Schmutztitel

Vorname Nachname

Grand Canonical Monte Carlo Simulation of Confined Hard Sphere Fluids

From Density to Topology

Diplomarbeit

von

Stefan Kuczera

betreut durch
Dr. Gerd Schröder-Turk
Prof. Dr. Klaus Mecke
Prof. Dr. Roland Roth

Erlangen,
18.August 2010

Abstract

Thermodynamical properties of confined fluids depend on the shape of the confinining cavity. A general hypothesis assumes that this dependence is expressed as a linear combination of four terms, namely the volume of the cavity, its interfacial area and integrated mean curvature and its Euler characteristic [33]. König *et al.* have shown by means of density functional theory that for hard-sphere fluids and for simple pore shapes this hypothesis is numerically valid [27, 28].

Here, this work is extended by grand-canonical Monte Carlo simulation studying the equilibrium fluid density and adsorption in cavities of complex shape. The confining cavities are given by periodic labyrinthine domains bounded by so-called triply-periodic minimal surfaces. The actual solid-pore interface is representated by a triangulated version of these surfaces. Due to previous work of Gerd Schröder-Turk these tringulations are available for all studied structures [47]. However, using the example of the Diamond constant mean curvature family, an alternative method is described for the generation of tringulated triply-periodic geometries. This is done with the help of the surface evolver program [5].

The implementation of the Monte Carlo algorithm as a `C++` program is explained in detail. In particular, a fast predicate to test whether a sphere is inside or outside of the confining domain is described. For bulk simulations, i.e. simulations without confinement, we find good agreement with the Carnahan-Starling theory for hard spheres.

Results for the confined simulations are compared to 3-dimensional numerical DFT calculations (carried out by Roland Roth [44]) und to an analytic morphometric approach [21, 27, 28]. We find quantitative agreement for all studied surfaces in the range of our simulation input parameters for both the confined packing fraction and the adsorption. Further, we are able to show, that the Euler number X of the cavity can be estimated from the equilibrium number of spheres in the cavity. Finally, we find out that the morphometric approach is working particularly good for channel widths larger than two times the correlation length ξ for the studied triply-periodic minimal surfaces.

Kurzreferat

Thermodynamische Eigenschaften von Flüssigkeiten hängen von der Form des Hohlraums ab, der sie umgibt. In Folge einer allgemeinen Hypothese wird angenommen, dass sich diese Abhängikeit als Linearkombination von vier Größen ausdrücken lässt. Namentlich sind dies das Volumen des Hohlraums, der Flächeninhalt der Grenzfläche, die integrierte mittlere Krümmung über diese Grenzfläche and die Eulercharakteristik des Hohlraums [33]. König *et al.* haben mit Hilfe von Dichtefunktionaltheorie gezeigt, dass diese Annahme für Hartkugelsysteme und für einfache Geometrien im Rahmen der numerischen Genauigkeit gültig ist [27, 28].

In der vorliegenden Arbeit wird diese Vorarbeit auf die Untersuchung von Gleichgewichtsdichten und Adsorption in komplex geformten Hohlräumen mittels großkanonischen Monte Carlo Simulationen erweitert. Die begrenzten Hohlräume sind durch periodische Labyrinthe gegeben, die durch so genannte dreifach periodische Minimalflächen begrenzt sind. Die Grenzschicht wird durch eine Triangulierung dieser Flächen dargestellt. Aufgrund von Arbeiten von Gerd Schröder-Turk, sind diese Triangulierungen für alle untersuchten Flächen verfügbar [47]. Dennoch wird eine Methode beschrieben, die es ermöglicht triangulierte Flächen von dreifach periodischen Geometrien zu erzeugen. Dies wird anhand einer Familie von Diamond Flächen beschrieben die alle konstante mittlere Krümmung haben. Die Flächen werden mit Hilfe des Programms Surface Evolver erzeugt [5]. Die Realisierung des Monte Carlo Algorithmus in Form eines C++ Programms wird detailiert beschrieben. Insbesondere wird auf ein Verfahren eingegangen, mit dessen Hilfe man schnell entscheiden kann, ob eine Kugel innerhalb oder ausserhalb der Pore ist. Für Simulationen ohne begrenzte Geometrie lässt sich eine gute Übereinstimmung mit der Carnahan-Starling Theorie harter Kugeln feststellen.

Die Ergebnisse für Simulationen in begrenzten Hohlräumen werden mit Ergebnissen verglichen, die entweder durch 3-dimensionale numerische Dichtefunktionalrechnungen (durchgeführt von Roland Roth [44]) erhalten wurden oder durch einen morphometrischen Ansatz analytisch erzeugt worden sind [21, 27, 28]. Es stellt sich heraus, dass sich für die begrenzte Packungsdichte und die Adsorption für alle Flächen im Bereich unserer Eingabeparameter quantitative Übereinstimmmung feststellen lässt. Ausserdem zeigen wir, das sich die Euler Zahl des Hohlraums aus der mittleren Teilchenzahl im Gleichgewichtszustand reproduzieren läst. Ausserdem wird noch gezeigt, dass der morphometrische Ansatz besonders dann gut funktioniert, wenn die mittelere Kanalbreite der untersuchten dreifach periodischen Minimalflächen grösser ist als die doppelte Korrelationslänge ξ.

Contents

1 Introduction 3

I Main Part 5

2 Basic Concepts 7
- 2.1 Topological and Geometrical Aspects 7
  - 2.1.1 Topology 7
  - 2.1.2 Parallel Body 8
- 2.2 Grand Canonical Ensemble 10
- 2.3 Confined Hard Sphere Systems 11

3 Minimal and Constant Mean Curvature Surfaces 15
- 3.1 Triply-Periodic Minimal Surfaces 15
- 3.2 Generation of Diamond Constant Mean Curvature Surfaces with Evolver 17
  - 3.2.1 Constant Mean Curvature Surfaces 17
  - 3.2.2 Surface Evolver 18
  - 3.2.3 Generation of Constant Mean Curvature Diamond 18
  - 3.2.4 Step Method 19
- 3.3 Medial Surface 22

4 Grand Canonical Monte Carlo Simulation of Confined Hard Spheres 25
- 4.1 Monte Carlo Method 26
- 4.2 Grand Canonical Monte Carlo 29
- 4.3 Implementation of the Monte Carlo Method 31
  - 4.3.1 Simulation of Confined Hard Sphere Fluids 31
  - 4.3.2 Fast Substrate-Sphere Interaction 33
  - 4.3.3 Geometrical Calculations 37
  - 4.3.4 Error Estimation 38
- 4.4 Thermodynamic Consistency for the Bulk Fluid 40
- 4.5 Simulation Result 43
  - 4.5.1 Simple Geometries 44
  - 4.5.2 Minimal Surfaces 44
  - 4.5.3 Comparison to DFT Data with Voxelized Interfaces 46

5 Morphometric Approach for Large Pores 51
- 5.1 Morphometric Approach 51
- 5.2 Results for Large Pores 54
  - 5.2.1 Confined Packing Fraction η_0 55

5.2.2 Adsorption Γ 60
5.2.3 Influence of Topology on Simulated Averages 62

6 Deviations from the Morphometric Formula **69**

7 Development of the Monte Carlo Algorithm **75**
7.1 Simulation Results with μ^* as Input Parameter 75
7.2 Mistake in the Monte Carlo Implementation 79
7.3 Random Number Generator 79
7.4 Finite Size Effects 80

8 Summary and Outlook **81**

Appendices **83**
A.1 Evolver File for D-CMC Surface 84

List of Figures **87**

List of Tables **93**

Bibliography **95**

Danksagung **97**

Erklärung **100**

Introduction

1 Introduction

The statistical physics of bulk properties of simple fluids, that is fluids in containers of infinite size, are well understood [20, 25]. In contrast, the properties of spatially confined fluids, for example in porous media or in biological cells or networks, are subject of current research. Several critical phenomena, such as capillary condensation, are the consequence of confinement of a fluid in containers of nano-or micrometer scale where the fluid senses the influence of the substrate [10, 15]. However confinement also affects noncritical properties of the fluids. Rather the thermodynamic potentials (that determine the equilibrium properties of the fluid) are dependent on the shape or morphology of the confining domain. For example, the grand-canonical partition function Ω, that for bulk fluids is a function of the container size V available to the particles, of the chemical potential μ and of the temperature T, becomes a function of the shape of the confining domain S. For the situation where the fluid correlation length ξ is substantially smaller than the domain sizes and for confining domains that are represented by the complement of convex bodies, it has recently been argued (and evidence given by density functional theory [28]) that

$$\Omega[S;\mu,T] = -p(\mu,T)\cdot V[S] + \sigma(\mu,T)\cdot A[S] + \kappa(\mu,T)\cdot C[S] + \bar{\kappa}(\mu,T)\cdot X[S]\ . \tag{1.1}$$

Here $V[S]$ is the volume of S, $A[S]$ the surface area of its bounding surface ∂S, $C[S]$ the integrated mean curvature of ∂S and X the Euler number of S. The coefficients p, σ, κ and $\bar{\kappa}$ are independent of S but depend on T and μ. However, these studies considered only domains S that were the complement of a convex body, implying that the effect of the substrate-fluid interaction can decay infinitely to the bulk case at large distances from the substrate.

Here, these studies are extended to periodic bodies that are bounded by triply-periodic minimal surfaces. The fluid is modeled by a hard sphere system, that is confined to this body. The equilibrium properties are studied by grand canonical Monte Carlo simulaton of the confined hard sphere fluid. Our aim is to show that Eq. (1.1) holds if certain physical conditions are satisfied by the grand canonical potential Ω.

Part I

Main Part

2 Basic Concepts

This chapter outlines the framework of confined hard sphere systems in the grand canonical ensemble. Most of the theorems and definitions used in the thesis are provided in this chapter. Especially the description of the confined hard sphere system in section 2.3 is important for the understanding of the following chapters.

2.1 Topological and Geometrical Aspects

A short introduction on topology is given in the first subsection. The Euler number X, or Euler characteristic, is defined and linked to differential geometry via the Gauss-Bonnet theorem (Eq. (2.2)). Further, the Steiner formula for the volume computation of a parallel body $\mathcal{B}_r$ is introduced.

2.1.1 Topology

The aim of this section is rather an informal introduction to the topology of geometrical objects in the 3D Euclidean space $\mathbb{E}^3$ than a profound description of the large field of topology found in hundreds of textbooks, as this would certainly go beyond the scope of this thesis. In particular, we stick to the introduction given in Ref. [23].

There are some fundamental aspects of shapes that are preserved if the objects studied consist of stretchable rubber sheets. A rubber sphere may be deformed into an ellipsoid, a long narrow cylinder, a cube or any other globular object, without any rupturing or fusion of the surface (Fig. 2.1). Similarly, a torus can be deformed into any object containing a single handle or a single hole. But it is not possible to deform the rubber torus into a sphere without destroying the connectivity of the rubber sheets.

This concept is the basis for the topology of 3D objects. Only those characteristics of the surface that are maintained upon stretching and squeezing are relevant. The usual notion of geometrical quantities like distance or area are excluded from topological analysis. The topological characteristics of a surface S can be quantified by single integer value, their corresponding Euler number $X(S)$. We define the Euler number, or Euler characteristic, as

$$X(S) = 1 - g(S) \;, \tag{2.1}$$

where $g(S)$ denotes the genus of S[1]. The genus is equivalent to the number of cavities and handles in the surface and measures its connectedness [23].

---

[1] In this definition, the Euler number of a sphere is 1, in contrast to an often employed definition, where $X = 2$ for a sphere

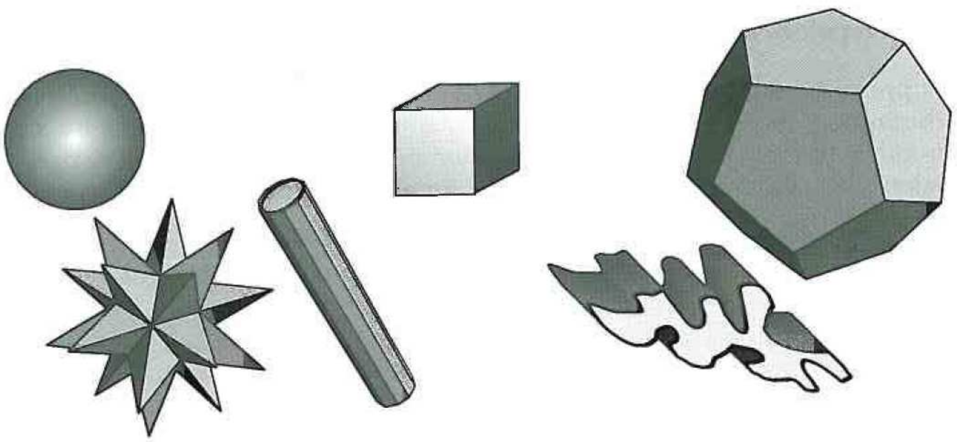

Fig. 2.1: A sphere can be stretched and bent (without any rupture of fusion of the surfaces) into an infinite variety of globular surfaces, all topological equivalent. Source: [23]

The link to differential geometry given by the Gauss-Bonnet theorem. For a closed surface S, i.e. a surface without boundaries, it states that

$$\int_S \mathrm{d}A\ K = 4\pi X\ , \tag{2.2}$$

where K is the Gaussian curvature. The Gaussian curvature can be computed from the principle radii of curvature R_1 and R_2 by

$$K = \frac{1}{R_1 R_2}. \tag{2.3}$$

A more general version of this theorem and a thorough survey of differential geometry is found in Ref. [8]. Nevertheless these results are sufficient to extend these notions to the minimal surfaces that are discussed in section 3.1. A list of simple structures and their corresponding Euler number can be found in table 2.1.

2.1.2 Parallel Body

The concept of a parallel body and Steiner's formula to compute its volume is introduced in this subsection. This is particularly fruitful for hard wall interactions that are discussed in section 2.3. The definitions and theorems are taken from Ref. [33], if not otherwise stated.

The parallel body $\mathcal{B}_r$ of a 3-dimensional body $\mathcal{B}$ is defined as

$$\mathcal{B}_r = \mathcal{B} \uplus B_r, \tag{2.4}$$

	Sphere	Torus	Double torus	Triple torus	Klein bottle
	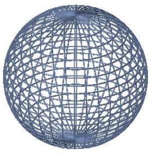			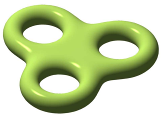	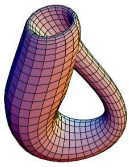
X=	1	0	-1	-2	0

Table 2.1: Euler number for some simple geometries. It can be calculated by $X = 1 - g(S)$, where the genus of the surface $g(S)$ is sum of cavities and handles (see Eq. (2.1)). Note that the Euler number of a sphere is equal to 1 for the definition used in this thesis. Source: [1]

where B_r is a sphere of radius $r > 0$ centered at the origin. The Minkowski sum $C = A \uplus B$ of two sets $A, B \subset \mathbb{E}^3$ is defined as

$$A \uplus B = \{a + b \mid a \in A, b \in B\} \ . \tag{2.5}$$

If we also assume that the body $\mathcal{B}$ is bounded, closed and convex, the Steiner formula can be applied. It states the volume $V(\mathcal{B}_r)$ of the parallel body $\mathcal{B}$ is given by

$$V(\mathcal{B}_r) = V(\mathcal{B}) + r \cdot A(\mathcal{B}) + r^2 \cdot C(\mathcal{B}) + \frac{r^3}{3} X(\mathcal{B}) \cdot 4\pi \ , \tag{2.6}$$

where $A(\mathcal{B})$ is the area of the boundary $\mathcal{O} = \partial\mathcal{B}$ and $X(\mathcal{B})$ the Euler number of $\mathcal{B}$ as defined in section 2.1.1. The integrated mean curvature C is given by

$$C = \int_{\mathcal{O}} \mathrm{d}\mathcal{O}\ H \ , \tag{2.7}$$

where H is the mean curvature, that can be obtained from the principle radii of curvature R_1 and R_2 by

$$H = \frac{1}{2}\left(\frac{1}{R_1} + \frac{1}{R_2}\right) \ . \tag{2.8}$$

V,A,C,X are also known as Minkowski functionals. The surface area A, the integrated mean curvature C and the Euler number X of $\mathcal{B}_R$ can be calculated with the help of following equations

$$A(\mathcal{B}_R) = A(\mathcal{B}) + 2r \cdot C(\mathcal{B}) + r^2 \cdot X(\mathcal{B}) \cdot 4\pi \ , \tag{2.9}$$

$$C(\mathcal{B}_R) = C(\mathcal{B}) + r \cdot X(\mathcal{B}) \cdot 4\pi \ , \tag{2.10}$$

$$X(\mathcal{B}_R) = X(\mathcal{B}) \ . \tag{2.11}$$

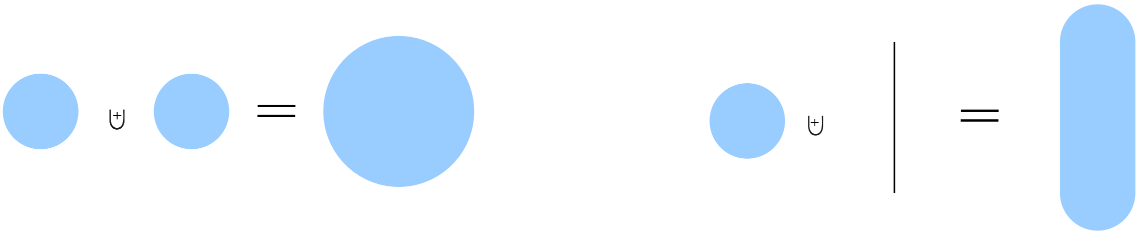

Fig. 2.2: Examples for the Minkowski sum of two sets. A parallel body $\mathcal{B}_r$ (2.4) of a body $\mathcal{B}$ is obtained by Minkowski addition of a sphere (or a disk in 2D) with radius r and $\mathcal{B}$. Source: [35]

2.2 Grand Canonical Ensemble

There are three main ensembles in statistical mechanics. The microcanonical ensemble describes a system that is totally isolated and has a fixed number of particles N, a fixed total energy E and a fixed volume V. In contrast the total energy E is a fluctuating quantity in the canonical ensemble, that characterizes a system that can exchange energy with a heat bath. The temperature T, the number of particles N and the volume V describe the state of the system. Furthermore if it is also possible for the system to exchange particles with a (particle) reservoir, one speaks of the grand canonical ensemble. The number of particles N also becomes a fluctuating quantity, whereas the state of the system is now characterized by the chemical potential μ, the temperature T and the volume V.

All ensembles are equivalent in the thermodynamic limit and it is possible to transform between different ensembles. Therefore the choice of an ensemble for a computer simulation is only a matter of convenience. In particular we are interest in the measurement of an average of a fluctuating thermodynamic property in an equilibrium system. As the number of particles of a systems is easily measured during a computer simulation, the grand canonical potential is chosen as the most suitable.

In the grand-canonical (μ, V, T)-ensemble the partition function for a classical system is given by

$$\Xi(\mu, V, T) = \sum_{N=0}^{\infty} \frac{z^N}{N!} \int_V \mathrm{d}\vec{r}^N e^{-\beta U(\vec{r}^N)} , \tag{2.12}$$

with $\vec{r}^N = (\vec{r}_1, \dots, \vec{r}_N)$, the fugacity $z = \exp(\beta\mu)/\Lambda^3$, the de Broglie thermal wavelength $\Lambda = (2\pi\beta\hbar^2/m)^{1/2}$ and the potential U. The ensemble average of any function $F(\vec{r}^N)$ of the particles coordinates can be expressed as

$$\langle F \rangle = \frac{1}{\Xi} \sum_{N=0}^{\infty} \frac{z^N}{N!} \int_V \mathrm{d}\vec{r}^N F(\vec{r}^N) e^{-\beta U(\vec{r}^N)} . \tag{2.13}$$

For the average number of particles in particular this yields

$$\langle N \rangle = \left(\frac{\partial \ln \Xi}{\partial \ln z} \right)_{V,T} . \tag{2.14}$$

It is obvious that even for simple potentials U the grand canonical partition function Ξ can only be calculated approximately. Therefore numerical methods are required. An example is the Monte Carlo method discussed in chapter 4.

The link to the grand canonical potential Ω follows from the relationship

$$\beta\Omega = -\ln\Xi \; . \tag{2.15}$$

The average number of particles can also be written as

$$\langle N\rangle = -\left(\frac{\partial\Omega}{\partial\mu}\right)_{V,T} \tag{2.16}$$

in terms of the grand canonical potential. Note that this is equivalent to Eq. (2.14).

Normally it is assumed that the grand canonical potential is an extensive quantity which means that it scales linearly with the volume V of the described system. Therefore in many textbook the relation

$$\Omega(\mu, V, T) = -p(\mu, T)V \; , \tag{2.17}$$

where $p(\mu, T)$ denotes the pressure, is given as a complete expression for Ω. This simple form, however, is valid only for infinite bulk, i.e. unconfined systems. If the system S is bounded by some container, the grand canonical potential becomes a functional $\Omega[S; \mu, T]$, that dependents in a potentially complicated manner on the shape of this container. The characterization of this shape dependency is one main aspect of this thesis.

2.3 Confined Hard Sphere Systems

The fluid model studied is a three-dimensional system of hard spheres of constant diameter $\sigma := 2R = 1$ whose centers are restricted to a rectangular domain $\mathbb{P} = [0, L_x] \times [0, L_y] \times [0, L_z] \subset \mathbb{E}^3$ with periodic boundaries. The pair-wise interaction between spheres at $\vec{r}$ and $\vec{r}\,'$ is given by

$$U_{sph}(\vec{r}, \vec{r}\,') = \begin{cases} 0 & \text{if } \; d(\vec{r}, \vec{r}\,') > \sigma \\ \infty & \text{otherwise} \end{cases} \; , \tag{2.18}$$

where $d(\vec{r}, \vec{r}\,')$ is the Euclidean distance with respect to the periodic boundary conditions. The volume of the spheres is denoted by

$$V_{\mathrm{sph}} = \frac{4}{3}\pi R^3 \; . \tag{2.19}$$

In addition the spheres are confined to a periodic pore domain $\mathcal{P}' \subset \mathbb{E}^3$ with translational lattice vectors $L_x\vec{e}_x$, $L_y\vec{e}_y$ and $L_z\vec{e}_z$ with Cartesian unit vectors $\vec{e}_x$, $\vec{e}_y$ and $\vec{e}_z$. The domain is bounded by the interface $\mathcal{I}' = \partial\mathcal{P}'$, that is assumed to be oriented such that the normal $\vec{n}(\vec{p})$ points into $\mathcal{P}'$ for all points $\vec{p} \in \mathcal{I}'$. The complement of $\mathcal{P}'$ is $\mathcal{B}' := \mathbb{E}^3 \setminus \mathcal{P}$, also called *substrate* or *solid*. As we apply periodic boundaries, the actual pore $\mathcal{P}'$ can be reduced to the pore domain $\mathcal{P} = \mathcal{P}' \cap \mathbb{P}$ within the rectangular domain $\mathbb{P}$. The same argument follows for the substrate $\mathcal{B} = \mathcal{B}' \cap \mathbb{P}$. As a consequence $V[\mathcal{P}] + V[\mathcal{B}] = V_{\mathbb{P}}$.

The effective interface within $\mathbb{P}$ is $\mathcal{I} = \mathcal{I}' \cap \mathbb{P}$. We furthermore require that the effective interface $\mathcal{I}$ is continuous on the boundaries.

This confinement is expressed by an interaction between a sphere at point $\vec{r}$ and the substrate

$$U_{sub}(\vec{r}) = \begin{cases} 0 & \text{if} \quad D(\vec{r}) > \sigma/2 \\ \infty & \text{otherwise} \end{cases} , \tag{2.20}$$

where $D(\vec{r}) = \min_{\vec{p} \in \mathcal{B}} d(\vec{p}, \vec{r})$ is the distance from the sphere center to the (or a, if there are more than one) nearest point $\vec{p} \in \mathcal{B}$ of the substrate $\mathcal{B}$.

The combined potential incorporating both sphere-sphere interaction U_{sph} and substrate-sphere interactions U_{sub} is given by

$$U(\vec{r}_1, \dots, \vec{r}_N) = \sum_{i=1}^{N} U_{sub}(\vec{r}_i) + \sum_{i>j}^{N} U_{sph}(\vec{r}_i, \vec{r}_j) \ . \tag{2.21}$$

This potential is 0 for a combination without any pair of overlapping spheres and without any sphere overlap with the substrate, and infinite otherwise.

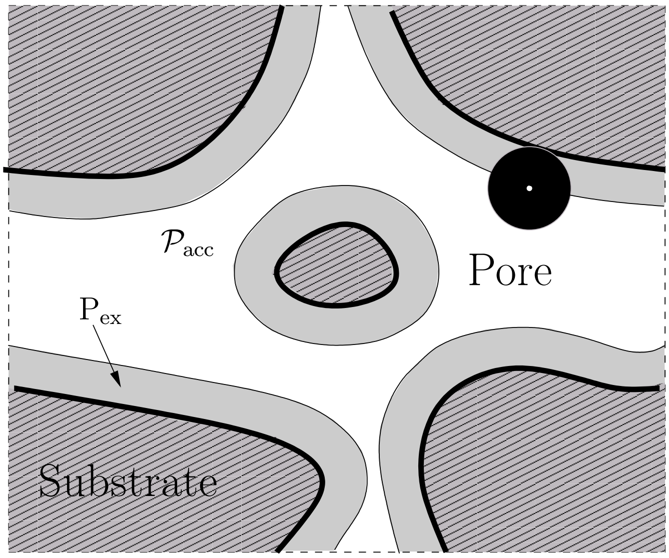

Fig. 2.3: Sketch of the pore geometry. The white part is the accessible pore space $\mathcal{P}_{\text{acc}}$ (2.22), whereas P_{ex} is the region that the sphere centers cannot penetrate due to hard core interaction with the wall. It also required that the surface is continuous on the boundaries, as depicted here.

We further introduce the parallel body $\mathcal{B}'_R$ (cf. Eq. (2.4)) of the substrate. This domain can also be reduced to the rectangular domain $\mathbb{P}$, therefore we define $\mathcal{B}_R = \mathcal{B}'_R \cap \mathbb{P}$ as the effective parallel body. By the nature of the potential defined in Eq. (2.20), the domain $\mathcal{P}_{\text{acc}} = \mathbb{P} \setminus \mathcal{B}_R$ is the accessible pore space for the centers of the hard spheres with volume

$V_{\mathrm{acc}}[\mathcal{P}] = V[\mathcal{P}_{\mathrm{acc}}]$. The volume of the domain $\mathrm{P}_{\mathrm{ex}} = \mathcal{P} \cap \mathcal{P}_{\mathrm{acc}}$ is referred to as excluded volume $V[\mathrm{P}_{\mathrm{ex}}]$. Although the substrate domain $\mathcal{B}$ is not necessarily convex, Steiner's formula can be applied to ${\mathcal{B}_R}^2$, if there are no self intersections of the parallel surface. We assume that this true for the studied systems as long as the sphere radius is small compared to L_x, L_y and L_z. Under consideration of the periodic boundaries this implies

$$V_{\mathrm{acc}}[\mathcal{P}] = V[\mathcal{P}] - R \cdot A[\mathcal{I}] - R^2 \cdot C[\mathcal{I}] - \frac{4\pi R^3}{3} X[\mathcal{I}] \ , \tag{2.22}$$

where $A[\mathcal{I}]$ is the area of the interface surface, $C[\mathcal{I}]$ its integrated mean curvature, and $X[\mathcal{I}]$ its Euler number as defined in Eq. (2.2). As we assume that $\mathcal{I}$ is a closed surface due to the periodic boundary conditions and continuous on the boundaries, the application of Eq. (2.2) is valid. For reasons of simplicity, we identify $A[\mathcal{P}] = A[\mathcal{I}]$, $C[\mathcal{P}] = C[\mathcal{I}]$ and $X[\mathcal{P}] = X[\mathcal{I}]$.

We are interested in equilibrium properties of this system for a given chemical potential μ, temperature T and pore domain $\mathcal{P}$. We define the confined packing fraction

$$\eta_0(\mathcal{P}, T, \mu) := V_{\mathrm{sph}} \frac{\langle N \rangle}{V_{\mathrm{acc}}[\mathcal{P}]} \ , \tag{2.23}$$

with the grand canonical average particle number $\langle N \rangle_{\mathcal{P},T,\mu}$ (Eq. (2.14)) and the accessible Volume $V_{\mathrm{acc}}[\mathcal{P}]$. Note that for a bulk system without confining substrate, $U_{sub} \equiv 0$, this corresponds to the definition of the bulk packing fraction

$$\eta = V_{\mathrm{sph}} \rho_{\mathrm{bulk}} \ , \tag{2.24}$$

where ρ_{bulk} is the number density of a hard sphere bulk fluid, i.e.

$$\rho_{\mathrm{bulk}} = \frac{\langle N \rangle_{V,T,\mu}}{V} \ . \tag{2.25}$$

The porosity $\phi[\mathcal{P}]$ is defined as the volume fraction

$$\phi[\mathcal{P}] = \frac{V[\mathcal{P}]}{V_{\mathbb{P}}} \ . \tag{2.26}$$

The physical situation is as follows: The confined fluid is in contact with a bulk fluid of known chemical potential μ, that can be regarded as a particle reservoir. The temperature dependence is omitted, as for hard core interactions, there is no energy scale to be compared to the thermal energy $k_{\mathrm{B}}T$. For reasons of convenience we define

$$k_{\mathrm{B}} T = 1 \ . \tag{2.27}$$

Furthermore it useful to split the chemical potential $\beta\mu$ into an ideal gas part $\beta\mu_{\mathrm{id}}$ and an excess (over ideal gas) part. The excess chemical potential is defined as:

$$\beta\mu_{\mathrm{ex}} := \beta\mu - \beta\mu_{\mathrm{id}} \quad \text{with} \quad \beta\mu_{\mathrm{id}} = \ln\left(\Lambda^3 \rho_{\mathrm{bulk}}\right) \ , \tag{2.28}$$

---

[2] Strictly speaking, $\mathcal{B}_R$ is not a parallel body in the original sense expressed in Eq. (2.4). For a proper mathematical definition, we had to define the parallel body on the quotient space $\mathbb{E}^3 / \sim$ with $x \sim y$ if $y = x + k_1 L_x \vec{e}_x + k_2 L_y \vec{e}_y + k_3 L_z \vec{e}_z \ , \ k_1, k_2, k_3 \in \mathbb{Z}$

where μ_{id} is the chemical potential of an ideal gas at same density ρ_{bulk} as the particle reservoir. It is important to remark, that the ideal gas contribution to the chemical potential is always referring to the density of the reservoir and not to the density of the confined system. This is also discussed in section 7.1 in context of an alternative input parameter μ^* for the Monte Carlo simulation. According to Eq. (2.28) the fugacity z can be written as

$$z = e^{(\beta\mu)}/\Lambda^3 = \rho_{\mathrm{bulk}} e^{\mu_{\mathrm{ex}}} \ . \tag{2.29}$$

This means, that the fugacity z does not depend on the definition of the thermal wavelength Λ. As z is the relevant parameter for the characterization of equilibrium properties, Λ can be set to any nonzero positive value. This is further discussed in section 4.2.

Finally it shall be remarked that even for a bulk hard sphere fluid the grand canonical partition function (2.12) cannot be solved analytically. Nevertheless there are theories that approximate η as a function of μ very accurately for a range of $0 \leq \eta \leq 0.4$. Namely these are the Percus-Yeckick solution [38] and the Carnahan-Starling equation of state (EOS) [6].

3 Minimal and Constant Mean Curvature Surfaces

The solid-pore interfaces of the confined hard sphere system are represented by discretized triply-periodic minimal surfaces (TPMS). General properties of certain representatives of the TPMS class are discussed in section 3.1. In section 3.2 the concept of constant mean curvature (CMC) surfaces is briefly introduced. Further, using the example of the Diamond CMC surface family, a method is described to obtain triangulations of these surfaces with the help of the program surface evolver. In particular, the generation of a CMC surface with prescribed porosity ϕ is described in detail. In the final section the concept of Medial surfaces (MS) is introduced. MS are used for the pore volume calculation in the Monte Carlo program described in section 4.3.3. They are also needed for the determination of the narrowest and widest points of the pore, which in turn are a measure for the average channel width of the TPMS used in chapter 6 in context of the applicability of the morphometric approach for different pore geometries.

3.1 Triply-Periodic Minimal Surfaces

Triply periodic minimal surfaces (TPMS) have vanishing mean curvature H for all points and partition space into two intertwined channel systems, if they are free of intersections. The Gyroid surface shown in Fig. 3.1 is a common example. Triply periodic means, that they are periodic in each space direction with three independent translational lattice vectors. In general, the two distinct labyrinths can be geometrically different. A TPMS whose two labyrinths are congruent is called balanced [47].

The term minimal stems from the fact that any sufficiently small patch cut from a such a surface has the least area of all surface patches with the same boundary. In fact, minimal surfaces are local minima of the surface area functional with respect to infinitesimal normal variations. Interestingly, this is equivalent to a vanishing mean curvature H. A profound deduction is found for example in Ref. [8].

Due to the translational periodicity, the analysis of TPMS can always be restricted to the unit cell. As all known TPMS also exhibit a large number of additional symmetries only a small representative fraction of the surface is needed to obtain any extended version of the TPMS by application of congruence transformations in Euclidean space. The smallest representatives are called fundamental regions or asymmetric units. The set of operations that are needed to reproduce a translational unit cell from the asymmetric unit patch is given by the Euclidean space group of the TPMS.

There is an infinite number of TPMS, but the three surfaces called Gyroid, Primitive (P) and Diamond (D) shown in Fig. 3.1 are the best-known with cubic symmetry. Furthermore these representatives are also balanced, whereas the two labyrinthine domains of the I-WP

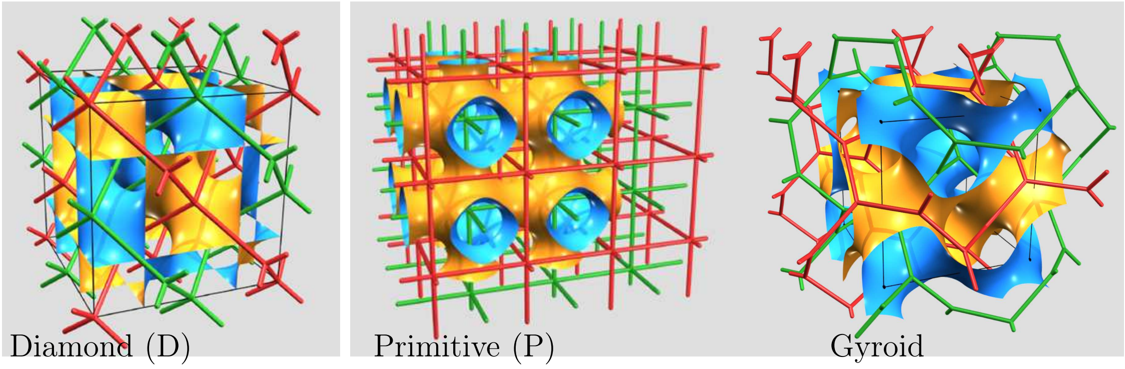

Fig. 3.1: The triply-periodic Diamond, Primitive and Gyroid minimal surfaces with cubic symmetries. The Primitive structure consists of 8 (smallest) cubic unit cells. The topology of the surfaces is expressed by the skeletal graph that measures the connectedness of the surface [47]. Different colors indicate the two congruent labyrinths of the balanced surfaces. Triangulated representatives are available for the Monte Carlo simulation of confined hard spheres. Source: [47].

surface (see Fig 3.5) are not congruent. The labyrinth with the larger porosity is denoted by "I", the other by "WP". The H surface, an example for a balanced TPMS with a tetragonal unit cell, is depicted in Fig. 3.2. Although there are a different types of unit cells, e.g. orthorhombic or hexagonal unit cells, we restrict ourselves to those with tetragonal or cubic symmetries, as the implementation in the Monte Carlo simulation program is easier, especially regarding the realization of periodic boundary conditions.

Our aim is to examine the thermodynamical properties of a hard sphere fluid confined to those geometries. This is done by defining one of the channels as the substrate, the other labyrinth as the pore domain. The actual solid-pore interface is then represented by the minimal surface. Technically speaking, we impose an orientation on the surface. For any balanced surface either choice of the solid channel leads to the same resulting structure, whereas both choices for the I-WP surface exhibit different physical situations.

For the implementation in the Monte Carlo program the minimal surface is represented by a triangulation, i.e. a set of vertices and set of triangles connecting these vertices. These sets are stored in a poly type file, which is readable for the program. This file consists of two parts. The first part is a list of the coordinates of the vertices and their corresponding index. The second part lists all triangles, which are represented by the indices of their corresponding vertices. For all minimal surface studied in this thesis, triangulations were available. The generation of these triangulations was carried out by Gerd Schröder-Turk with the help of its analytic representation, i.e. its Weierstrass parametrization. These parametrization and a detailed description of the generation method is found in Ref. [47]. An alternative method for the generation of a triangulated minimal surface is presented in section 3.2 using the example of the Diamond surface.

Although the Euler number of an infinitely extended TPMS is not defined, one can define the Euler number X per translational unit cell in spirit of Eq. (2.2) by restricting the integral to the surface contained within this cell. Therefore if we refer to an Euler number X of a TPMS, we mean the Euler number per cubic or tetragonal translational unit cell. It is remarkable that the Euler number per translational unit cell is always an integer value for the examined structures [47]. This is going to be important for the examinations in chapter 5, where the dependency of certain thermodynamical properties on the shape of a pore domain is studied.

Furthermore, triply-periodic minimal surfaces are generic models for negatively curved pore geometries, and are also motivated by their realizations as nanoscopic spatial structures in self-assembled structures, for example in some butterfly wings [24].

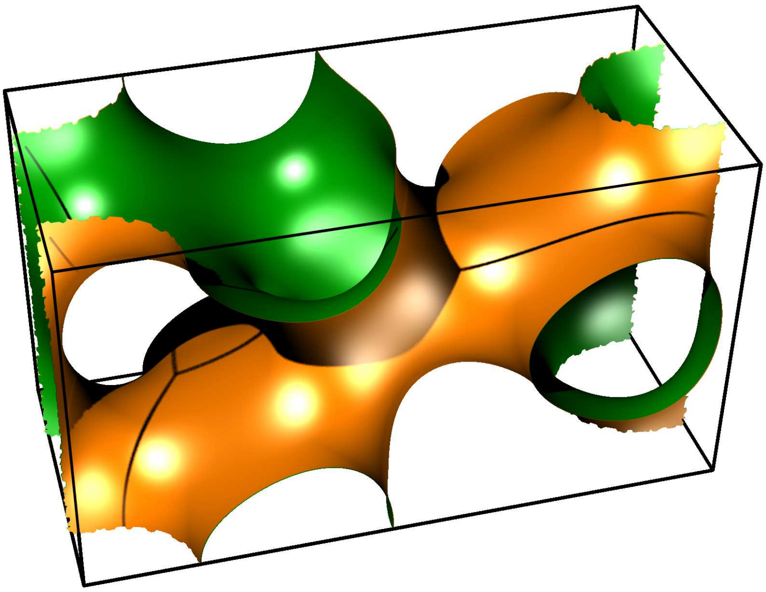

Fig. 3.2: The triply-periodic H surface. The frame outlines the tetragonal translational unit cell of the surface. One side of the surface is colored green, the other orange. The two labyrinth domains are congruent, i.e. the surface is balanced.

3.2 Generation of Diamond Constant Mean Curvature Surfaces with Evolver

Cubic unit cells for several triangulated Diamond CMC surfaces were created with the help of the program evolver [5]. Although these surfaces are not used for further examination in this thesis, the methodology is briefly discussed in this section. Surfaces up to a volume fraction of $\phi = 1/6$ could be generated (see table 3.1).

3.2.1 Constant Mean Curvature Surfaces

Constant mean curvature (CMC) surfaces are surfaces with constant mean curvature $H(p)$ for all points p on the surface. Obviously any minimal surface is also CMC surface. Other examples for CMC surfaces are spheres and infinitely extended cylinders. It has been shown, that surfaces that minimize the area under a volume constraint have constant mean curvature [16]. This explains why soap bubbles are always spherical [41].

Karcher [26] has demonstrated that the TPMS introduced in section 3.1 can be deformed to produce surfaces of non-zero CMC. These deformations lead to a whole family of CMC surfaces for each minimal surface and induce changes in the relative amount of space contained on each side of the interface, or the volume fraction ϕ. These results are used to generate CMC members of the D surface family by the help of the program surface evolver, which is introduced here.

3.2.2 Surface Evolver

The main functionality of the program is the minimization of certain energy functionals, e.g. the surface area, for a triangulated input geometry S. This is done by means of conjugate gradient and Hessian methods, combined with iterative refinement of the initial triangulation. A detailed description is found in Ref. [5].

CMC surfaces are geometries with constant mean curvature H_0. Therefore the numerical minimization of the functional

$$E[S] = \int_S (H(p) - H_0)^2 dp \;, \tag{3.1}$$

where $H(p)$ is the point-wise mean curvature of S, is a fruitful approach to the generation of a CMC structure. This is done by determining the gradient of the functional $E[S]$ for the $3N$ dimensional system and then moving the vertices by a small (negative) value in direction of this gradient. The result is a triangulated surface, with local mean curvature close to H_0 for all points. As there exists not only one CMC surface for a certain value of H_0, it is clear that constraints have to imposed on the initial configuration to create the desired surface. The best way to express these constraints is by group theory and topology. The latter is expressed by the network graph of the corresponding CMC surface [47]. Furthermore, every known CMC surface belongs to a space group and inherits its symmetries. Therefore the proper knowledge of the corresponding space group for a specific surface is essential, as we will see for the Diamond CMC surface case. It is possible to define such constraints within the evolver program for a given geometry. A complete list of all space groups is found in Ref. [19].

3.2.3 Generation of Constant Mean Curvature Diamond

The starting point for the construction of the D-CMC surface was the evolver file for the Diamond minimal surface provided by Ken Brakke on Ref. [11]. It basically contains the initial patch for the smallest (asymmetric) unit cell of the surface. By minimizing $E[S]$ (Eq. (3.1)) for $H_0 = 0$, the program generates a smooth triangulated surface which can be extended to the cubic unit cell of the Diamond by applying the symmetry operations of its space group Pn$\overline{3}$m [9].

Setting the H_0 input parameter to a non-zero value and proceeding in the same way as for $H_0 = 0$ does not lead to the desired result, i.e. a CMC version of the Diamond structure, as the CMC family belongs to a different space group. It turns out that the Diamond CMC surface is of symmetry Fd$\overline{3}$m [17]. This can be understood by recalling that both labyrinths of the non-oriented Diamond minimal surface are totally equal, whereas for the CMC case the channel systems are different. Thus, an orientation has to be imposed on the geometry which leads to a loss of symmetry. Therefore the evolver file has to be modified to account for this discrepancy. A small summary of the changes and a working copy of the file is found in appendix A.1.

The initial surface patch is a coarse version of an asymmetric unit patch of the CMC Diamond surface. The general procedure is to use the `g` command to minimize the functional, until the functional $E[S]$ is below a small threshold. Each `g` command is equivalent to one gradient iteration step. Normally after $10^2 - 10^4$ iterations a refinement of the triangulation is employed using the `r` command.

To produce an even triangulation, i.e. a triangulation where all triangle edges are almost of the same length, the commands `w,u,l,t` and `V` are available. The commands `w,u` are used to equiangulate the triangles of the surface patch. The `l` command divides edges of lengths above a prescribed threshold, whereas the `t` command weeds out small triangles. A smoothing of the surface is initiated by the `V` command. For a detailed description of all commands see Ref. [5]. As the efficiency of the minimization process is also depending on the quality of the triangulation, this should always be checked after a certain amount of iterations. For an uneven triangulation of the surface patch it is possible that a sequence of gradient step results in a distorted surface with less symmetry.

After 3-4 refinements the surface patch close to the optimal configuration, i.e. the order of magnitude of the functional $E[S]$ is in the range of 10^{-20} to 10^{-15}. Now a `hessian_seek` command, that invokes one step of the Hessian method, can be used to further optimize the surface. This method works particularly good close to the local minimum, decreasing $E[S]$ to the numerical limit of $\sim 10^{-27}$.

The resulting surface is saved as poly type file (see section 3.1) for further processing. By imposing the space group symmetry operations on the surface patch, a cubic translational unit cell of the CMC Diamond structure is finally constructed. This is easily achieved by a graphic processing tool like houdini [22]. Nevertheless it has to be remarked that this method only works for values of H_0 values, where it has been shown that Diamond CMC surfaces exist [7].

3.2.4 Step Method

CMC structures with a certain volume fraction ϕ are of special interest. As there is no analytic relation linking H_0 and the volume fraction ϕ, we are not able to directly obtain a CMC Diamond for a specific value of ϕ. The problem is now to iteratively approximate the corresponding value H_ϕ for a given volume fraction ϕ.

The idea is to assume that the function $V(H)$ for the Diamond CMC surface family is continuous and monotonic in some vicinity of H_ϕ with $V(H_\phi) = V_\phi$, where $V(H)$ is the actual and V_ϕ the desired volume enclosed by the asymmetric unit patch, and therefore is approximated by a linear function

$$V(H) = a \cdot H \qquad \text{for} \qquad H \rightarrow H_\phi \ , \tag{3.2}$$

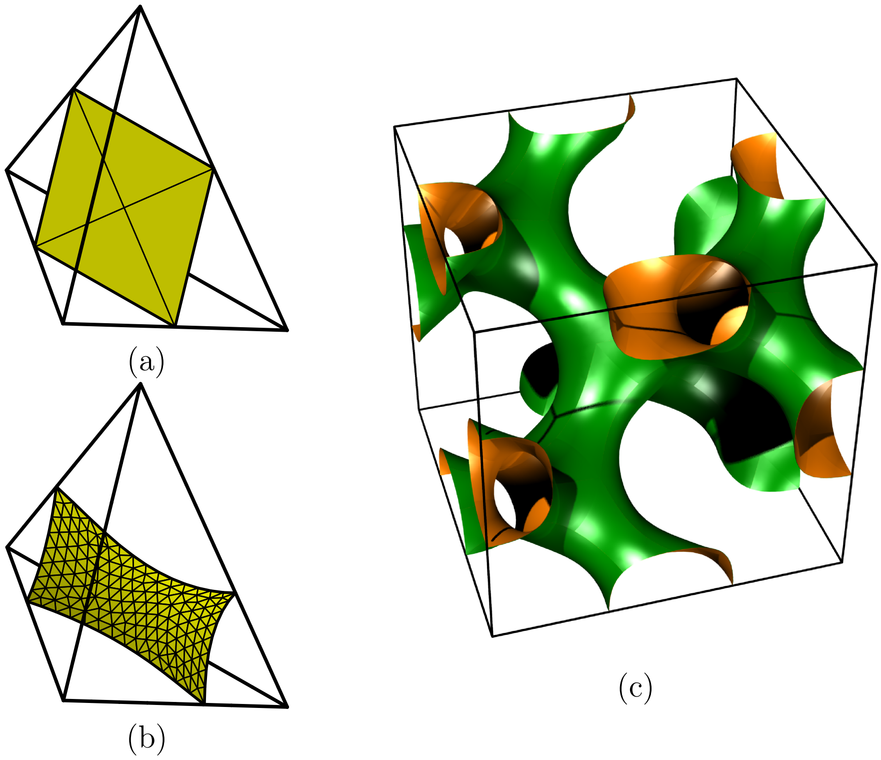

(a)

(b)

(c)

Fig. 3.3: (a) The initial surface patch of the evolver input file. The confining tetrahedron outlines the corresponding asymmetric unit cell of the CMC diamond. (b) Asymmetric unit patch after the minimization of the functional $E[S]$ (Eq. (3.1)) via the surface evolver program. The faces are mirror planes in the Fd$\overline{3}$m symmetry group. (c) A cubic unit cell of the D-CMC-surface with a volume fraction of $\phi = 0.25$. The colors indicate the orientation of the geometry (orange inside the pore, green outside).

with $a \approx V'(H_\phi)$. The proper computation of the volume contribution of the asymmetric surface patch to the Diamond CMC surface is already implemented in the evolver file. Therefore

$$V_\phi = \phi \cdot V_{\mathrm{auc}} \ , \tag{3.3}$$

with V_{auc} as the volume of the asymmetric unit cell. The first step is now to generate an asymmetric surface patch as described in section 3.2.3 with a value H_{initial} so that $V(H_{\mathrm{initial}})$ is close to V_ϕ . This is done using data of previous works on Diamond CMC surfaces which are found in [7, 29]. These information also help to approximate the gradient $V'(H_\phi)$ to obtain a used in the linear relation (Eq. (3.2)). It has to be pointed out that it is not necessary to know the exact gradient , which shall become clear, when describing the actual step method.

The idea of the step method is to alter the input value H of the functional $E[S]$ in small steps to gradually evolve a surface with the desired properties, i.e. the volume difference $\Delta V = V(H) - V_\phi$ is below a prescribed threshold and $E[S] \ll 1$. One step method sequence consists of the following:

The step length δH for H is calculated as

$$\delta H = \frac{\Delta V}{n \cdot a} \ , \tag{3.4}$$

where n is a natural number that regulates the refinement of our step length. Now the actual step happens, as the input parameter H is set to $H + \delta H$ and the functional $E[S]$ is minimized again using the `g` and `hessian_seek` commands. No more refinement or smoothing commands are used as they could change the value of $E[S]$ in an unexpected way and lead to a failure of the method. This step is repeated until either (a) $|\Delta V|$ is below the prescribed threshold (exit condition) or (b) any further addition of δH would lead to an increase of $|\Delta V|$. If the gradient a was chosen in a proper way, either cases occur after n steps, as it is illustrated in Fig. 3.4. This is the endpoint of the sequence.

The whole sequence is iterated until it exits with condition (a) and the whole procedure is finished. The cubic unit cell is now generated by the same means as in subsection 3.2.3.

It is clear, that an imprecise approximation of the gradient $V'(H_\phi)$ could result in slow convergence but not to the failure of the method, as long as a is close enough to the exact value of $V'(H_\phi)$. The choice of n is somewhat influenced by two counteracting effects. On the one hand a large value of n could lead to a very small $|\Delta V|$ after only one sequence. On the other hand this implies that this sequence also consists of many steps and therefore needs more computation time. For the Diamond CMC surface a value of $n = 3$ leads to good convergence in reasonable time. Additionally if the method gets stuck, one has either to approximate the gradient more precisely, increase the refinement parameter n or find a parameter H_{initial}, so that $V(H_{\mathrm{initial}})$ is closer to V_ϕ.

mean curvature $d/2 \cdot H_0$	0	0.393	0.528	0.702	0.861
volume fraction ϕ	0.5	0.3	0.25	0.2	$0.1\overline{6}$

Table 3.1: Evolution of D CMC structures with a given volume fraction. These surfaces are obtained by the step method. The volume of the initial asymmetric unit cell is $(1/12) \cdot d^3$ with d as edge length of the Fd$\overline{3}$m cubic unit cell.

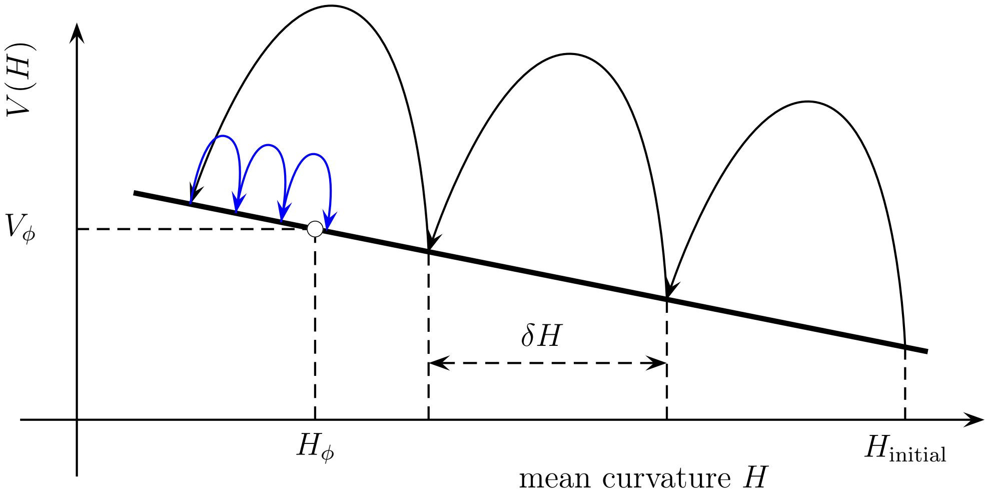

Fig. 3.4: An illustration of the step method. The plot shows schematically the volume V as function of the mean curvature H in the vicinity of H_ϕ . As this dependency is approximated linearly close to H_ϕ, the initial curvature H_{initial} is altered by δH (cf. Eq. (3.4)) to gradually generate a CMC-Diamond structure with desired volume fraction. The gradient of the linear function is a (cf. Eq. (3.2)). Each arc represents a step as defined in the step method. After $n = 3$ steps the step size is recalculated and the algorithm is iterated.

A list of surfaces obtained by this method is found in table 3.1.

3.3 Medial Surface

The concept of medial surfaces is briefly discussed in this section, as they are used for the volume calculation in section 4.3.3. They are also needed for the determination of the narrowest and widest points of a pore, which are used in chapter 6. A thorough survey of medial surfaces is found in Ref. [46].

According to Ref. [46], a medial surface MS of a domain S is defined as the locus of centers of maximal spheres, i.e. spheres wholly contained within the domains which graze the surface tangentially and are not contained in any other such sphere. One of the two channel systems of the minimal surfaces introduced in section 3.1 is an example for such a domain, that fulfills the requirements imposed on S in [46]. In a loose sense, the medial surface defines the center of a domain.

Some simple example are given now. The medial surface of an infinite slab of thickness d (bounded by two parallel planes) is a parallel plane at distance $d/2$ in between the two original planes. The medial surface of a sphere is its center point and the medial surface of a cylinder of infinite height with circular cross section is its rotational symmetry axis.

Any point $\vec{p} \in C$ on the boundary C of a domain S has exactly one corresponding point $\vec{q} := \mathrm{ms}(\vec{p})$ on the medial surface MS of S. The point $\vec{p}$ is located at the shortest distance from $\vec{q}$ compared with all other points on C. Therefore the map ms from a point on C to the corresponding medial surface point can be written as

$$\mathrm{ms} : C \to \mathbb{E}^3, \quad \vec{p} \mapsto \mathrm{ms}(\vec{p}) := \vec{p} + d_m(\vec{p}) n(\vec{p}) \ , \tag{3.5}$$

where $n(\vec{p})$ is the unit point normal at $\vec{p}$ and $d_m(\vec{p})$ is the Euclidean distance of $\vec{p}$ to its corresponding medial surface point $\mathrm{ms}(\vec{p})$ called medial distance [46].

In context of the pore domains $\mathcal{P}$ studied in this thesis it is important to remark that $\mathcal{P}$ is parameterized by the union

$$\mathcal{P} = MS \cup \bigcup_{\vec{p} \in \mathcal{I}} \left\{ \vec{p} + \tau \vec{n}(\vec{p}) \middle| \tau \in \left[0, d_m(\vec{p})\right) \right\} \ , \tag{3.6}$$

where MS is the medial surface of $\mathcal{P}$ and $\mathcal{I}$ the effective interface as defined in section 2.3. This result is used for the volume computation described in section 4.3.3.

In Ref. [46] an algorithm is described for the numerical computation of the MS for an oriented triangulated surface, such as the TPMS introduced in section 3.1. Therefore medial surface data is available for all surfaces that are studied in this thesis. The MS of the I-WP surface for both orientations is illustrated in Fig. 3.5.

In spirit of Eq. (3.5) the (or a, if there are more than one) narrowest point of the pore $\mathcal{P}$ is defined as

$$\mathrm{NP}\left(\mathcal{P}\right) = \min_{\vec{p} \in \mathcal{I}} \left(d_m(\vec{p})\right) \tag{3.7}$$

and the (or a) widest as

$$\mathrm{WP}\left(\mathcal{P}\right) = \max_{\vec{p} \in \mathcal{I}} \left(d_m(\vec{p})\right). \tag{3.8}$$

In Fig. 3.5 the medial surface for both orientations of the IWP surface is illustrated.

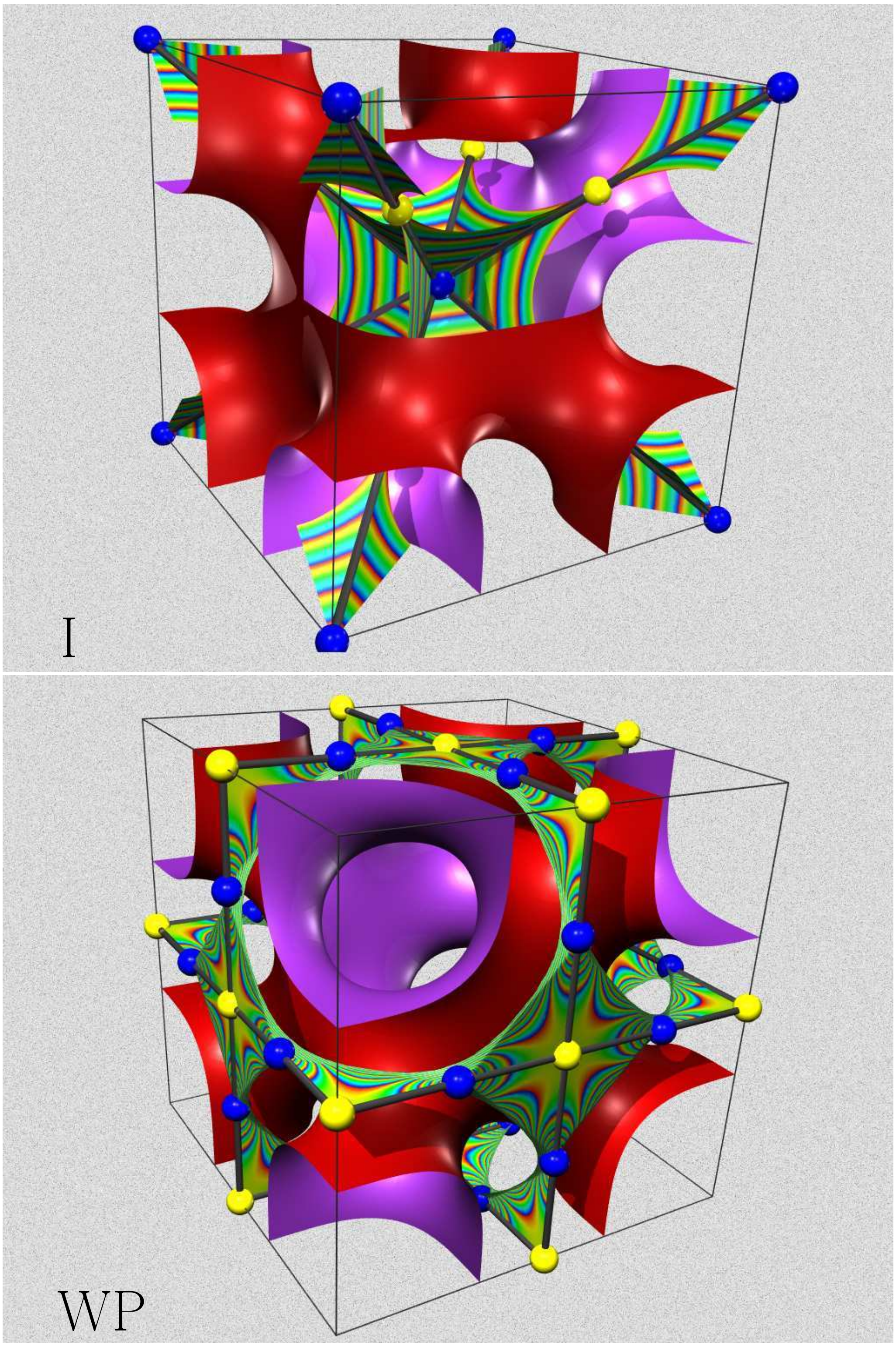

Fig. 3.5: The two medial surfaces in either of the two geometrically different channels of the I-WP TPMS for a conventional cubic unit cell: (Top) MS of the I side (Here, the surface itself is cut open for better visibility of the MS) (Bottom) MS of the WP.Blue spheres indicate maxima of the medial distance function $d(p)$ (3.5), whereas yellow spheres indicate minima of $d(p)$ along the line graphs. Note that these points are not identical with NP $(\mathcal{P})$ (3.8) and WP $(\mathcal{P})$ (3.7). Source: [47]

4 Grand Canonical Monte Carlo Simulation of Confined Hard Spheres

The main aspect of this thesis is the grand canonical Monte Carlo simulation of hard sphere systems confined to either one of the labyrinthine domains of the triply-periodic minimal surfaces introduced in chapter 3. The simulation program is used to study the equilibrium properties of such a system. As the number of particles within the system is easily measured in a computer simulation, the grand canonical ensemble is chosen as the most suitable for our purposes. The program used for the simulation is based on the work of Gerd Schröder-Turk *et al.* [13].

In section 4.1 the fundamental ideas of the Monte Carlo method are discussed. For reasons of convenience the Monte Carlo simulation is first described as a Markov process in the framework of the canonical ensemble. In section 4.2 this concept is then extended to the grand canonical ensemble, which is used in the simulation program. The main focus of this section lies in the derivation of the acceptance probabilities for particle insertion and deletion.

In the following section the actual implementation of the Monte Carlo method as a `C++` program is addressed. In particular a fast method for the computation of the substrate-sphere interaction by using a precomputed grid look-up table is described in detail. The section is also dealing with the calculation of certain geometrical quantities, e.g. the pore volume $V[\mathcal{P}]$, performed by the program. Additionally, the error calculation as implemented in the program is outlined.

An analysis of the thermodynamic consistency for the bulk fluid, i.e. an unconfined fluid, is given in section 4.4. In particular, theoretical predictions for the bulk packing fraction η, obtained from the Carnahan-Starling equation of state for hard spheres [6] and pair correlation functions, obtained by means of White Bear density functional theory [44], are compared to the simulation results. It is also asserted that the simulation is consistent in the ideal gas limit.

In the final section the simulation results for simple pore geometries (sec. 4.5.1), i.e. spherical and cylindrical pores and the simulation results for the TPMS (sec. 4.5.2) are presented. In particular, the relative difference $(\eta_0 - \eta)/\eta$ between the confined packing fraction η_0 (Eq. (2.23)) and the bulk packing fraction η (Eq. (2.24)) is presented as a function of the simulation box size and η which is related to the chemical potential μ by Eq. (4.46). It turns out, that the confined hard sphere fluid shows a complex behavior that is discussed in this section. Further, the validation of our simulation results is supported by the good agreement we find with numerical 3-dimensional DFT calculations for TPMS, carried out by Roland Roth [44].

4.1 Monte Carlo Method

This section develops the description of the Monte Carlo simulation as a Markov process in the framework of the canonical ensemble based on Ref. [20]. The next section extends the concept to the grand canonical ensemble which is used in the simulation program.

It has already been stated, that the partition function Ξ ((Eq. 2.12)) cannot be solved analytically for a hard sphere system. Therefore numerical methods are needed to approximate the average (Eq. (2.13)) of an observable $F(\vec{r}^N)$. Monte Carlo is a powerful technique to find such an approximation with the help of a computer system. For reasons of convenience, the concept is introduced in context of the canonical ensemble and then extended to the grand canonical ensemble, which is used to investigate the equilibrium properties of the confined hard sphere fluid.

The canonical ensemble average for any observable F of particle coordinates can generally be written as

$$\langle F\rangle = \frac{\int F(\vec{r}^N)\exp\left(-\beta V_N(\vec{r}^N)\right)\,\mathrm{d}\vec{r}^N}{\int \exp\left(-\beta V_N(\vec{r}^N)\right)\,\mathrm{d}\vec{r}^N}\ , \tag{4.1}$$

where $V_N(\vec{r}^N)$ is an arbitrary potential depending on particle coordinates $\vec{r}^N = \{\vec{r}_1, \ldots, \vec{r}_N\}$. Generating a large number of random configurations of particles, one might hope that it is possible to estimate the average by replacing the integrals by sums over this finite number of configurations in the sample, i.e.

$$\langle F\rangle \simeq \frac{\sum_m F(m)\exp\left(-\beta V_N(m)\right)}{\sum_m \exp\left(-\beta V_N(m)\right)}\ . \tag{4.2}$$

The sums runs from $m = 1$ to $m = \mathcal{N}$, with $\mathcal{N}$ the total number of created configurations. $V_N(m)$ denotes symbolically the total potential energy of the system in state m. This approach is somehow very inefficient, because almost all randomly constructed configurations have a vanishing Boltzmann-factor and therefore do not contribute to the sum. As consequence it is necessary to introduce some form of importance sampling. This means that regions of configuration space that contribute the most should be sampled most frequently.

To eliminate the bias created by this sampling method, one has to attach an appropriate weight to each configuration. If $W(m)$ is the probability of choosing configuration m, then Eq. (4.2) must be replaced by

$$\langle F\rangle \simeq \frac{\sum_m F(m)\exp\left(-\beta V_N(m)\right)/W(m)}{\sum_m \exp\left(-\beta V_N(m)\right)/W(m)}\ . \tag{4.3}$$

A natural choice for the weighting probability would be the Boltzmann distribution itself. Therefore by setting

$$W(m) = \frac{\exp\left(-\beta V_N(m)\right)}{\sum_n \exp\left(-\beta V_N(n)\right)} \tag{4.4}$$

one gets for Eq. (4.3)

$$\langle F\rangle \simeq \frac{1}{\mathcal{N}}\sum_{m=1}^{\mathcal{N}} F(m)\ . \tag{4.5}$$

The remaining problem is generation of random variables - that are the set of all coordinates of all particles - that are distributed according to Eq. (4.4). This can be formulated in terms of the theory of stochastic processes.

First of all, it is more convenient to refer to a certain variable in this chain as the state n of the system at a certain point rather than to speak of the value of this variable. So if the probability of finding the system in a state n at a certain "time" t is solely determined by the state m, occupied at the previous time $(t-1)$, the sequence is said to form a Markov chain. The concept of time is only introduced for descriptive purposes and has no real relation to any physical timescale.

Assume $q_n(t)$ is the probability of the system occupying state n at time t with

$$\sum_n q_n(t) = 1 \tag{4.6}$$

for all t. The Markovian character can be expressed as

$$q_n(t) = \sum_m P_{nm} q_m(t-1) \tag{4.7}$$

where the transition probability $P_{nm} \equiv \text{prob}(n, t|m, t-1)$ is assumed to be independent of t. $\text{prob}(n, t|m, t-1)$ is the probability that the system is occupying state n at time t under the condition that it is in state m at time $t-1$.

As P_{nm} can be regarded as square matrix, one can write

$$\vec{q}(t) = P\vec{q}(t-1) \ . \tag{4.8}$$

One can generalize Eq. (4.8) immediately to yield the probability distribution at a certain time t given an initial configuration $\vec{q}$:

$$\vec{q}(t) = \overbrace{P\cdots P}^{t \text{ times}} \vec{q}(0) = P^t \vec{q}(0) \ , \tag{4.9}$$

where P^t is t-fold product of P with itself. As P is a stochastic matrix, it satisfies the conditions

$$0 \leq P_{nm} \leq 1 \ , \quad \sum_n P_{nm} = 1 \quad (\text{for all } m) \ . \tag{4.10}$$

If all elements of P^t are non-zero for some finite time t, which essentially means that each state of the system can be reached from any other in a finite number of steps, then the process is said to be ergodic. This term is closely related to the meaning of ergodicity used in statistical mechanics. If the Markov process is ergodic, it can be shown that the limits

$$\Pi_n = \lim_{t\to\infty} P^{(t)}_{nm} \tag{4.11}$$

exist and are the same for all m. Taking Eq. (4.7) and the normalization condition of $q(0)$ into account, it is obvious that the column vector $\vec{\Pi} = \{\Pi_n\}$ represents a unique, asymptotic probability distribution,

$$\vec{\Pi} = \lim_{t\to\infty} \vec{q}(t) \tag{4.12}$$

which is independent of the initial configuration $\vec{q}(0)$. Once $\vec{\Pi}$ is reached, one speaks of the steady-state condition, which is expressed by the following equation:

$$P\vec{\Pi} = \vec{\Pi} \ . \tag{4.13}$$

Having set up the theoretical foundations of the Markov process, it is now useful to consider how to apply this scheme to a computer simulation. First, as our interest lies in the ensembles average of some function of particle coordinates, we have to ensure that there is a unique equilibrium distribution, i.e. our process has to be ergodic. Second, the limits in Eq. (4.9) are known for the canonical ensemble and given by the Boltzmann distribution

$$\Pi_n = \frac{\exp\left(-\beta V_N(n)\right)}{\sum_m \exp\left(-\beta V_N(m)\right)} \ . \tag{4.14}$$

By introducing the concept of microscopic reversibility or closely related detailed balance, the problem is greatly simplified. This basically means, that one is looking for transition matrices where the following equation holds:

$$\Pi_m P_{nm} = \Pi_n P_{mn} \ . \tag{4.15}$$

It can easily be shown, that the steady state condition Eq. (4.13) is automatically fulfilled under these circumstances. The remaining problem is now the proper construction of the Markov process, which is expressed in the matrix P. This leads to a brief excursus on the generation of sequences of configurations, although the detailed discussion is deferred to section 4.3, where the implementation is described.

Assume the system is in some state m at a given time t. The next step would be the transition to a state n, which is in some way adjacent to m. n is called a trial configuration. This move would consist of a displacement of a single particle in a prescribed range. The term “adjacent to” can be understood as “not very different from”. For an adequate description of the Markov process it is further useful to introduce a stochastic matrix α, whose elements α_{nm} are the conditional probabilities of choosing a trial state n. $\alpha_{nm} = 0$ for all pairs of states that are non-adjacent. One also demands that α has to be symmetric, which means that transitions in any direction should be equally probable. Then P has all the properties that are required if

$$P_{nm} = \begin{cases} \alpha_{nm} & \text{if } \Pi_n \geq \Pi_m, n \neq m \\ \alpha_{nm}\Pi_n/\Pi_m & \text{if } \Pi_n < \Pi_m, n \neq m \\ 1 - \sum_{n\neq m} P_{nm} & \text{if } n = m \end{cases} \ . \tag{4.16}$$

The transition matrix defined by Eq. (4.16) was proposed by Metropolis et al. [34] and remains the most commonly used prescription for P. Although one can think of more complicated realizations of the detailed balance condition, the Metropolis scheme appears to result in a more efficient sampling of configuration space than most other strategies that have been proposed [3, 12]. It is also important to point out, that the fundamental part of the definition lies in ratio Π_n/Π_m, as the introduction of α is merely due to the proper definition of the Markov process itself. α is often called the underlying matrix of the Markov chain.

4.2 Grand Canonical Monte Carlo

Having set up the theoretical foundations of the Markov process, it is now necessary to extend the concept to the grand canonical ensemble that is used for the simulation. To be more specific, the (μ, V, T)-ensemble is used, although the temperature dependence can be omitted, because for hard core interactions, as employed here, there is no energy scale to be compared to the thermal energy $k_\mathrm{B}T$. Especially the derivation of the insertion and deletion probability is carried out in detail, as there was some confusion regarding this issue during my thesis project.

The method we use goes back to Norman and Filinov [37]. In this technique, there are three different types of transition:

(a) displacement of a particle;

(b) insertion of a particle;

(c) deletion of a particle.

The compulsory ergodicity requirement is obviously fulfilled for this scheme. It is also shown in Ref. [37], that transitions involving more than one particle, e.g. the displacement of two particles, is not effective, because of a high rejection rate. Therefore the corresponding states are regarded as non-adjacent. It is possible to apply the Metropolis scheme of section 4.1 for all moves of type (a). In contrast state transitions of type (b) and (c) need a proper examination to define the values of P_{nm} correctly.

The detailed balance condition Eq. (4.15) of the process can be rewritten as

$$\mathrm{acc}(o \to n) \cdot \alpha(o \to n) \cdot P(o) = \mathrm{acc}(n \to o) \cdot \alpha(n \to o) \cdot P(n) \ , \tag{4.17}$$

where $P(o)$, $P(n)$ denote the Boltzmann weights for an “old” configuration o and a “new” configuration n. $\alpha(o \to n) = \alpha_{no}$ and $\alpha(n \to o) = \alpha_{on}$ are the values of the underlying matrix α, i.e. the probabilities for generating such a move. It turns out that for this method α is not symmetric for a transition of type (b) and (c). The acceptance probabilities $\mathrm{acc}(n \to o)$ and $\mathrm{acc}(o \to n)$ need to be defined, so that P_{nm} fulfills the detailed balance condition. Applying the Metropolis scheme one obtains:

$$\mathrm{acc}(o \to n) = \min\left(1,\ \frac{\alpha(n \to o)}{\alpha(o \to n)} \cdot \frac{P(n)}{P(o)}\right) \tag{4.18}$$

$$\mathrm{acc}(n \to o) = \min\left(1,\ \frac{\alpha(o \to n)}{\alpha(n \to o)} \cdot \frac{P(o)}{P(n)}\right) \ . \tag{4.19}$$

It can be easily verified that Eq. (4.17) is satisfied. The remaining question is the proper identification of α and the Boltzmann weights. As a transition is restricted to insertion or deletion of only one particle, the following quantities are sufficient. The ratio

$$\frac{P(C_{N+1})}{P(C_N)} = \Lambda^{-3} e^{\beta\mu} e^{-\beta(V_{N+1}-V_N)} \ , \tag{4.20}$$

where $C_N = \{\vec{r}_1, \vec{r}_2, \cdots, \vec{r}_N\}$ denotes an arbitrary configuration with N particles. The detailed derivation of this expression is found on Ref. [48]. Furthermore

$$\alpha(N \to N+1) = \frac{1}{c} \cdot \frac{1}{V} \tag{4.21}$$

as probability for a trial insertion of a particle uniformly anywhere in the prescribed volume. The probability for randomly picking one particle for a trial deletion is

$$\alpha(N+1 \to N) = \frac{1}{c} \cdot \frac{1}{N+1} \ . \tag{4.22}$$

The factor $1/c$ accounts for the equal probabilities of the insertion and deletion process. We also demand, that $1/2 \geq 1/c \geq 0$, so that $1 - 2/c$ is the probability for attempting a displacement of a particle.

Taking these results and substituting them into Eq. (4.19) yields:

$$\mathrm{acc}(N \to N+1) = \min\left(1,\ \frac{V}{N+1} \cdot z \cdot \exp[-\beta(V_{N+1} - V_N)]\right) \tag{4.23}$$

$$\mathrm{acc}(N \to N-1) \ = \min\left(1,\ \frac{N}{V} \cdot z^{-1} \cdot \exp[-\beta(V_{N-1} - V_N)]\right) \tag{4.24}$$

It shall be noted that a different approach is given in many textbooks [12, 36]. There α is assumed to be symmetrical using the concept of a mixed system containing real and fictitious (ideal gas) particles where the total number of particles is fixed. This eventually leads to the same probabilities as presented here though the derivation is different.

For a hard sphere system Eq. (4.23) and Eq. (4.24) further simplify to

$$\mathrm{acc}(N \to N+1) = \min\left(1,\ \frac{V}{N+1} \cdot z\right) \tag{4.25}$$

$$\mathrm{acc}(N \to N-1) = \min\left(1,\ N \cdot (zV)^{-1}\right) \tag{4.26}$$

in case the insertion created no overlap. From the Metropolis scheme in Eq. (4.16) follows that displacements are unconditionally accepted if they create no overlap and vice versa for hard sphere systems.

As has been shown in section 2.3, the fugacity z is independent of the thermal wavelength. Hence, Λ can be set to any constant non-zero value without changing the insertion and deletion probability. This also implies that the equilibrium properties remain unchanged for any choice of Λ. For reasons of convenience the thermal wavelength is chosen in a way that $\beta\mu_{\mathrm{id}} = \ln\eta$, with η as the bulk packing fraction. Therefore:

$$\Lambda^3 = \frac{4}{3}\pi R^3 = V_{\mathrm{sph}} \ . \tag{4.27}$$

It shall be remarked that the Grand Canonical Monte Carlo simulation works particularly good for packing fractions $\eta \leq 0.4$. For higher densities the sampling method becomes inefficient due to a high rejection rate for both insertions and displacements. Nevertheless this range is suitable for the comparison to DFT theories, as they also work best in this η range.

The starting point for the Monte Carlo sampling is the generation of an initial configuration i. In general there are no restrictions on i beside a non-vanishing probability according to the Boltzmann distribution. For a confined hard sphere system this means that there is no sphere-sphere and no sphere-solid overlap. Although the asymptotic probability distribution of the Markov process is unique (see Eq. (4.12)) irrespective of the initial configuration, one has to bear in mind that only a finite number of states can be sampled in a computer simulation. As our interest lies only in systems with low to medium packing fractions, it is sensible to start with a very low preset number of particles $N_p = 10$ to speed up the initialization process, although it might not always be the optimal starting configuration. As a consequence the determination of the relaxation time, i.e. the number of moves until the system is in equilibrium, is important and addressed in this section 4.3.

4.3 Implementation of the Monte Carlo Method

Having set up the theoretical foundations of the Grand Canonical Monte Carlo (GCMC) simulation, the realization on a computer system as a `C++` program is discussed. The main features of the software are described and it is explained how the simulation results were obtained. Furthermore, the program's additional useful functions, e.g. the computation of the area of the confining geometry, are briefly described.

4.3.1 Simulation of Confined Hard Sphere Fluids

In practice the initialization is done in the following way. The simulation box $\mathbb{P}$ is chosen to be a rectangular translational unit cell of the periodic confining geometry, but not necessarily its primitive or smallest translational unit cell. The description in the thesis is restricted to surfaces with either cubic or tetragonal unit cells with lattice translations vectors $L_x \vec{e}_x$, $L_y \vec{e}_y$ and $L_z \vec{e}_z$ with Cartesian unit vectors $\vec{e}_x$, $\vec{e}_y$ and $\vec{e}_z$. By convention, the simulation box origin is set to (0,0,0), so that $\mathbb{P} = [0, L_x] \times [0, L_y] \times [0, L_z]$ with volume $V_{\mathbb{P}}$[1] $= L_x L_y L_z$. Therefore the applied periodic boundary conditions are easy to implement. The surface data is provided by a poly input file (see section 3.1). As the radius of the spheres is fixed, the volume V is one the free input parameters of the simulation. Then the prescribed number of particles N_p is randomly inserted within the bounds of the simulation bound obeying the no overlap restriction.

Now a MC step is performed. A MC step is defined as a sequence of $3N_T$ transition attempts. One transition attempt can either be a trial displacement of one particle with probability $(1 - 2/c)$ or a trial insertion/deletion with equal probabilities $1/c$ (see section 4.2). As it has been shown in Ref. [37] that equal probabilities for all three transition types are the most efficient, $1/c = 1/3$ in our simulations. The intuitive choice for N would be the maximal number of spheres that fit into the pore. However, that is too complicated to compute for a complex geometry in general, and we choose simply the volume of the simulation box V divided by the sphere volume V_{sph}, i.e.

$$N_T = \frac{V}{V_{\text{sph}}} \; . \tag{4.28}$$

---

[1] The index $\mathbb{P}$ is omitted in the following, so that V always refers to the volume of the current simulation box. This is consistent with Eq. (4.23).

In the case of a trial displacement, a randomly chosen sphere i currently positioned at $\vec{r}_i$ is moved by a small prescribed value λ in a random direction. This is done by creating a shift vector $\vec{s}$, that is uniformly distributed on the unit sphere and by testing if the sphere creates overlap at its new position $\vec{r}_i + \lambda\vec{s}$. If not, the new position is stored, otherwise the sphere remains at $\vec{r}_i$. In our realization λ is set to $0.2R$ because larger values generate displacements that are more likely to be rejected, especially for higher densities.

A trial insertion consists of two steps. First, the acceptance condition (4.25) is checked. A random number q, uniformly distributed on $[0, 1]$ is generated. After this the inequality

$$q < \frac{V}{N+1} \cdot z \tag{4.29}$$

is evaluated. If Eq. (4.29) holds, the program moves on to step two, otherwise the trial insertion is already rejected. The second step is marked by the generation of a trial position $\vec{r}_t$ that is equally distributed within the simulation box. In case a trial sphere at $\vec{r}_t$ creates overlap the insertion is rejected, otherwise accepted. It has to be remarked that the step order is important regarding the program's efficiency, as the overlap check is very time consuming. Nevertheless the implementation would be also correct if the steps were interchanged.[2]

The trial deletion also consists of two steps. Step one is equal to the insertion case, expect the inequality

$$q < N \cdot (zV)^{-1} \tag{4.30}$$

is checked this time according to the acceptance probability for a trial deletion Eq. (4.26). In step two a randomly chosen particle is deleted.

Now a certain number of MC steps N_{sbm} (sbm: "steps between measurement") has to be performed until the system is in equilibrium. N_{sbm} is an input parameter of the program. The relaxation time is determined in the following way. For the same input parameters μ and V a test simulation is run where the value of some measured quantity, e.g. the average number of particles in the simulation box, is recorded for every MC step. By observing the obtained data, a step number is determined after which the measured quantity is obviously fluctuating around some average value (see Fig. 4.1). To account for statistical uncertainties this number is multiplied by a factor of two to finally yield N_{sbm}.

As the system is considered to be in equilibrium now, values of any function of particle coordinates F can be accumulated. This is done by recording the value of F in intervals of the input parameter N_{ibm} (ibm: "intervals between measurement"). After a total number of steps N_{total} (input parameter) the simulation is finished and the approximation of $\langle F \rangle$ (Eq. (2.13)) is calculated by the averaging F over the sampled configurations (see Eq. 4.5)

$$\text{AVRG}\,(F) = \frac{1}{N_{\text{sc}}} \sum_{m=1}^{N_{\text{sc}}} F(m) \ , \tag{4.31}$$

---

[2] In fact, this is possible for the hard sphere system, as the potential V_N is either 0 or ∞. For general potentials the position of the trial particle would be crucial for the computation of the insertion probability.

where N_{sc} is the total number of sampled configurations. Note that we are using the notation of Ref. [25]. N_{sc} is given by

$$N_{\text{sc}} = \left\lceil \frac{N_{\text{total}} - N_{\text{sbm}}}{N_{\text{ibm}}} \right\rceil . \tag{4.32}$$

The ceiling function $\lceil \cdot \rceil$ assures that N_{sc} is an integer number.[3] The whole procedure, from the initiation to the averaging of the measured quantities, is defined as a MC run. It also possible to have N_{runs} multiple runs. The results of the single runs are merged and the average calculated by

$$[F] = \frac{1}{N_{\text{runs}}} \sum_{m=1}^{N_{\text{runs}}} \text{AVRG}\,(F)_i \ , \tag{4.33}$$

where $\text{AVRG}\,(F)_i$ refers to the average over all sampled configurations of the i-th run.

Now we have a short discussion on the choice of N_{ibm}. Remarks on N_{total} and N_{runs} are deferred to section 4.3.4 as they are closely related to the error calculation, which is explained there. Conceptually it would be correct to measure a quantity F after every single transition attempt (whether successful or not). Although one accumulates a lot of data that way, a single measurement of F is highly correlated to values of F obtained shortly before and after. Hence, its contribution to the average Eq. (4.31) is negligible. The concept of correlation time, i.e. the number of transition attempts this correlation persists, is discussed in Ref. [3]. Although this issue seems only to be an inconvenience, the main downside is of numerical nature. The simulation program computes the average of F after the n-th measurement by

$$\text{AVRG}\,(F)_n = \text{AVRG}\,(F)_{n-1} - \frac{1}{n}\,\text{AVRG}\,(F)_{n-1} + \frac{1}{n} F_n \ , \tag{4.34}$$

where $\text{AVRG}\,(F)_n = 1/n \cdot \sum_{i=1}^{n} F_i$ and F_n the measured value. Therefore it is not desirable that $N_{\text{sc}} / \text{AVRG}\,(F) \gg 1$ because of numerical precision problems in Eq. (4.34). Furthermore N_{sc} must not exceed numerical limits. Hence, it is more sensible to measure less but uncorrelated data. As a consequence N_{ibm} is chosen in a way that successive measurements can be considered uncorrelated. Especially for higher densities N_{ibm} is scaled up, as successive measurements tend to become more correlated, because of higher rejection rates of insertion and displacement transitions. Admittedly our simulations are clearly below those critical thresholds. Nevertheless this approach is fruitful for future projects were higher precision is needed.

4.3.2 Fast Substrate-Sphere Interaction

The challenge is to ensure that each sphere-solid overlap test only takes $\mathcal{O}(M)$ time, where M is the number of triangles of the discretized solid-pore interface. Therefore an improved algorithm for the substrate-sphere overlap check is needed for the complex TPMS geometries, compared to the basic implementations. This scheme is presented here.

---

[3] Therefore the simulation is finished after $N_{\text{total}} + c$ steps, where c assures that $N_{\text{total}} - N_{\text{sbm}}$ is a multiple of N_{ibm}.

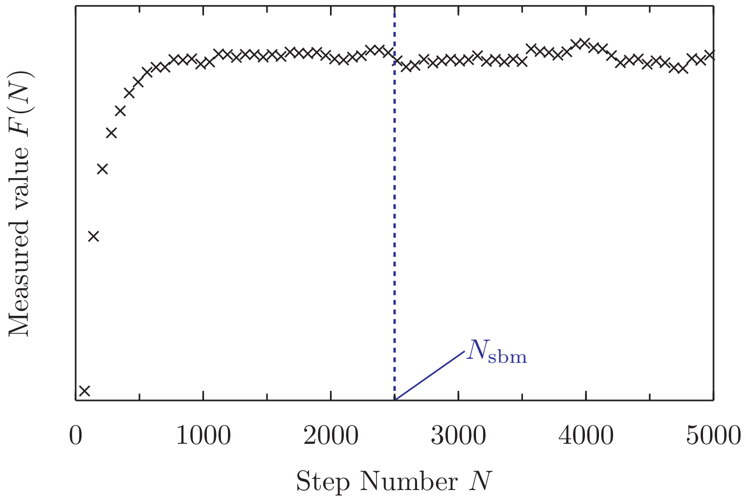

Fig. 4.1: Determination of the relaxation time for a given set of input parameters. A test simulation is run for same input parameters and the value of a measured quantity F is recorded for every MC step. F is starting to fluctuate about some average value after approximately 1000 Monte Carlo steps. To account for statistical uncertainties, the systems is considered to be in equilibrium after $N_{\mathrm{sbm}} = 2500$ steps. In the simulation the amount of MC steps performed before the actual measurement is set to N_{sbm}.

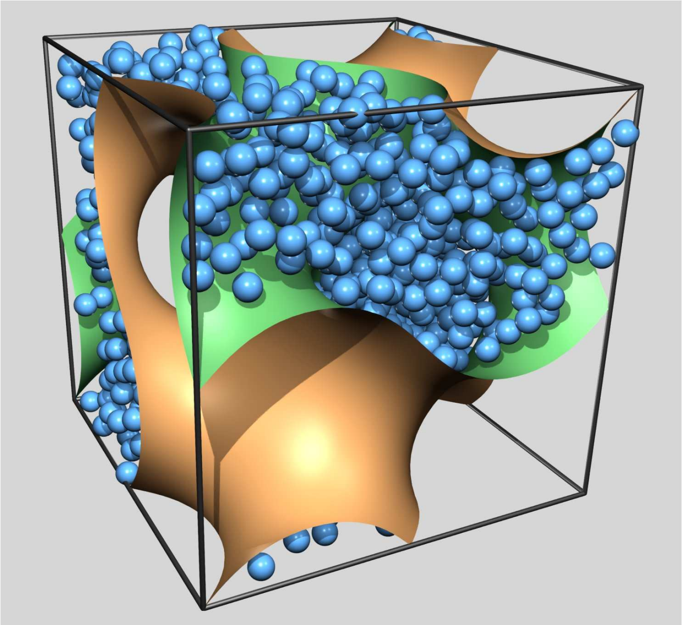

Fig. 4.2: Snapshot of a hard sphere liquid confined to one of the domains given by the Gyroid cubic minimal surface with lattice size $L = 17\sigma$. The cubic frame is the simulation box $\mathbb{P}$ which in turn corresponds to a translational unitcell of the surface (here the cubic unitcell $L_x = L_y = L_z = L$).

The solid phase is represented by an oriented triangulated surface, as stated in section 3.1. As a basic implementation of the test whether a sphere of radius R at a given position $\vec{r}$ overlaps with the solid phase, the nearest triangle to $\vec{r}$ is identified, and the signed distance from $\vec{r}$ to the triangle analyzed. If it is negative (meaning inside the solid phase) or smaller than R (meaning in the pore phase but too close to the pore/solid interface) a sphere at $\vec{r}$ is not fully contained in the pore domain, otherwise it is. This test works accurate for smooth triangulated surfaces, where the angle between adjacent triangles is below a certain threshold.

Our implementation improves this scheme by introducing a precomputed cubic grid lookup table where each voxel has either of the following status: (a) voxel in solid phase or so close to the interface that any sphere of radius R positioned anywhere in the voxel overlaps with solid, (b) voxel so deep in pore phase that all spheres positioned anywhere in the voxel are fully contained in pore, and (c) spheres in this voxel may or may not overlap with solid depending on their exact position. For case (c), the voxel also specifies a list of those triangles that may overlap with spheres in this voxel; the basic test described above needs to be applied only to these triangles. Using this look-up table the simulations are only approximately a factor of 2 to 10 slower for confined fluids than for a simple bulk simulation (for pore geometries used in this thesis). The computational effort clearly depends on the number of triangles of our input geometry. Therefore the choice of the quality of the triangulation is influenced by two counteracting effects. On the one hand a fine triangulation represents a very good approximation of the analytic surface. Thus the geometrical properties, e.g. volume or surface area, are precisely reproduced. On the other hand the computation time increases rapidly with increased number of triangles. Hence it is important to find a compromise. We achieved good results with 10^4 - 10^5 triangles per translational unit cell.

The creation of the look-up table is conceptually straightforward: A cubic grid of size $N_x \times N_y \times N_z$ with grid spacing Δ is created that covers (at least) the whole simulation box $\mathbb{P}$. The number of subdivisions N_x (and accordingly N_y and N_z that are usually given by the aspect ratio of $\mathbb{P}$) should be chosen as high as possible to speed up the simulation. The surface representation of the confining solid is always assumed to extend beyond $\mathbb{P}$, so that there are not any open surface boundaries in $\mathbb{P}$. The creation of the lookup table described above involves the evaluation of the signed Euclidean distance map [47] to the surface. For each cube of the lookup table grid, the signed distance D from its center to the nearest point of the pore/solid interface surface is computed. The sign determines if a point is in the pore or in the solid phase (positive in the pore phase by convention). Based on the value of D the assignment of the voxel status as described above is simple: If $D \leq \max\{0, R - \sqrt{3}\Delta/2\}$, including in particular all negative values, the cube cannot contain any spheres that do not overlap with the solid phase (a). Similarly, if $D > R + \sqrt{3}\Delta/2$ the cube cannot contain any spheres that overlap with the solid (b). All remaining cubes are ones in which the overlap of a sphere of radius R with the solid depends on the precise position of that sphere in the cube . For each of these cubes a list of all triangles that are closer than R to the borders of the cube are stored to facilitate the overlap test (c). This completes the construction of the look-up table. A predicate overlap($\vec{r}$) is implemented based on this lookup table that returns true if a sphere of radius R at $\vec{r}$ overlaps with the solid, and false otherwise. Only in the case (c) is it necessary to actually compute the distances from $\vec{r}$ to triangles of the surface, and only to a small set of surface triangles

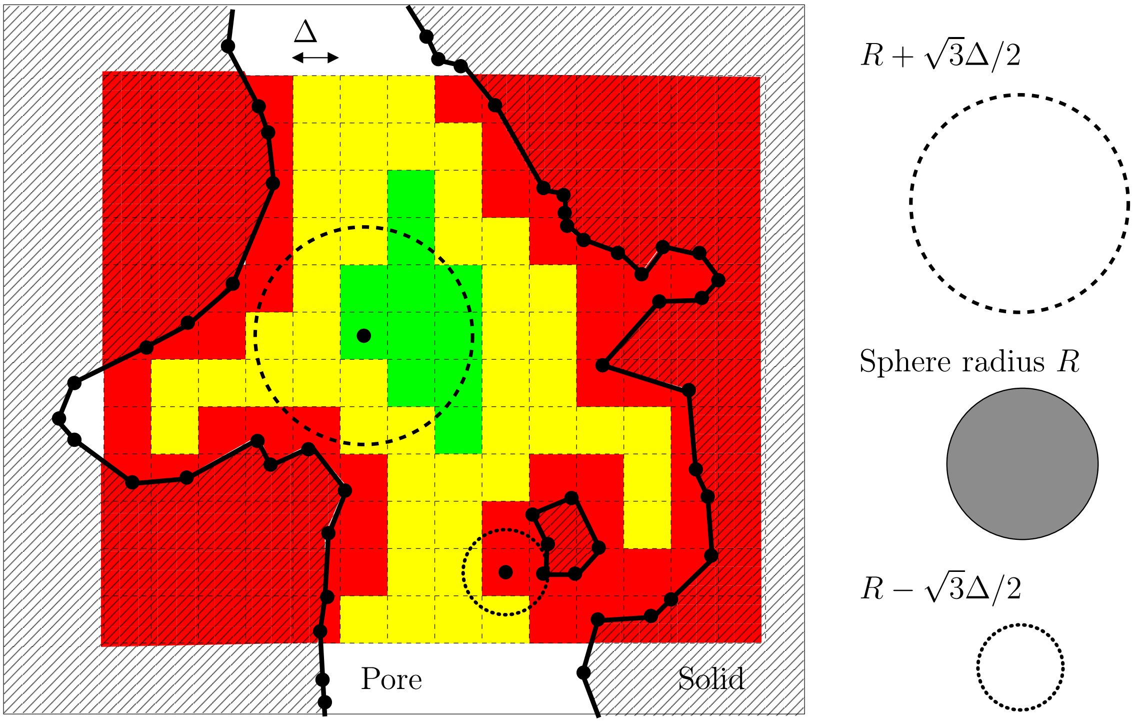
Δ
Pore
Solid
$R+\sqrt{3}\Delta/2$
Sphere radius R
$R-\sqrt{3}\Delta/2$

🟩 No sphere in this voxel can overlap with solid

🟥 Any sphere in this voxel overlaps with solid

🟨 Spheres in this voxel may or may not overlap with solid

Fig. 4.3: Look-up table for fast but exact test whether a hard sphere of radius R overlaps with the solid phase or not. A detailed description is given in this section.

stored in the corresponding list. This ensures the constant-time performance of the predicate. See Fig. 4.3.

The computation of the Euclidean distance for all grid points involves in its most elegant and fast form point-proximity queries from computational geometry [39]; these are complicated to implement. We have chosen a slower but simpler approach that exploits the fact that we only need the Euclidean distance values up to a maximum of $R + \sqrt{3}\Delta/2$. First we determine for each cube all triangles of the solid-pore interface that are closer than $R + \sqrt{3}\Delta/2$ (a secondary basic lookup table for triangles is used to ensure that this search is a constant-time operation in the total number of triangles). For each cubes that has any such triangles the signed Euclidean distance is determined by searching for the nearest of the triangles of this cube, and decide which of the three cases applies to this cube. All remaining cubes are either case (a) or (b). This assignment is easily performed by iteratively setting all as yet unassigned neighbours of cubes of case (a) to (a), and similarly for the case (b). As the interface surface is required to subdivide the simulation box $\mathbb{P}$ into a pore and a solid body, i.e. in particular that it has no open boundaries in $\mathbb{P}$, this iterative approach yields the correct assignment for all cubes.

4.3.3 Geometrical Calculations

An additional functionality of the program is the computation of certain geometrical quantities of the input geometry. These are the volume of the pore $V[\mathcal{P}]$, the surface area $A[\mathcal{P}]$, the integrated mean curvature $C[\mathcal{P}]$ and the Euler number $X[\mathcal{P}]$. The calculation methods are briefly described in this section.

Pore Volume $V(\mathcal{P})$ As the volume calculation for an arbitrary input geometry is difficult, this function is only available for surfaces with medial surface data (see section 3.3). The algorithm exploits the fact that it is possible to parameterize the pore domain according to Eq. (3.6). The general idea is to successively generate parallel surface layers by shifting each vertex $\vec{v}_i$ in normal direction $\vec{n}_i$ towards its corresponding medial surface point $\vec{m}_i$ with $i = 1 \dots N_v$ (N_v : Total number of vertices). This is done until each vertex coincides with its corresponding medial surface point. The volume between those layers is accumulated, to finally yield the whole pore volume $V(\mathcal{P})$. A more precise formulation is given now.

The whole process consists of $M = 50$ steps. In the j-th step ($j = 1 \dots 50$), the following points are calculated

$$\vec{p}_i = \vec{v}_i + \min\left((j-1) \cdot \Delta r, d_m(\vec{v}_i)\right) \cdot \vec{n}_i \ , \tag{4.35}$$

$$\vec{q}_i = \vec{v}_i + \min\left(j \cdot \Delta r, d_m(\vec{v}_i)\right) \cdot \vec{n}_i \tag{4.36}$$

where $\Delta r = \max_i(d_m(\vec{v}_i))$ is the maximal medial distance of all vertices, $d_m(\vec{v}_i)$ is the medial distance of the i-th vertex and $\vec{n}_i$ its point normal. For each triangle k of the original triangulated surface denoted by its vertices ($\vec{v}_{k(1)}$, $\vec{v}_{k(2)}$, $\vec{v}_{k(3)}$) the volume of the polyhedron P_{jk} is calculated. P_{jk} is defined by the triangles ($\vec{p}_{k(1)}$, $\vec{p}_{k(2)}$, $\vec{p}_{k(3)}$), ($\vec{q}_{k(1)}$, $\vec{q}_{k(2)}$, $\vec{q}_{k(3)}$) and the connected lines between ($\vec{p}_{k(l)}$, $\vec{q}_{k(l)}$), with $l \in \{1, 2, 3\}$. The volume of the polyhedrons is accumulated to finally yield the volume of parallel layer $\sum_k vol(P_{jk})$. This marks the end of j-th step.

The whole pore volume is then given by

$$V(\mathcal{P}) = \sum_{j,k} vol(P_{jk}) \ . \tag{4.37}$$

The min function in Eq. (4.35) ensures, that the maximal displacement length does not exceed the medial distance for each vertices. According to the definition of Δr, $\vec{q}_i = \vec{m}_i$ for all vertices i for the M-th step. That means no further step is required, as all points coincide with their corresponding medial surface points and volume calculation is complete. Accurate volume approximation is achieved with this method. The relative volume difference $(V_{\text{analytic}} - V_{\text{triang.}})/V_{\text{analytic}}$ for the analytic and the triangulated representations of the TPMS is below 10^{-4}. Nevertheless, one has to bear in mind, that the quality of the triangulation is also influencing this quantity.

Computing the parallel layers only up to a distance of R might be a good alternative to the analytic calculation of the excluded volume $V(\mathrm{P}_{\text{ex}})$ (see sec. (2.3)). Although not implemented yet, this might be of purpose for future projects.

Area A and Integrated Mean Curvature C The surface area is simply calculated by sum over the area of each triangle. The computation of the integrated mean curvature $C = \int_A \mathrm{d}H$ is carried out as a sum over the edge angles of adjacent triangles. But as most of the examined surfaces in this thesis have vanishing mean curvature anyway, this shall not be discussed here. In Ref. [14] the method is described in detail.

Euler number X The computation of the Euler number as defined in Eq. (2.1) makes direct use of the Gauss-Bonnet theorem for triangulated surfaces.. Therefore

$$X = \frac{1}{2}(N_V - N_E + N_F) \tag{4.38}$$

where N_V is the number of vertices, N_E the number of edges and N_F the number triangles. The edges and vertices have to be taken with weight 1, 1/2 or 1/4 if they appear inside, at the face or at the edge of the simulation box respectively. The 1/2 in Eq. 4.38 accounts for consistency with the definition of X given in section 3.1.

4.3.4 Error Estimation

4.3.4.1 Standard Error Calculation

In this section we derive an expression for the error estimation of some quantity F which is measured over a certain number N_{sc} of equilibrium configurations, i.e.

$$\text{AVRG}\,(F) = \frac{1}{N_{\text{sc}}} \sum_{m=1}^{N_{\text{sc}}} F(m) \ . \tag{4.39}$$

We stick to the notation used in [25] p. 104. Assuming that there is no correlation between F_i and F_j for $i \neq j$ and that all F_i are equally distributed, then the variance would simply be given by

$$\sigma^2(\text{AVRG}\,(F)) = \frac{\sigma^2(F)}{N_{\text{sc}}} \tag{4.40}$$

where

$$\sigma^2(F) = \text{AVRG}\left((F - \text{AVRG}\,(F))^2\right) = \frac{1}{N_{\text{sc}}} \sum_{i=1}^{N_{\text{sc}}} (F - \text{AVRG}\,(F))^2 \ . \tag{4.41}$$

But in practice, we cannot generally make the assumption that our data points are totally uncorrelated, as already stated in section 4.3. If we evaluate certain quantities sufficiently frequently, e.g. every MC step, our results are going to be highly correlated. There are some approaches that deal with that problem directly by introducing a correlation "time", which tells us how long this correlation persists [3]. As this approach is somehow difficult to realize, we chose a simpler one.

4.3.4.2 Implemented Error Calculation

The average of F over all N_{runs} runs is defined as (cf. (4.33))

$$[F] = \frac{1}{N_{\text{runs}}} \sum_{i=1}^{N_{\text{runs}}} \text{AVRG}\,(F)_i \ . \tag{4.42}$$

The idea is now to consider the averages $\text{AVRG}\,(F)_i$ of each single runs as uncorrelated and equally distributed random variables. According to (4.41) the variance of $[F]$ is given by

$$\sigma^2([F]) = \frac{\sigma^2(\text{AVRG}\,(F))}{N_{\text{runs}}} \tag{4.43}$$

where

$$\sigma^2(\text{AVRG}\,(F)) = \frac{1}{N_{\text{runs}}} \sum_{i=1}^{N_{\text{runs}}} (\text{AVRG}\,(F)_i - [F])^2 \ . \tag{4.44}$$

The estimated error in the mean over all runs is then given by

$$\sigma([F]) = \frac{1}{\sqrt{N_{\text{runs}}}} \sqrt{\sum_{i=1}^{N_{\text{runs}}} (\text{AVRG}\,(F)_i - [F])^2} \ . \tag{4.45}$$

The aforementioned choice of the input parameter N_{total} and N_{runs} is discussed in the following. In principle the decision was made based on two main arguments:

(a) reasonable, predictable simulation time

(b) small relative errors $\sigma([F])/[F] \approx 10^{-4}$

As the program was run on a high performance parallel computer, where maximal simulation time was set to 24 hours, point (a) was especially important. Good results were achieved with $N_{\text{total}} = 20000$, $N_{\text{runs}} = 64$ (640 for higher precision runs) and $N_{\text{ibm}} = 30-70$ depending on density of the hard sphere system with simulation box size 8^3, 17^3 and 34^3.

It has to be pointed out, that the simulation has not yet been optimized regarding runtime and corresponding error. Our main focus was on the creation of datasets for many different surfaces in a wide spectrum of μ values for different simulation box sizes to compare them to the morphometric approach of chapter 5.

4.4 Thermodynamic Consistency for the Bulk Fluid

This section demonstrates that the Monte Carlo implementation is thermodynamically consistent and produces correct results for the bulk fluid, i.e. without confinement.

In particular, the simulation data for the bulk packing fraction η is compared to the Carnahan-Starling DFT theory [6], for packing fractions $\eta \leq 0.4$, as the theoretical approximations are good within this range. The implicit analytic expression for η reads:

$$\beta\mu = \frac{\eta(8 + 3\eta(\eta - 3))}{(1-\eta)^3} + \ln\eta \ . \tag{4.46}$$

It is derived by using the expression for the excess free energy A^{ex} given in Ref. [20] for the Carnahan Starling EOS and the thermodynamic relation

$$\left(\frac{\partial A^{\text{ex}}}{\partial N}\right)_{T,V} = \mu_{\text{ex}} \ . \tag{4.47}$$

Note that the ideal gas contribution is assumed to be $\ln\eta$, which is possible by choosing the thermal wavelength Λ accordingly. In the case of our hard spheres system Λ^3 is set to the sphere volume V_{sph}. This is in agreement with the choice in section 4.2. The inversion of Eq. (4.46) is done numerically to obtain $\eta(\mu)$ and the resulting comparison to the simulation is found in Fig. 4.4. We are later going to refer to a corresponding bulk packing fraction of the particle reservoir for a simulation in a confined geometry at a certain chemical potential μ. By this we mean the value of $\eta(\mu)$ as derived here.

As stated above the equilibrium properties of the hard sphere system do not depend on the choice of the thermal wavelength. This is reflected in the simulation data. A bulk fluid has been simulated with same parameters as in Fig. 4.4 except that Λ^3 was set to $V_{\text{sph}}/8$. The result is shown in Fig. 4.5. A change of the thermal wavelength leads to a constant shift of the absolute energy of the system. But as we are only interested in relative values, a redefinition of the chemical potential μ to $\mu' = \mu - \ln 8$ reproduces the same behavior as already seen. Therefore the equilibrium properties of the fluid are not affected by the choice of Λ. Nevertheless one has to make sure that the definitions are equivalent while comparing the results to external data.

Furthermore it is demonstrated that the two point correlation function $g(r = |\vec{r}|)$ is in good agreement with results obtained by DFT calculations based on the White Bear functional [44] for packing fractions $0.2 \leq \eta \leq 0.4$ (see Fig. 4.6). It has been shown in Ref. [45] that

$$g(r) \overset{r\to\infty}{\longrightarrow} \frac{A}{r} e^{-r/\xi} \cos\left(ar + \theta\right) \ , \tag{4.48}$$

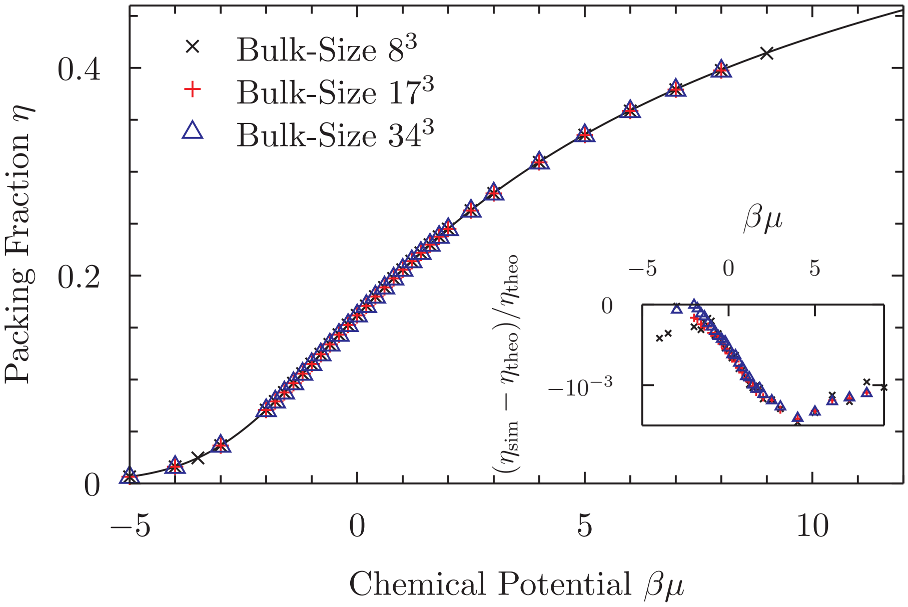

Fig. 4.4: Packing fraction η simulated for different chemical potentials μ. The solid line represents the Carnahan-Starling approximation, whereas the symbols are the result of the GCMC simulation in a cubic simulation box of edge length $L = 8$, 17 or 34. The inset shows the relative difference between simulation and theory for the three different box sizes.

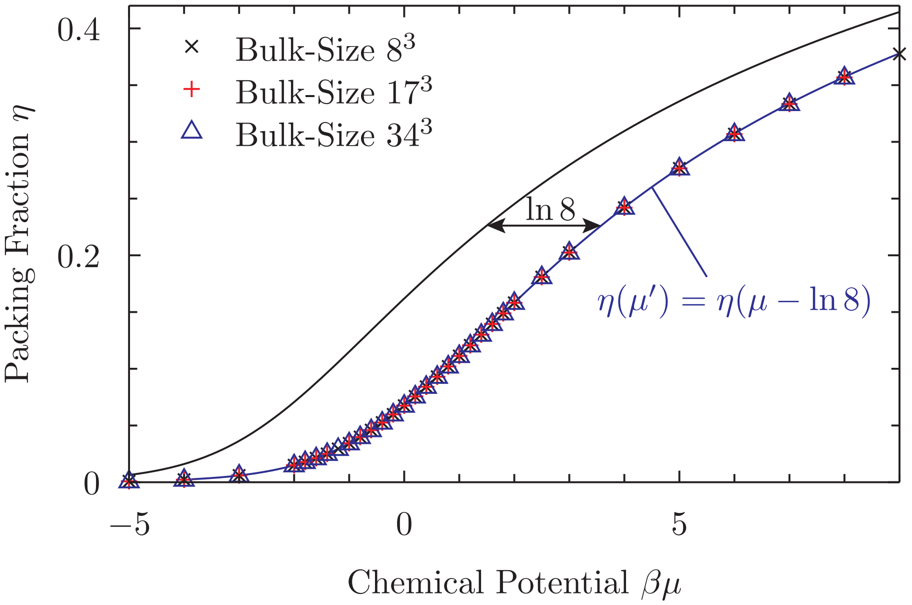

Fig. 4.5: The simulation results for the definition $\Lambda^3 = V_{\rm sph}/8$. A redefinition of the chemical potential $\mu' = \mu - \ln 8$ reproduces the same results as shown in Fig. 4.4. As expected, the thermodynamic equilibrium properties do not depend on the choice of the thermal wavelength.

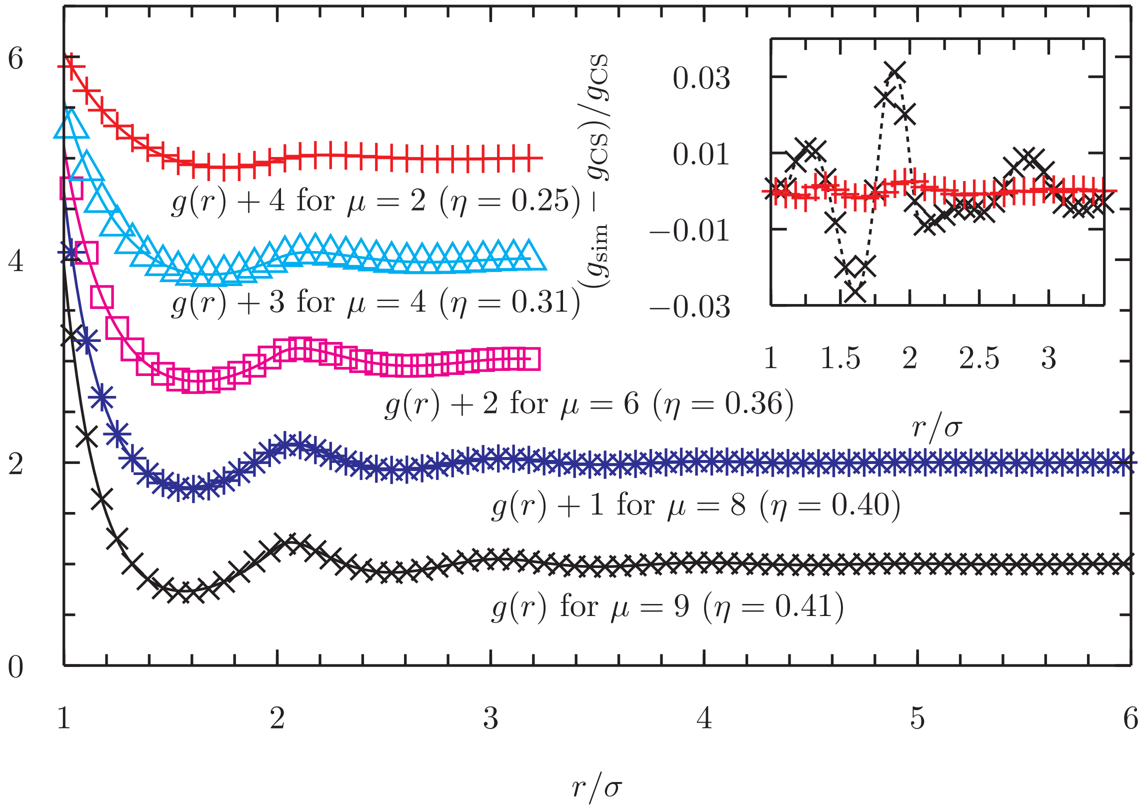

Fig. 4.6: Two Point correlation function $g(r)$ of unconfined hard sphere fluids. Symbols are the result of GCMC simulation in a cubic box of size $L = 17$. Lines represent $g(r)$ in Carnahan-Starling approximation. The inset show the relative difference between theory and simulation for the densest (black) and the least densest case (red).

with the correlation length ξ and constants A, a and a phase shift θ. The correlation length is a measure for the persistence length of sphere-sphere correlations as well as sphere-solid correlations [45]. It has to be remarked that ξ increases for denser systems. As the envelope of the oscillations of the two point correlation functions $g(r)$ in Fig. 4.6 is proportional to $e^{-r/\xi}/r$, this is also seen in our simulation data.

As a final consistency check, the ideal gas limit of the bulk fluid is studied. In the limit of small densities, the excess part of the chemical potential (see Eq. (2.28) has to converge to zero. In Fig. 4.7 it is demonstrated that the simulated bulk fluid behaves in the proper way for different simulation box sizes.

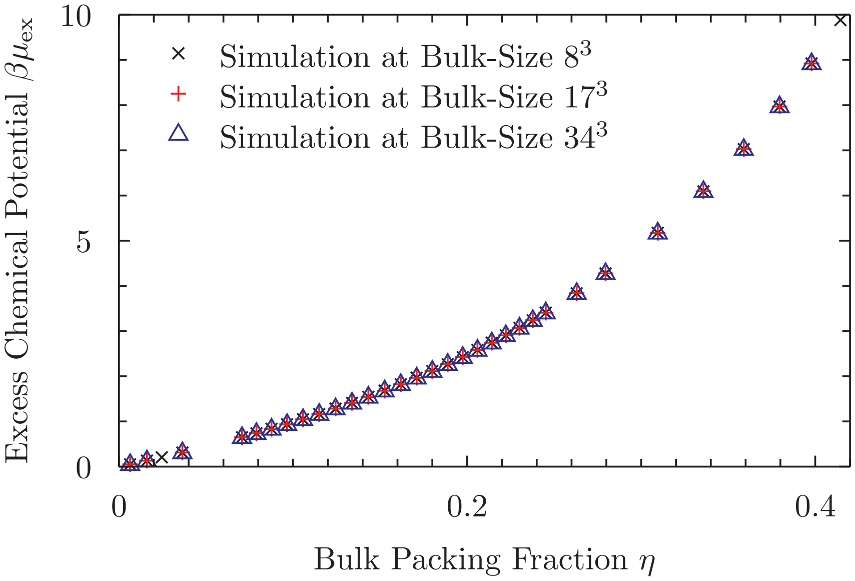

Fig. 4.7: The excess part of the chemical potential potential μ_{ex} (Eq. (2.28)) converges to zero for small packing fractions η of the reservoir for all simulation box sizes, i.e. in the ideal gas limit. Therefore the simulation reproduces the expected thermodynamical behavior.

4.5 Simulation Result

The results for the confined fluid simulation are presented in this section. First, data for rather simple geometries are shown whereas the second subsection is dealing with the minimal surface interfaces from chapter 3. It turns out that the behavior of the confined packing fraction is very complex for all the surfaces and at first it seems hardly possible to make any precise predictions on the thermodynamical properties for any given geometry. One of the typical characteristics for all plots is the decreasing influence of the morphological features for larger simulation box sizes, as the η_0 tends towards its bulk value (see e.g. Fig. 4.8).

4.5.1 Simple Geometries

As a starting point for the presentation of the simulation data very simple geometries were chosen. That means the cubic simulation box contains either a sphere that was placed in the center of the box or a cylindrical pore and either the inner or the outer part was declared as the pore domain. The surface properties are found in table 4.1. As these structures are easily implemented into a GCMC simulation, a lot data could be generated. The simulation data for a sphere of radius $0.3L$ with inside orientation, i.e. the sphere itself is the pore domain, for values of $L = 8, 17, 34$ is presented in Fig. 4.8. For cubic simulation boxes L denotes the edge length of the box in units of the sphere diameter σ, if not otherwise stated. In the case of a tetragonal simulation box the edge lengths in each space direction are given explicitly.

For reasons of convenience η is chosen as parameter on the x-axis rather than the simulation input parameter μ. As theory and simulation data are in good agreement for the bulk case (shown in section 4.4), it is possible to exchange both quantities. The implicit relation Eq. (4.46) is used to determine the bulk packing fraction of the reservoir as function of the chemical potential.

The data show a very complex behavior although the structure is fairly simple. The first observation is that the confined packing fraction η_0 (Eq. (2.23)) is always larger than the corresponding bulk packing fraction η of the reservoir. This can be partly explained by the very nature of the definition of η_0. Although the sphere centers cannot penetrate the excluded pore domain P_{ex}, the sphere domain itself may overlap with this part of the pore. For entropic reasons the probability to find sphere close to the walls is higher as in first order the entropy is linear to the space occupied by the spheres. Spheres adsorbed by the wall occupy less space of the accessible volume and therefore provide more space for other particles. An illustration for the influence of a planar wall on the local density is given in Fig. 7.1. Spheres close to the substrate are also less likely to be pushed away compared to spheres that are fully surrounded by other spheres.

This statement is further sustained by the fact that for increasing box size the effect is decreasing. For larger box sizes the ratio $A[\mathcal{P}]/V[\mathcal{P}]$ is getting smaller. Therefore the ratio of spheres adsorbed at the walls to the total amount of spheres within the simulation box is smaller.

It is also observed that deviations are smaller for lower bulk packing fractions. The influence of the confinement is decreasing as the correlations of the spheres with the walls are smaller for lower densities, i.e. the correlation length ξ is smaller. As a consequence the relative difference between η_0 and η tends to zero for low densities.

The same observations are made for the other sphere structures (Fig. 5.5) and as well as for the cylindrical pores (Fig. 5.6). Although qualitatively equivalent, the relative difference between η_0 and η is smaller for pores with high porosity ϕ. This is also explained by the fact that the ratio $A[\mathcal{P}]/V[\mathcal{P}]$ is smaller for those geometries.

Nevertheless it remains unclear, how to quantitatively describe these deviations. An answer is presented in chapter 5.

4.5.2 Minimal Surfaces

The analysis is now extended to the minimal surfaces introduced in chapter 3. The surface properties are found in table 4.2. As their structure is very complex (Fig. 3.5), one might

Structure	Orientation	Radius	Porosity
Sphere	inside	$0.3L$	0.11
	inside	$0.4L$	0.27
	outside	$0.3L$	0.90
	outside	$0.4L$	0.73
Cylinder	inside	$0.3L$	0.28
	inside	$0.4L$	0.50
	outside	$0.2L$	0.87
	outside	$0.3L$	0.72

Table 4.1: Properties of the used geometries for a box size of L. Inside means that the pore space is the inner part of the sphere/cylinder, outside the opposite.

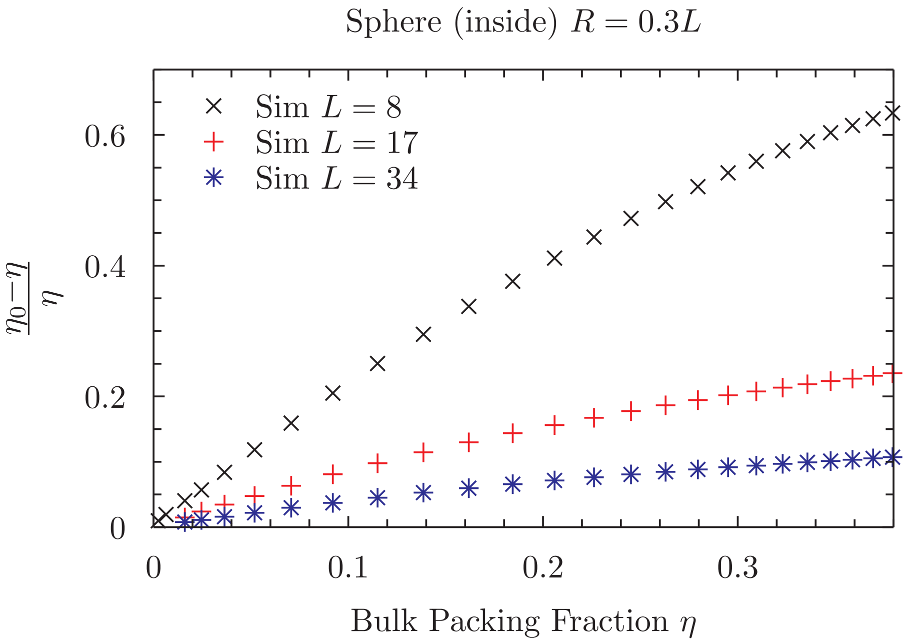

Fig. 4.8: Simulation result for a sphere of radius $0.3L$ placed in the center of a cubic simulation box with edge length L. The inner part of the sphere is defined as the pore space, whereas the outer part represents the substrate. The relative difference between the confined packing fraction η_0 and the reservoir packing fraction η is plotted versus η. There are deviations from the bulk case due to the confining geometry, that decrease with larger box size and smaller packing fraction of the reservoir. This behavior is typical for all solid pore interfaces examined in this work. An explanation for that behavior is given in section 4.5.1.

expect that the behavior of η_0 is also more complex. But it turns out that the behavior is qualitatively similar to the spherical and cylindrical pores discussed in the previous section as illustrated for the Gyroid in Fig. 4.9. Further, in Fig. 4.10 the dependence of η_0 on the geometry is illustrated. For all surfaces the box size was chosen to be $L = 8$.

The deeper meaning of the choice of the box sizes becomes apparent in chapter 5. The simulation data for $L = 17, 34$ for the other TPMS are found in Fig. 5.4.

surface	box size	area	Euler number	Porosity ϕ
Gyroid	L	$3.094 \cdot L^2$	-4	1/2
Primitive (P)	$1.1484 \cdot L$	$3.094 \cdot L^2$	-2	1/2
P8uc	$0.8121 \cdot L$	$3.094 \cdot L^2$	-16	1/2
Diamond (D)	$0.8977 \cdot L$	$3.094 \cdot L^2$	-8	1/2
IWP (I)	$0.9450 \cdot L$	$3.094 \cdot L^2$	-6	0.537
IWP (WP)	$0.9450 \cdot L$	$3.094 \cdot L^2$	-6	0.463
H	xl=$1.564 \cdot L$ yl=$0.903 \cdot L$ zl=$0.726 \cdot L$	$3.094 \cdot L^2$	-4	1/2

Table 4.2: List of the studied solid pore interfaces that are introduced in section 3.1. For all geometries the box size is set up in a way that the surface area equals the surface area of the Gyroid for box size L. As this structure is well understood and a lot of simulation data are available, it is taken as a reference point. The intertwined channel systems of Gyroid, P and D are congruent as mentioned in section 3.1 whereas this is not the case for the IWP surface. Therefore results for both orientations are presented. (I) means, that the I-labyrinth is the pore domain and vice versa. P8uc denotes a primitive surface but with 8 (smallest) cubic unit cells within the simulation box (instead of one). Finally the H structure does not have a cubic but a (non-primitive) tetragonal unit cell, so edge lengths are given in each space direction. The deeper meaning of this choice becomes apparent in chapter 5.

4.5.3 Comparison to DFT Data with Voxelized Interfaces

The validation of our simulation results is supported by the good agreement we find with numerical 3D DFT calculations for TPMS, carried out by Roland Roth [44] (Fig. 4.11). Those were obtained with voxelized data sets of the minimal surfaces used in the Monte Carlo simulation.

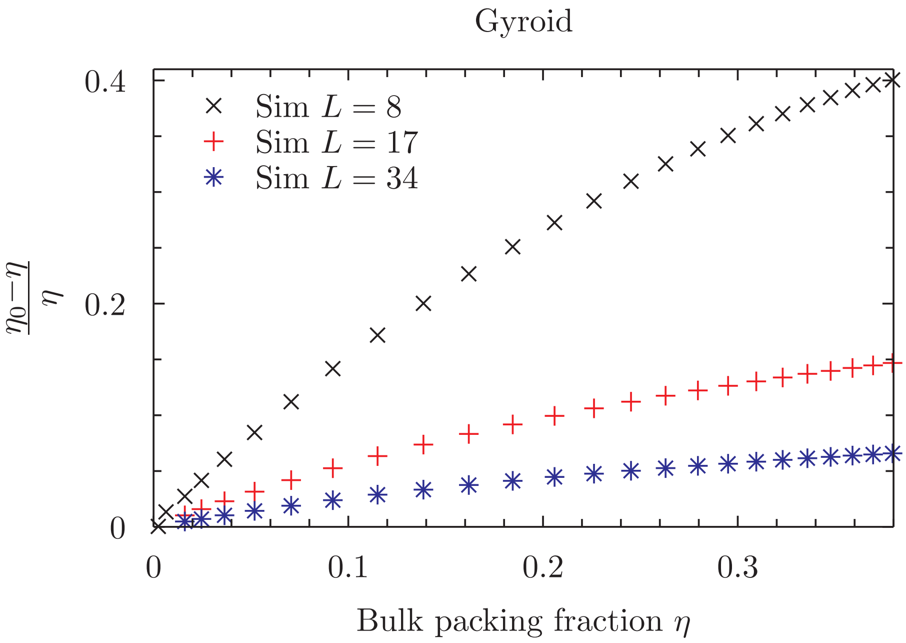

Fig. 4.9: Simulation result for the Gyroid (s. Fig. **??**) for box sizes $L = 8, 17, 34$. Although the geometry of the Gyroid (Fig. 3.1) is more complex than the geometry of a single sphere, the behavior of the relative difference between the confined packing fraction and η is similar (Fig. 4.8). An explanation for the positivity of $(\eta_0 - \eta)/\eta$ is given in section 4.5.1.

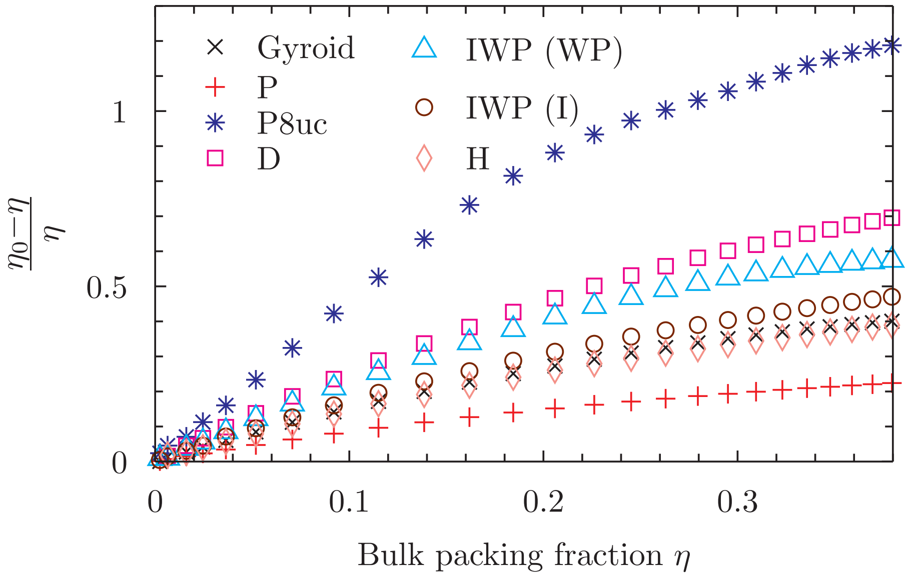

Fig. 4.10: Simulation result for all TPMS of table 4.2 for $L = 8$. The P8uc is showing the largest relative difference $(\eta_0 - \eta)/\eta$ as it has the least pore volume compared to all other TPMS with $L = 8$. As all surfaces have the same surface area the ratio of surface area A to volume V is the largest for the P8uc surface. According to the explanation given in section 4.5.1, this is reason for the large relative difference $(\eta_0 - \eta)/\eta$ of the P8uc structure compared to the other shown TPMS.

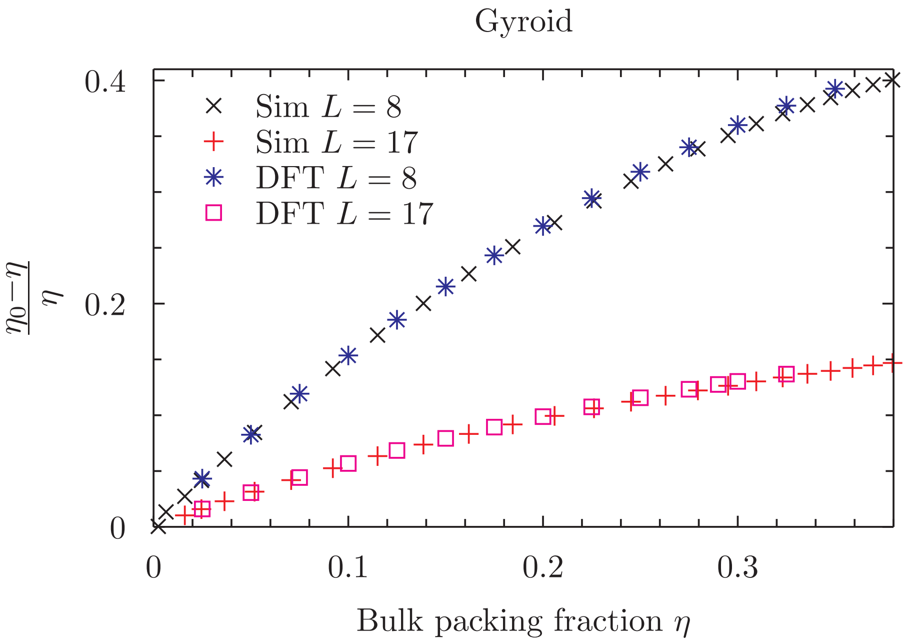

Fig. 4.11: Comparison of simulation result and DFT data for the Gyroid. The data were obtained by 3D DFT calculations, carried out by Roland Roth, using voxelized data sets for the TPMS [44]. The agreement of both approaches is very good. Thus the simulation data can be regarded as being well established within the parameter range of η. For $L = 34$ the DFT calculation are not available.

5 Morphometric Approach for Large Pores

The simulation results show a complex behavior, that needs to be understood. In this chapter a theory is presented that predicts the simulation results quantitatively in a very good manner in the range of our input parameters. In section 5.1 the theoretical background of the morphological approach is discussed, whereas section 5.2 demonstrates the good agreement of theory and simulation data. This is shown for the relative difference $(\eta_0 - \eta)/\eta$ between η_0 and η and the adsorption Γ. Furthermore it is attempted to show the influence of the topology on the thermodynamic properties by extracting the Euler number X of the studied surfaces using only the theoretical concept and the simulation data.

As we have seen in section 3.1, the thermodynamic properties of a confined hard sphere fluid depend on the shape of the pore $\mathcal{P}$. According to a general hypothesis this dependence can be expressed as a linear combination of the volume $V[\mathcal{P}]$, the area $A[\mathcal{P}]$ of the interface, the integrated mean curvature $C[\mathcal{P}]$ and the Euler number $X[\mathcal{P}]$ [33]. In Refs. [30, 31, 32] the structure and phase behavior of microemulsions was explained by assuming that the free energy of the fluid on a mesoscopic scale is given by these four fundamental measures. Furthermore, König *et al.* have shown numerically that these four measures are sufficient to describe accurately the free energy of a hard-sphere fluid in contact with a complexly shaped wall [27]. These results are the basis for the morphological study of the thermodynamic properties of our confined hard sphere fluid. In particular, we are describing the morphometric approach for the grand canonical potential Ω (Eq. (2.15)).

5.1 Morphometric Approach

As already stated in section 2.2, the grand canonical potential $\Omega = \Omega[S; T, \mu]$ of a fluid depends on the temperature T and on the chemical potential μ, as well as on geometry of the confining substrate that bounds the system S. For hard sphere systems, as employed here, the temperature dependence can be omitted (see section 2.3). The remaining question is the identification of the relevant morphological parameters.

The focus is now on the dependence of $\Omega[S]$ on the shape of the confinement of S. The actual form of this mapping from a given pore geometry onto real number is a complex integral over the phase space of the whole system, that usually can be calculated only approximately. Nevertheless, it has been shown in Ref. [28] that only four morphological measures, i.e. the pore volume $V[S]$, the surface area $A[S]$, the integrated mean curvature $C[S]$ and the Euler number $X[S]$ (see section 4.3.3), are sufficient to describe the shape dependency of $\Omega[S]$, if certain physical conditions are satisfied:

(a) Motion invariance: The thermodynamic potential of a system must be independent of its location and orientation in space, i.e. $\Omega[gS] = \Omega[S]$ for all translations and rotations g in three dimensions.

(b) Continuity: If a sequence of convex sets S_n converges towards the convex set S for $n \to \infty$, then $\Omega[S_n] \to \Omega[S]$. This continuity property intuitively expresses the fact that an approximation of our convex domain by, e.g. a triangulated surface, yields an approximation of the grand canonical potential $\Omega[S]$ by $\Omega[S_n]$. It is stated in Ref. [28] that continuity is violated if the pore is very small and comparable in size to that of the fluid particles. In our case the volume of the unit cells of the examined surfaces $V \gg V_{\mathrm{sph}}$ and therefore continuity effects are neglected.

(c) Additivity: The functional of the union of two domains S_i, $i = 1, 2$, is the sum of the functional of the single domains subtracted by the functional of the intersection:

$$\Omega[S_1 \cup S_2] = \Omega[S_1] + \Omega[S_2] - \Omega[S_1 \cap S_2] \tag{5.1}$$

This relation generalizes the common rule for the addition of an extensive quantity for two disjunct domains $S_1 \cap S_2$ to the case of overlapping domains by subtracting the value of the thermodynamic quantity of the double-counted intersection. The intersection does not need to be a volume but can rather be an area or a line for adjacent bodies S_i. Additivity can break down if long ranged interactions are present, which is not the case for hard sphere systems, or if the system develops a macroscopic intrinsic length scale. In the case of a system confined by a minimal surface geometry, this means that the average width of the channel systems is comparable to the correlation length ξ (see section 4.4) of the hard sphere fluid. This shall be further examined in the successive sections.

The basis for this assumption is the Hadwiger theorem [18]. It states that any functional of the shape in three dimensions $f[S]$ that satisfies the conditions (a), (b) and (c) can be written as a linear combination of the Minkowski functionals V, A, C and X. Assuming that the grand canonical potential of the hard sphere system fulfills these conditions, the ansatz

$$\Omega[S;\mu] = -p(\mu) \cdot V[S] + \sigma(\mu) \cdot A[S] + \kappa(\mu) \cdot C[S] + \bar{\kappa}(\mu) \cdot X[S] \tag{5.2}$$

can be regarded as complete expression for $\Omega[S;\mu]$. The pressure p, the surface tension at the planar wall σ and the bending rigidities κ and $\bar{\kappa}$ are properties of the fluid and the wall-fluid interaction but do not dependent on the actual shape of the confining surface.

It is important to realize that Eq. (5.2) can be applied to any complex solid pore interface, e.g. the minimal surfaces introduced in chapter 3, as the geometry enters only via the four quantities V, A, C and X, which can be obtained easily. On the other hand the thermodynamic coefficients p, σ, κ and $\bar{\kappa}$ can be determined for simple geometries. This has been done for planar, spherical and cylindrical walls by means of Rosenfeld's fundamental measure theory (FMT) [42] and the White-Bear version of FMT [21, 43] . Both of them have shown to give an accurate description of the thermodynamics and the structure of the hard sphere fluids exposed to those geometries. For reasons of simplicity, we restrict ourselves to the White-Bear version of FMT mark II in this thesis. According to Ref. [21] the pressure coefficient

$$\beta p = \frac{3\eta}{4\pi R^3} \, \frac{1+\eta+\eta^2-\eta^3}{(1-\eta)^3} \ , \tag{5.3}$$

the planar wall surface tension (at a hard wall)

$$\beta\sigma = \frac{\eta(2+(3-2\eta)\eta)-(1-\eta)^2\ln(1-\eta)}{4(1-\eta)^2\pi R^2}, \tag{5.4}$$

the first bending rigidity

$$\beta\kappa = \frac{(5-\eta)\eta}{(1-\eta)R} + \frac{2}{R}\ln(1-\eta), \tag{5.5}$$

and the second bending rigidity

$$\beta\bar{\kappa} = -\ln(1-\eta) \ . \tag{5.6}$$

The relation (4.46) establishes the dependence of those coefficients on the chemical potential μ. For reasons of convenience the bulk packing fraction η (see Eq. (2.24)) is chosen as main parameter instead of the chemical potential μ from here on.

All thermodynamic quantities of interest here can be derived directly from Ω and inherit the simple dependence on the shape of S by virtue of Eq. (5.2). Applying this to our pore geometries, the confined packing fraction η_0 as defined in Eq. (2.23) can be expressed in terms of the morphological features of the pore $\mathcal{P}$ and the bulk packing fraction η as

$$\begin{aligned}
\eta_0(\mathcal{P},\eta) &= \frac{V_{\text{Sph}}}{V_{\text{acc}}[\mathcal{P}]}\langle N\rangle \overset{(2.16)}{=} -\frac{V_{\text{Sph}}}{V_{\text{acc}}[\mathcal{P}]}\frac{\partial\Omega(\mathcal{P},\mu)}{\partial\mu} \\
&\overset{(5.2)}{=} -\frac{V_{\text{Sph}}}{V_{\text{acc}}[\mathcal{P}]}\left(\frac{\partial(-p)}{\partial\mu}V[\mathcal{P}] + \frac{\partial\sigma}{\partial\mu}A[\mathcal{P}] + \frac{\partial\kappa}{\partial\mu}C[\mathcal{P}] + \frac{\partial\bar{\kappa}}{\partial\mu}X[\mathcal{P}]\right) \ , \\
&= \frac{V_{\text{Sph}}}{V_{\text{acc}}[\mathcal{P}]}\left(\rho_{\text{bulk}}V[\mathcal{P}] + \Gamma_\sigma A[\mathcal{P}] + \Gamma_\kappa C[\mathcal{P}] + \Gamma_{\bar{\kappa}}X[\mathcal{P}]\right) \ . \qquad (5.7)
\end{aligned}$$

where the Gibbs-Duhem relation

$$\left(\frac{\partial\beta p}{\partial\mu}\right)_{V,T} = \rho_{\text{bulk}} \tag{5.8}$$

was used. The derivatives (taken at constant temperature T and constant volume V) are given by:

$$\Gamma_\sigma = -\frac{\partial}{\partial\mu}\sigma = -\frac{\partial\sigma}{\partial\eta}\left(\frac{\partial\mu}{\partial\eta}\right)^{-1} = \frac{(\eta-1)\eta(3+\eta(6+\eta(2\eta-5)))}{4(1+\eta(4+(\eta-2)^2\eta))\pi R^2} \ , \tag{5.9}$$

$$\Gamma_\kappa = -\frac{\partial}{\partial\mu}\kappa = -\frac{\partial\kappa}{\partial\eta}\left(\frac{\partial\mu}{\partial\eta}\right)^{-1} = \frac{(\eta-1)^2\eta(3+\eta^2)}{1+\eta(4+(\eta-2)^2\eta)R} \tag{5.10}$$

$$\Gamma_{\bar{\kappa}} = -\frac{\partial}{\partial\mu}\bar{\kappa} = -\frac{\partial\bar{\kappa}}{\partial\eta}\left(\frac{\partial\mu}{\partial\eta}\right)^{-1} = \frac{(\eta-1)^3\eta}{1+\eta(4+(\eta-2)^2\eta)} \ . \tag{5.11}$$

A visualization of Γ_σ, Γ_κ, $\Gamma_{\bar\kappa}$ is found in Fig. 5.1. The relative difference $(\eta_0 - \eta)/\eta$ can be expanded in powers of η as

$$\frac{\eta_0 - \eta}{\eta} = a\eta + b\eta^2 + \mathcal{O}(\eta^3) \ , \tag{5.12}$$

with constants a and b.

Before we go to the comparison of the theoretical predictions to the simulation data another thermodynamical property is introduced, that can easily be extracted from our simulation data. The excess adsorption is defined as

$$\Gamma(\mu) = \frac{1}{A[\mathcal{P}]} \int_{\mathcal{P}} \mathrm{d}\vec{r}(\rho(\vec{r}) - \rho_{\mathrm{bulk}}) \ , \tag{5.13}$$

with the inhomogeneous density profile $\rho(\vec{r})$ of the pore system. Γ measures the excess (over the bulk) amount of fluid adsorbed at the solid-pore interface per unit area. As the evaluation of the integral in (5.13) yields $\langle N \rangle - \rho_{\mathrm{bulk}} V[\mathcal{P}]$, we can use the sampled value of $\langle N \rangle$ to measure the adsorption. The link to the morphometric approach is given by the Gibbs' adsorption theorem

$$\Gamma = -\left(\frac{\partial \gamma}{\partial \mu}\right)_{T,V} \ , \tag{5.14}$$

where

$$\gamma = \frac{\Omega + pV[\mathcal{P}]}{A[\mathcal{P}]} \tag{5.15}$$

denotes the interfacial tension, which measures the total change in the grand potential per unit area introduced by the wall. In combination with (5.2) and (5.9)-(5.11),

$$\Gamma = \Gamma_\sigma + \Gamma_\kappa \frac{C[\mathcal{P}]}{A[\mathcal{P}]} + \Gamma_{\bar\kappa} \frac{X[\mathcal{P}]}{A[\mathcal{P}]} \ . \tag{5.16}$$

A density profile for hard spheres at a planar wall is shown in Fig. 7.1. It is obvious that $\rho(\vec{r}) = 0$ for $\vec{r} \in \mathrm{P}_{\mathrm{ex}}$ as the sphere centers cannot penetrate the excluded volume due to the hard wall interactions. Therefore the integral over P_{ex} yields $(-V[\mathrm{P}_{\mathrm{ex}}]\rho_{\mathrm{bulk}})$. As a consequence the adsorption is expected to be negative for the studied hard sphere systems.

5.2 Results for Large Pores

The theoretical predictions of the morphometric approach are compared to the simulation data. It turns out that the theory is in good quantitative agreement with the simulation in our prescribed parameter range. Only for the P8uc larger deviations for $L = 8$ are found for medium densities (see Fig. 5.3). This is explained by a violation of the additivity condition that needs to be satisfied by the grand canonical potential (cf. sec. 5.1). A detailed discussion on that is given here and in chapter 6. The minor deviations for the other geometry (Fig. 5.4) are assumed to be of the same nature.

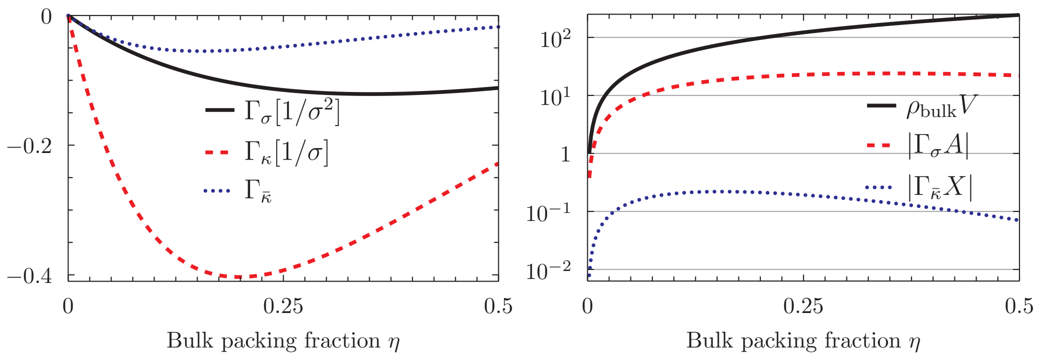

Fig. 5.1: The coefficients Γ_σ, Γ_κ and $\Gamma_{\bar{\kappa}}$ of the morphometric approach for the confined packing fraction η_0 (Eq. (5.7)) on the left hand side. On the right hand side the volume term $\rho_{\mathrm{bulk}}V$, the area term $\Gamma_\sigma A$ and the topological term $\Gamma_{\bar{\kappa}}X$ appearing in the morphometric approach for η_0 (Eq. (5.7)). The volume V, area A and Euler X are chosen to be equal to the geometrical values for Gyroid for a box size $L = 8$. For such a system the contribution of the topological term to the confined packing fraction η_0 is small compared to the volume and area term, as the Euler number is not scaling with the system size. Note the logarithmic scale on the y-axis.

5.2.1 Confined Packing Fraction η_0

The expansion of η_0 in terms of the four geometrical quantities $V[\mathcal{P}]$, $A[\mathcal{P}]$, $C[\mathcal{P}]$ and $X[\mathcal{P}]$ was derived in section 5.1 as

$$\eta_0 = \frac{V_{\mathrm{Sph}}}{V_{\mathrm{acc}}[\mathcal{P}]}\left(\rho_{\mathrm{bulk}}V[\mathcal{P}] + \Gamma_\sigma A[\mathcal{P}] + \Gamma_\kappa C[\mathcal{P}] + \Gamma_{\bar{\kappa}}X[\mathcal{P}]\right) \; . \tag{5.17}$$

This theoretical result is compared to the data obtained via the GCMC simulation. The theoretical prediction and the simulation data are in quantitative agreement for the Gyroid (Fig. 5.2), Primitive (Fig. 5.3) and H interface (Fig. 5.4). Yet the Diamond and IWP structures (Fig. 5.4) show minor and the P8uc larger deviations. One might assume that this discrepancy stems from inherent statistical errors of the simulation. But there are a couple of reasons that are contrary to this assumption. First, there are no deviations for larger box sizes where $L = 17, 34$. A size dependency of the statistical error is not intuitive for a similar number of sampled configurations. Second, the DFT data shows the same behavior. The comparatively small error bars serve as a third argument. In fact, they are omitted because they are smaller than the symbol size.

As a consequence the reason for the deviations must be found within theory which is shortly reviewed here. The first condition set on the grand canonical potential is “Motion Invariance”. As the hard core interactions only depend on the relative positions of the spheres and the substrate, the absolute position in space does not matter. Therefore any rotation or translation of our structure would reproduce the same physical situation. Hence, this requirement is assumed to be fulfilled. Concerning the second condition “continuity”, it has already been stated in section 5.1 that continuity effects are only import for very small systems that are comparable in size with the hard spheres. Knowing the structure of the studied geometries, this condition is also fulfilled.

Thus, the remaining additivity condition has to be examined closely. According to Ref. [28] a fluid can be considered additive inside a concave pore domain, if opposing walls are separated by several correlations lengths. For a hard sphere system at medium densities the correlation length $\xi \approx R$ [45]. Analyzing the medial surface distances for the P8uc structure for $L = 8$, it turns out that certain parts of the channel system are not wider than 3 sphere radii. That means the wall distances are comparable to the correlation length of the fluid for higher densities. Therefore it cannot be assumed that additivity is fulfilled for this structure. This violation explains the observed deviations shown in Fig. 5.3. On the other hand the channels are much wider for Primtive for the studied box sizes. Therefore the additivity condition is assumed to be fulfilled. This is reflected in the quantitative agreement of simulation and theory.

Furthermore, one can use the same argumentation to explain the observed deviations for the other geometries (Fig. 5.4). In chapter 6 the range of applicability of the morphometric approach is studied more closely. Fig. 5.5 and Fig. 5.6 demonstrate that the morphometric approach also works well for structures with integrated mean curvature $C \neq 0$, i.e. for the spherical and cydrincal pore systems .

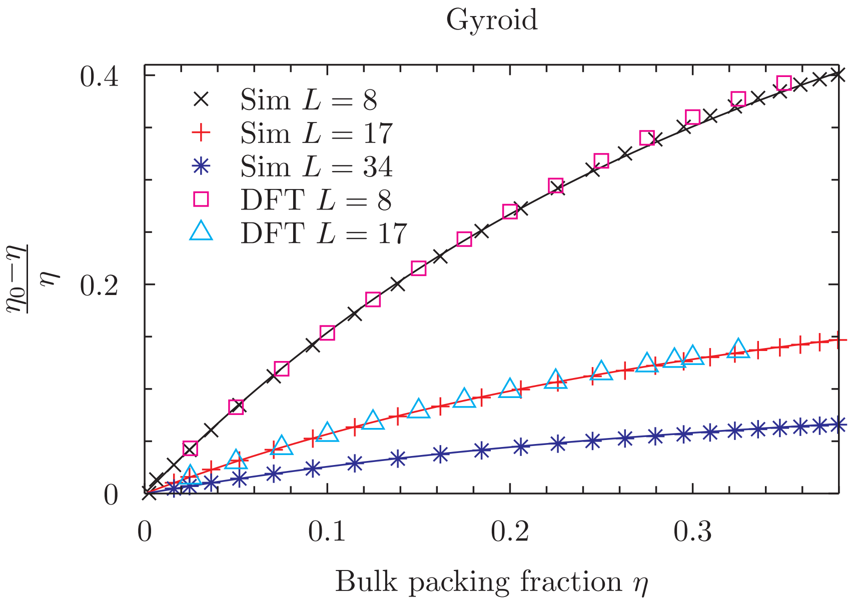

Fig. 5.2: The relative difference $(\eta_0 - \eta)/\eta$ as predicted by the morphometric approach Eq. (5.12) (solid line) compared both to the simulation and DFT data (symbols). The agreement of both numerical approaches to the theoretical curve is really striking. Obviously the morphometric approach is working well within this range of η and L for the Gyroid.

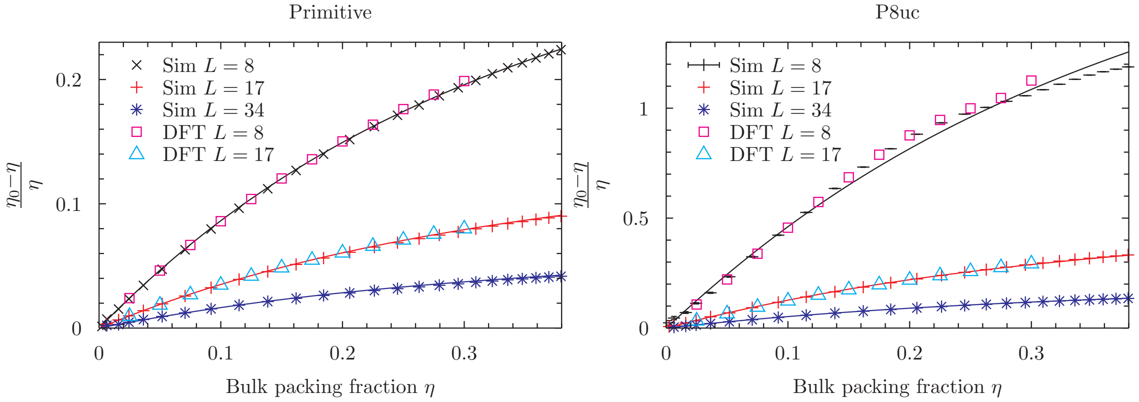

Fig. 5.3: Primitive and P8uc: On the one hand theory and simulation are in very good agreement for the P surface. On the other hand there are deviations for the 8 unit cell equivalent. This can be explained by a violation of the additivity condition set on the grand canonical potential in section 5.1. As the channel system of the P8uc structure is two times narrower than that of the primitive, correlation effects play an important role here. A detailed discussion on that is given in chapter 6.

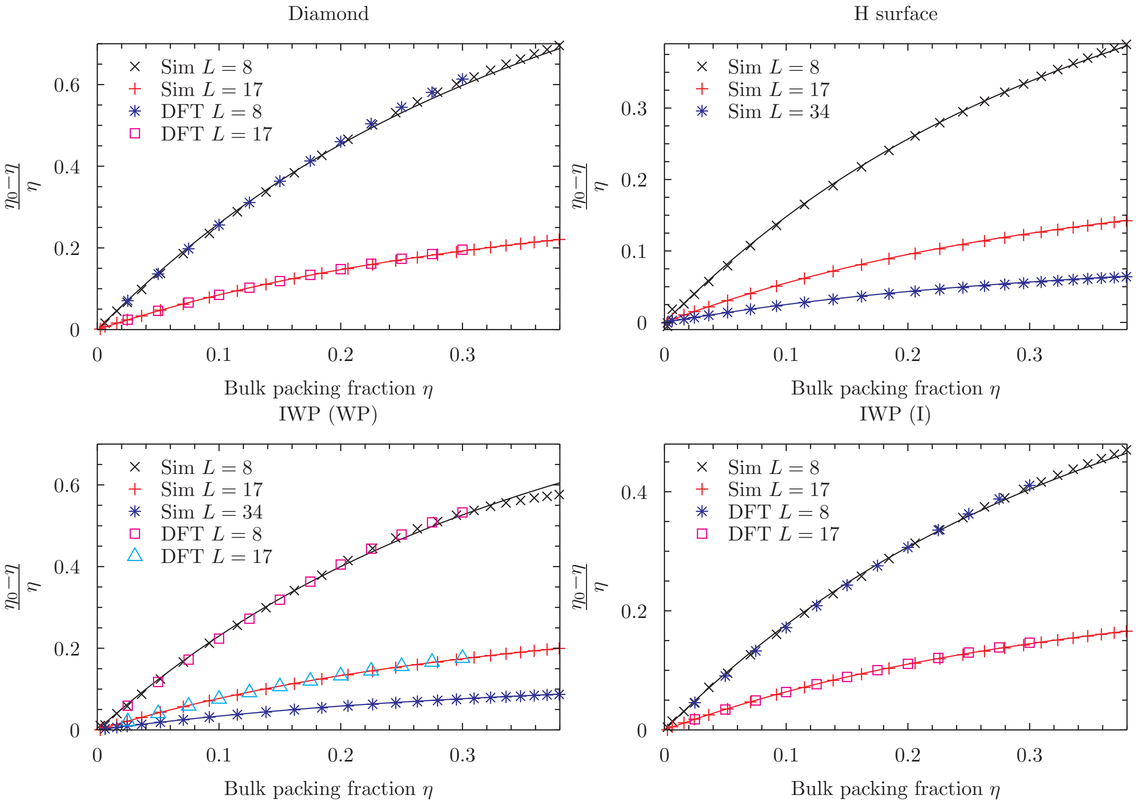

Fig. 5.4: Simulation results for the Diamond, IWP (both orientations) and the H surface and the theoretical predictions. Beside minor deviations for $L = 8$ for bulk packing fractions $\eta \leq 0.25$ the theory is in quantitative agreement with the simulation results.

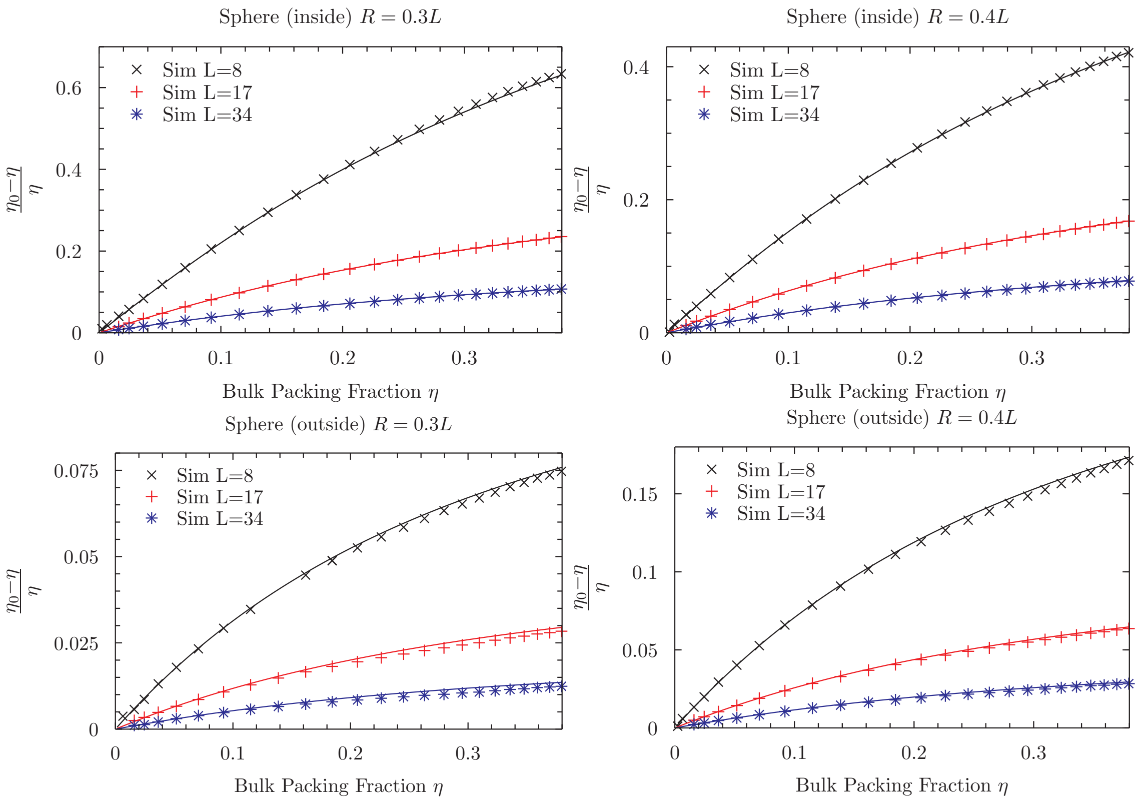

Fig. 5.5: Spherical pores: The good quantitative agreement shows, that the morphometric approach also works for geometries with integrated mean curvature $C \neq 0$.

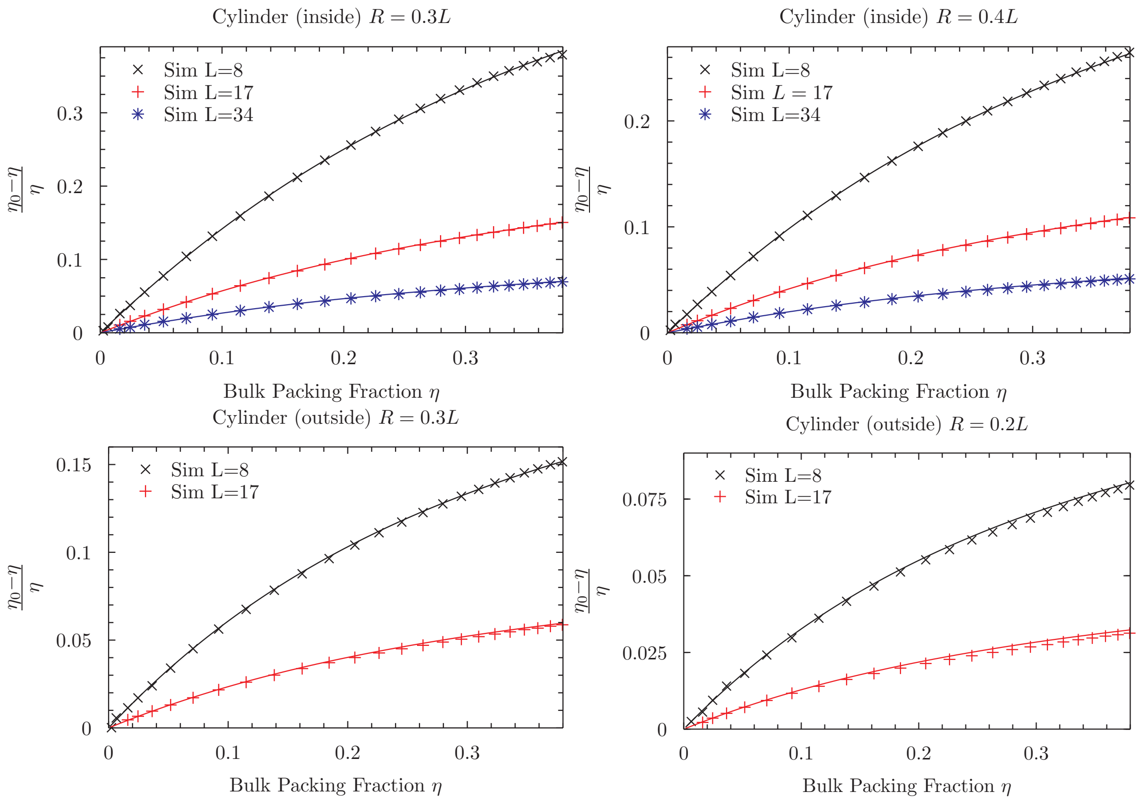

Fig. 5.6: Cylindrical pores: We also observe good agreement with the theoretical predictions.

5.2.2 Adsorption Γ

The dominating contribution to η_0 stems from the volume term $\rho_{\text{bulk}}V$ in Eq. (5.17). Therefore a volume independent quantity is better regarding the understanding of the influence of the other morphometric expressions. As the adsorption Γ exhibits the desired property, it is studied for the given interfaces. Additionally, it can be easily extracted from our simulation data.

The morphometric expression for the adsorption is given by (cf. sec. 5.1)

$$\Gamma(\mathcal{P}, \eta) = \Gamma_\sigma(\eta) + \Gamma_\kappa(\eta)\frac{C[\mathcal{P}]}{A[\mathcal{P}]} + \Gamma_{\bar{\kappa}}(\eta)\frac{X[\mathcal{P}]}{A[\mathcal{P}]} \ . \tag{5.18}$$

The examination of Γ is particularly fruitful for the minimal surface interfaces (table 4.2), as the integrated mean curvature C is 0. This means only the topological term $(X/A)\Gamma_{\bar{\kappa}}$ is expressing the shape dependency of Γ. Furthermore the surface area A of the TPMS was chosen to be equal for all geometries for same corresponding box size L to the Gyroid surface area. It is apparent now, that Γ is solely depending on the ratio X/A and η. In particular differences in the adsorption for different surfaces for the same L should only be due to their different Euler number X.

The results are discussed using the example of P and P8uc (Fig. 5.7). First, as predicted in section 5.1 the adsorption is negative for all systems. Even for the P8uc surface the difference between the theoretical curves for $L = 8$ and $L = 17$ is barely visible, as the term topological term $(\Gamma_{\bar{\kappa}}(\eta)X[\mathcal{P}]/A[\mathcal{P}])$ is small compared to Γ_σ (cf. Fig. 5.1). The simulation and DFT data are in quantitative agreement for the Primitive whereas deviations are observed for the P8uc for packing fractions $\eta \geq 0.15$. This is in accordance with the results obtained for the confined packing fraction η_0, as the same behavior is observed there. Quantitatively there are almost no difference between P and P8uc. The results for the other surfaces are similar, as shown in Fig. 5.8 for the Diamond and H surface.

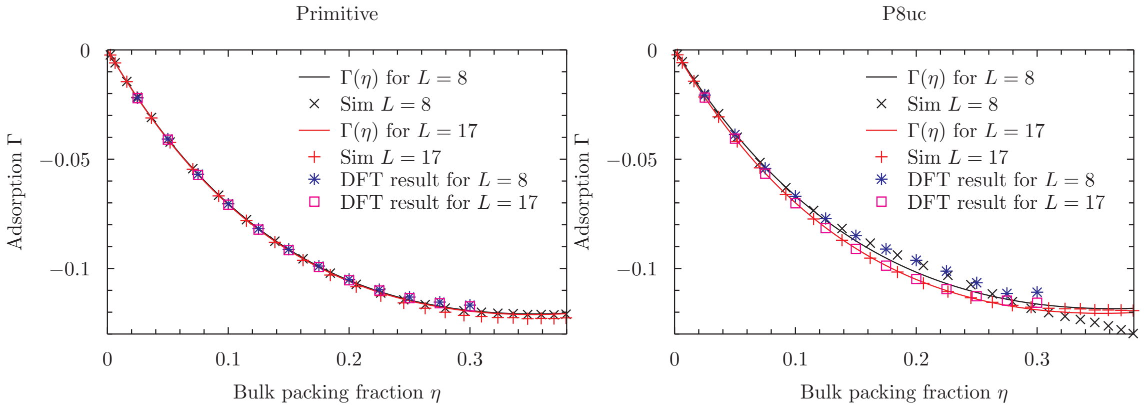

Fig. 5.7: Adsorption plots for Primitive and P8uc. The deviation behavior is similar to the confined packing fraction (s. Fig. 5.3), as the predictions are very accurate for the primitive whereas the numerical results deviate from the theoretical curve for the P8uc for $L = 8$. The almost identical graphs for $L = 8$ and $L = 17$ are due to the fact that $(\Gamma_{\bar{\kappa}}(\eta)X[\mathcal{P}]/A[\mathcal{P}])$ is the only varying parameter which is small compared to $\Gamma_\sigma(\eta)$ (s. Eq. 5.18).

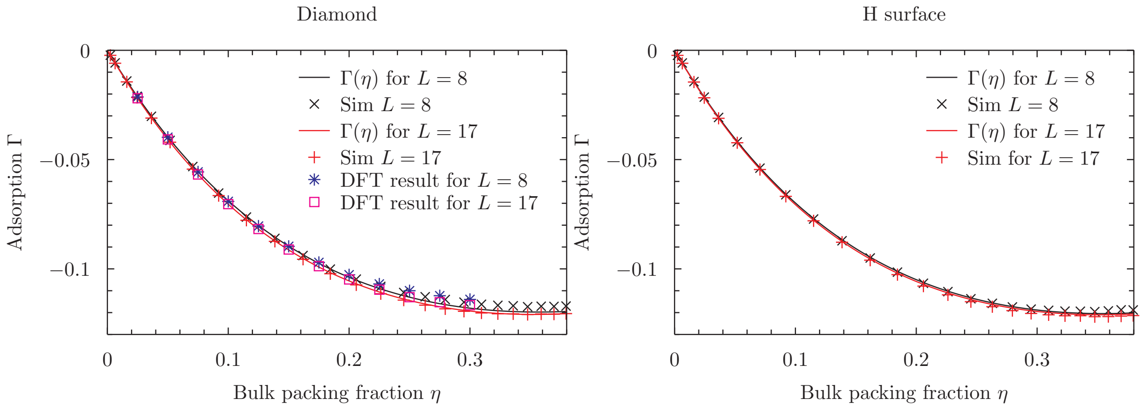

Fig. 5.8: Plots for the other examined structures. The agreement for all of them is still really good, although all geometries except the H surface show stronger deviations with increasing bulk packing fraction for a scaling factor of 8.

5.2.3 Influence of Topology on Simulated Averages

The topological term of the morphometric approach $\Gamma_{\bar{\kappa}} X[\mathcal{P}]$ is studied in this section. Therefore three different attempts are made to extract the Euler number X of our TPMS interfaces using only the theoretical concept, i.e. the morphometric approach and the simulated average of particles.

(1) The morphometric approach for the mean number of particles (5.7) is solved for the Euler number X. The resulting equation is evaluated with the simulation result for the average number of particles for different bulk packing fractions η. The coefficients Γ_σ and $\Gamma_{\bar{\kappa}}$ are taken from Eq. (5.9) and Eq. (5.11).

(2) Similar to attempt (1), but the area coefficient Γ_σ is determined through a simulation of a system confined by two parallel planar walls. Further, the reservoir density ρ_{bulk} is extracted from the bulk simulation discussed in section 4.4 and not calculated through the Carnahan-Starling approximation (Eq. 4.46).

(3) The quantities $\langle N \rangle_{sim}(\eta)$, V, A and X are regarded as fixed parameters for all surfaces and a fitting method is used to obtain $\Gamma_\sigma(\eta)$ and $\Gamma_{\bar{\kappa}}(\eta)$. Then one proceeds as in attempt (1).

A successful extraction further sustains the assumption that thermodynamic properties of fluids are depending on the topology of their confining geometry. It has already been stated that the Euler number X is a constant for each TPMS with integer values (s. tab. 4.2). The evaluation of X should yield a discrete spectra, with plateaus according to the Euler number of the different surfaces. Furthermore it has to be noted that the Euler number is not scaling with the system size. As a consequence the contribution of the topological term is larger for smaller systems. On the other hand it has already been observed, that for small systems the additivity condition required for the morphometric approach might not be fulfilled and the morphometric formula for the grand canonical potential is not valid. Therefore the simulation parameters have to be chosen in way that the grand canonical potential can be regarded additive and the contribution of the topological term is still significant compared to statistical and (unknown) systematic errors. Although certainly not optimized, it has been found out that a simulation box size of $L = 8$ is a suitable choice.

5.2.3.1 Attempt (1)

Using the morphometric coefficients as obtained by density functional theory, the easiest approach is to take the simulated average number of spheres $\langle N \rangle_{sim}$ and subtract all morphometric terms beside the topological. This can be expressed in following equation:

$$X = \frac{1}{\Gamma_{\bar{\kappa}}} \cdot \left(\langle N \rangle_{sim} - \rho_{\text{bulk}} \cdot V - \Gamma_\sigma \cdot A \right) \ , \tag{5.19}$$

where Eq. (5.7) was solved for the Euler number X. As the integrated mean curvature C is vanishing for all TPMS the mean curvature term is omitted.

For a box size of $L = 8$, the best results were obtained, which are shown in Fig. 5.9. Although not very precise, the results qualitatively reproduce the expected behavior for all surfaces expect for the P8uc, which is therefore not shown in the graph. One has to imagine that the absolute values of $\langle N\rangle_{sim}$, $\rho_{\text{bulk}} \cdot V$ and $\Gamma_\sigma \cdot A$ are several orders of magnitude larger than those of $\Gamma_{\bar{\kappa}} \cdot X$ for the chosen box size (cf. Fig. 5.1). Yet the dependence on the topological term is not vanishing, although one might assume that this information is lost in the numerical noise. Nevertheless it has to be pointed out, that only for the presented η range the data agree with the theoretical predictions. For larger η and larger box sizes the results for X show no systematic behavior. This might be explained by the fact that for denser systems, correlation effects are more import and the validity of the morphometric approach might not be given. Further, for larger box sizes the contribution of the topological term is not significant compared to the statistical and systematic errors.

The error bars in Fig. 5.9 are computed for the known statistical error of the simulated average number of spheres $\langle N\rangle$. As the error of all other quantities in Eq. (5.19) is not known, they are assumed to be errorless. But as the statistical errors cannot fully explain the observed deviations, it has to be assumed that the uncertainties of the other quantities are significant. For example, even small errors in the pore volume calculation might affect the obtained results. Additionally the morphometric coefficients are approximations (good though) obtained by means of density functional theory. It is also possible that a non-negligible contribution of the integrated mean curvature C has to be taken into account as the triangulated interfaces are not perfect minimal surfaces. The identification of these sources of error are complicated and have not been studied yet.

5.2.3.2 Attempt (2)

As mentioned in section 5.1 the morphometric coefficients Γ_σ and $\Gamma_{\bar{\kappa}}$ were derived analytically by means of DFT calculations and therefore are only approximations. Thus, it is useful to obtain Γ_σ directly by simulating a fluid between two parallel, planar walls. The morphometric approach for $\langle N\rangle$ reduces then to

$$\langle N\rangle = \rho_{\text{bulk}} \cdot V + \Gamma_\sigma \cdot A \tag{5.20}$$

as C and X are 0 for the given interface. This yields

$$\Gamma_\sigma = \frac{1}{A}\left(\langle N\rangle_{sim} - \rho_{\text{bulk}} \cdot V\right) \ . \tag{5.21}$$

To obtain reliable results the distance d between the parallel walls was chosen to be larger than 15 sphere radii. Therefore additivity is regarded as fulfilled for such a system and the morphometric formula is valid. Further, ρ_{bulk} can also be directly obtained from the bulk simulation data (cf. sec. 4.4). Therefore more information on the quality of our result is available, as only the errors of $\Gamma_{\bar{\kappa}}$, V and A remain unknown. After the calculation of Γ_σ and ρ_{bulk}, one proceeds as in attempt (1).

The result is shown in Fig. 5.10. Compared to attempt (2) slight improvements in the qualitative behavior are observed. In particular the extraction of the Euler number for the P surface is more accurate. As the errors of $\langle N\rangle_{sim}, \rho_{\text{bulk}}$ and Γ_σ are taken into account, the shown error bars are larger for attempt (2). Nevertheless the error approximation is more reliable compared to the previous attempt as the uncertainties of ρ_{bulk} and Γ_σ were unknown there.

Still it is not possible to explain the deviations from the theoretical predictions solely by the statistical errors.

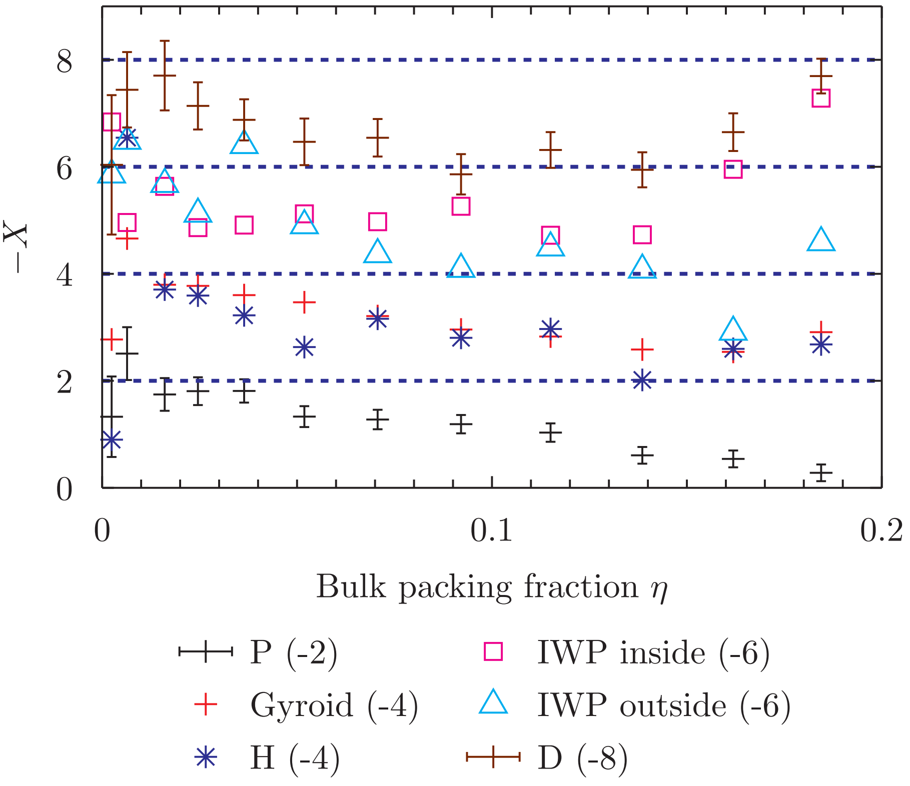

Fig. 5.9: The extraction of the Euler number for attempt (1). Although the quantitative agreement needs to be improved, the correct tendency is reproduced for all geometries. This is an amazing result as the contribution of the topological term to average number of particles is very small compared to the other terms appearing in the morphometric approach (cf. Fig. 5.1). Nevertheless the data is deteriorating outside the presented η-range and does not show the expected behavior. The values behind the surface names are the corresponding Euler numbers. Except for P and D, the error bars are omitted for better visibility. The uncertainties for the other surfaces are comparable in magnitude.

5.2.3.3 Attempt (3)

The final attempt is somewhat different. The quantities $\langle N\rangle_{sim}(\eta)$, V, A and X are regarded as fixed parameters for all surfaces. The scaling factor is restricted to $L = 8$. The coefficients $\Gamma_\sigma(\eta)$ and $\Gamma_{\bar\kappa}(\eta)$ are now obtained for a certain value of η by finding the optimal parameters x_σ and $x_{\bar\kappa}$ for the overdetermined system of equations

$$\begin{aligned} (\langle N\rangle_{sim}(\eta))_1 - \rho_{\text{bulk}} \cdot V_1 \;+ x_\sigma \cdot A_1 +\; x_{\bar\kappa} \cdot X_1 &= 0 \\ \vdots \qquad\qquad\qquad \vdots \qquad\qquad \vdots \quad & \\ (\langle N\rangle_{sim}(\eta))_M - \rho_{\text{bulk}} \cdot V_M + x_\sigma \cdot A_M + x_{\bar\kappa} \cdot X_M &= 0 \end{aligned} \tag{5.22}$$

where the indices $1, \ldots, M$ denote the different minimal surfaces of table 4.2 (except P8uc). This optimization is done by means of a linear least square method, described for example

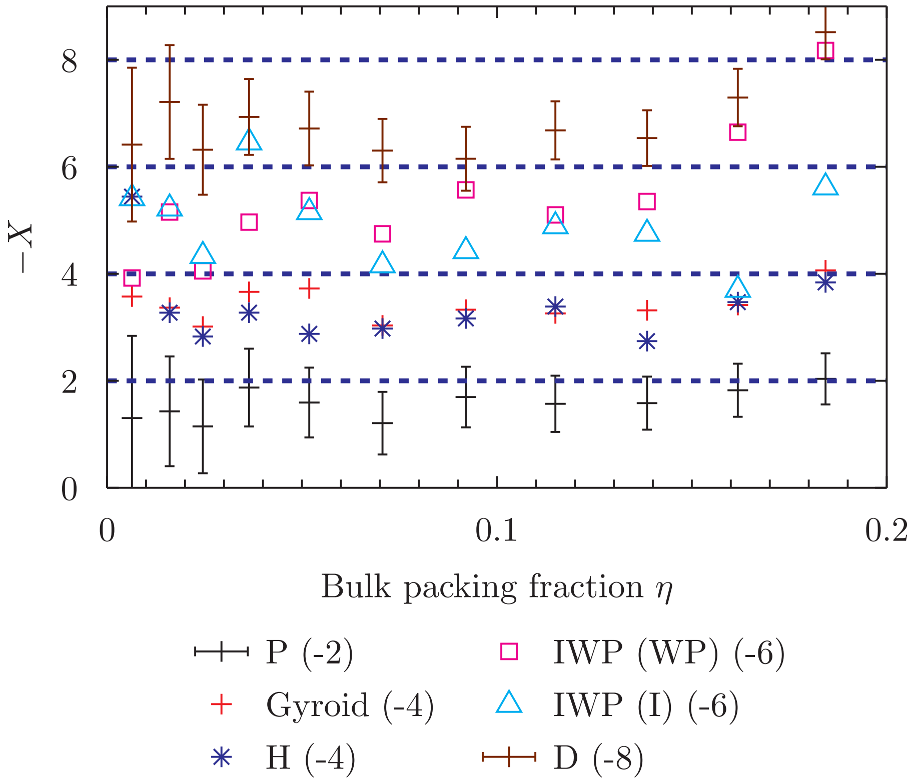

Fig. 5.10: The extraction of the Euler number for attempt (2). Slight improvements compared to the first approach are observed (cf. Fig. 5.9). Especially for the Primitive surface a better agreement is visible. For better visibility, only for the P and the D surface error bars are shown. The uncertainties for all other surfaces are comparable in magnitude. The large error bars compared to attempt (1) are due to the fact, that errors in the area coefficient Γ_σ and in the determination of the bulk packing fraction are taken into account.

in [40] p. 788ff. . The fit parameters x_σ and $x_{\bar{\kappa}}$ then correspond to Γ_σ and $\Gamma_{\bar{\kappa}}$ respectively for each value of η where $\langle N \rangle_{sim}(\eta)$ is available. Eventually one proceeds again as in attempt (1) with the new coefficients.

The quantitative agreement is better for this approach for an even larger η range compared to the previous attempts (Fig. 5.11). This might be explained by the fact that information on the topology of the structures was already used in the fitting routine. In contrast, for attempt (1) and (2) no topological information has been used to determine the Euler number X.

Fig. 5.12 shows $\Gamma_\sigma(\eta)$ and $\Gamma_{\bar{\kappa}}(\eta)$ as obtained by the fitting method. The area coefficient $\Gamma_\sigma(\eta)$ is in good quantitative agreement with the DFT approximation. On the other hand the topological term shows qualitative agreement only for $\eta < 0.15$. Further, the relative error of the fitted $\Gamma_{\bar{\kappa}}$ is larger than 1. This is explained by the fact that the matrix $K = (A_i, X_i)_{i=1,\cdots,M}$ used for the fitting method is badly conditioned, because the area A is equal for all TPMS and two orders of magnitude larger than the Euler number X. The error calculation is also found in [40].

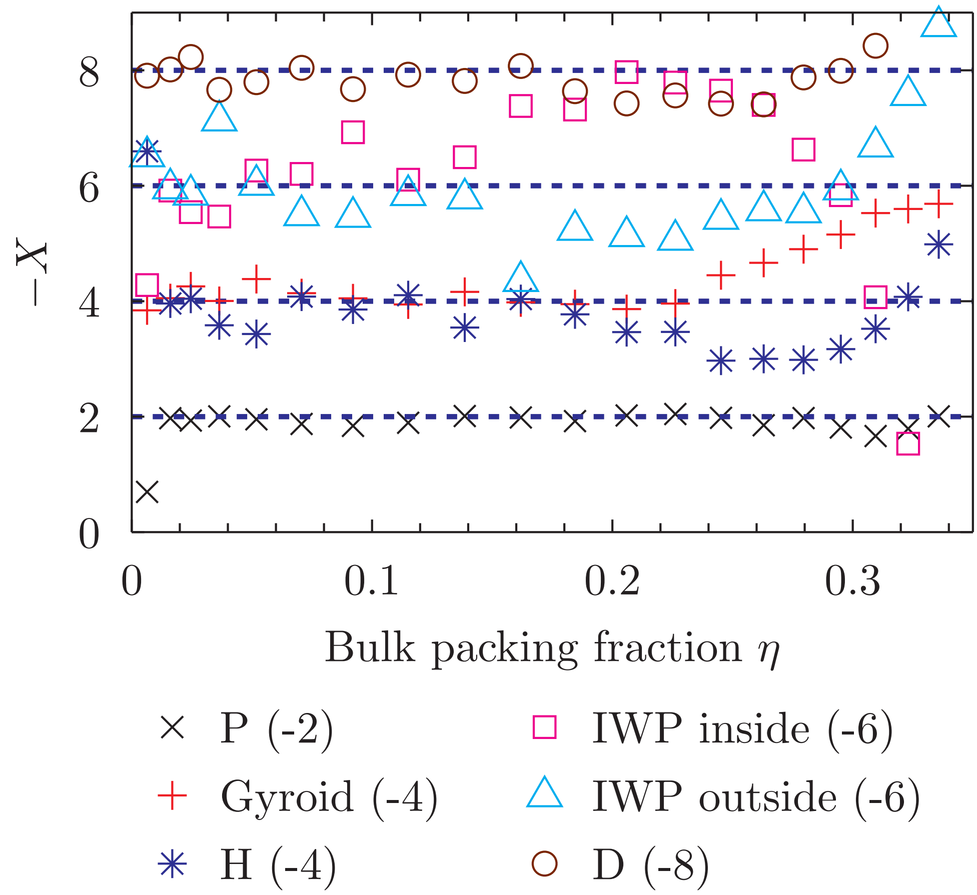

Fig. 5.11: The result for attempt (3). The Euler number X is even better extracted compared to attempt (1) and (2). Also the η-range could be extended up to a value of 0.35.

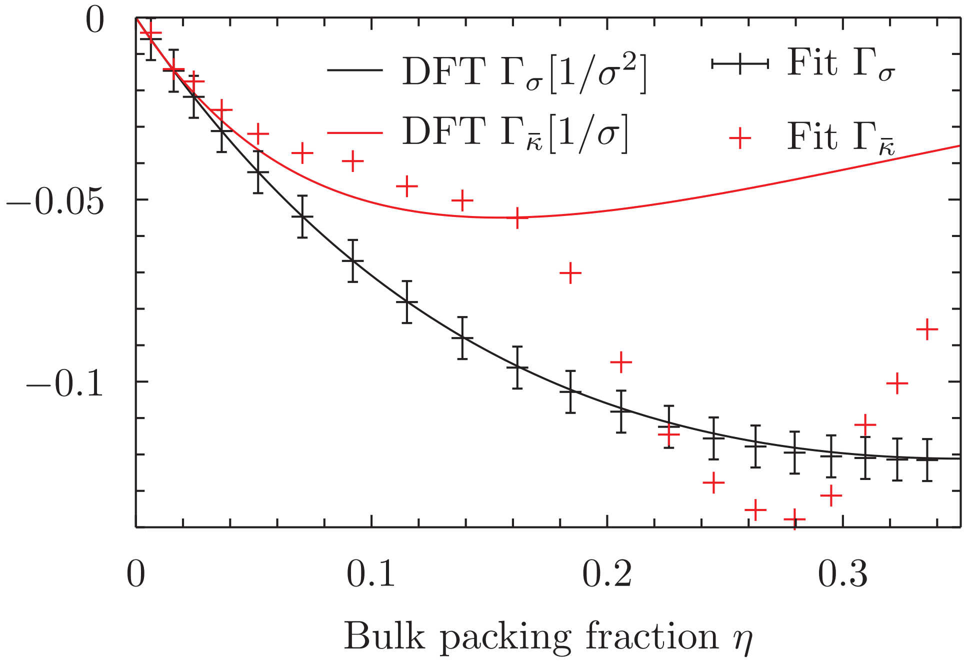

Fig. 5.12: This graph shows both the DFT (see Eq. 5.9) curve and the fitted data for Γ_σ and $\Gamma_{\bar{\kappa}}$. The fitted area coefficient is in good agreement with the theoretical curve whereas the topological term shows no qualitative agreement for $\eta > 0.15$. The error bars for $\Gamma_{\bar{\kappa}}$ are omitted as they are larger than the y-range of the plot.

6 Deviations from the Morphometric Formula

In this chapter the validity range of the morphometric approach is studied. A measure for the average channel width of the TPMS is introduced. It is found out that the morphometric formula for η_0 (Eq. 5.7) is accurate for channel widths larger than two times the correlation length ξ, whereas significant deviations are oberserved for smaller channel widths.

In chapter 5 small deviations from the theoretical predictions have been observed for box sizes $L = 8$. These deviations were explained by the fact that for the given systems the correlation length ξ of the fluid is comparable to the wall distances. Therefore the grand canonical potential cannot be regarded as being additive and the morphometric approach being valid.

The aim is now to examine the correlation between the average channel width of the TPMS in terms of the correlation length $\xi(\eta)$ given by Fig. 6.6 and the deviation of the simulation results for the confined packing fraction η_0 from the morphometric prediction. We define the average channel width as the mean value of

$$d_{\min} = d_m(\mathrm{NP}\,(\mathcal{P})) \tag{6.1}$$

and

$$d_{\max} = d_m(\mathrm{WP}\,(\mathcal{P}))\ . \tag{6.2}$$

$d_m(\mathrm{NP}\,(\mathcal{P}))$ is the medial distance (Eq. (3.5)) of the narrowest point of the pore $\mathrm{NP}\,(\mathcal{P})$ (Eq. (3.7)) and $d_m(\mathrm{WP}\,(\mathcal{P}))$ is the medial distance of the widest point of the pore $\mathrm{WP}\,(\mathcal{P})$ (Eq. (3.8)). The deviation between the morphometric approach and simulation result is expressed by

$$\Delta\eta_0 = \eta_0^{\mathrm{Sim}} - \eta_0^{\mathrm{morph}}, \tag{6.3}$$

where η_0^{Sim} is the simulated average and η_0^{morph} the morphometric prediction. Simulations were run for all TPMS (except P8uc) for varying box sizes of $L = 5, 6, 7, 8, 9, 10$. For a given box size L the correlation length ξ is the varying parameter. The dependence of ξ on the bulk packing fraction η is shown in Fig. 6.6.

The results obtained for the Gyroid (Fig. 6.1), Diamond (Fig. 6.2), IWP (WP) (Fig. 6.3), IWP (I) (Fig. 6.4) and the H surface (Fig. 6.5) show a common characteristic feature. The deviations start to become significant when the average channel width is smaller than two times the correlation length. Especially for the Gyroid surface this effect is apparent. The error bars are omitted for all surfaces but the H surface as they are smaller than the symbol size. Therefore the deviations are not due to statistical uncertainties. As a consequence it might be assumed that for an average channel width larger than 2ξ the additivity condition is fulfilled by the grand canonical potential and the morphometric approach is valid.

Furthermore, some sort of oscillation effect is observed for all surfaces beside the H surface. Using the example of the Gyroid it can be observed that for $L = 5$ and $L = 7$ the difference $\Delta\eta$ is positive for small channel widths, whereas the theory overestimates the confined density for $L = 6$. An explanation might be that certain channel widths are more favorable for sphere packing. The examination of this packing property is difficult for the complex geometries and beyond the scope of this thesis.

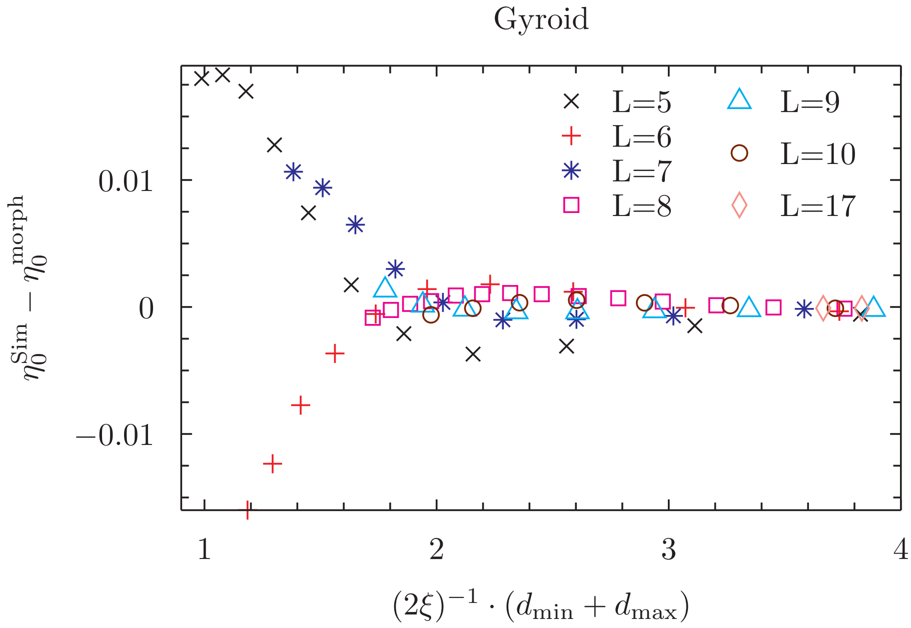

Fig. 6.1: The average channel width $(d_{\min} - d_{\max})/2$ in terms of the correlation length ξ is plotted against the difference $\eta_0^{\mathrm{Sim}} - \eta_0^{\mathrm{morph}}$ between the simulation results and the morphmetric prediction for η_0. For systems where the average channel width is smaller than two times the correlation length $\xi(\eta)$ (Fig. 6.6), significant deviations between theory and simulation are observed. For larger channel widths the morphmetric approach predicts the simulation results very accurately. The error bars are not shown as they are smaller than the symbol size.

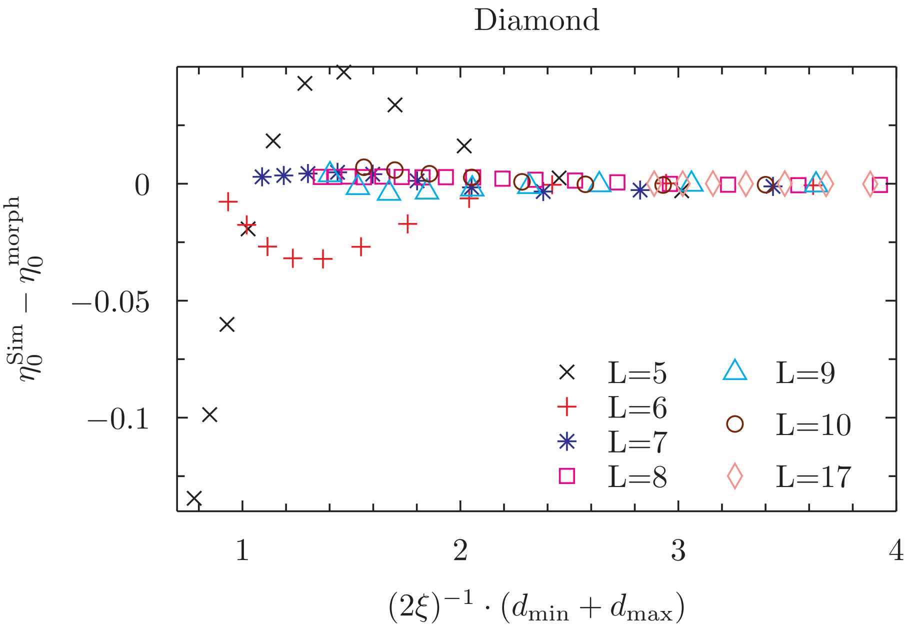

Fig. 6.2: The Diamond surface shows a similar behavior as the Gyroid for $L = 5, 6$. On the other hand for $L \geq 7$ the theoretical prediction are accurate even for systems where the average channel width is smaller than two times the correlation length.

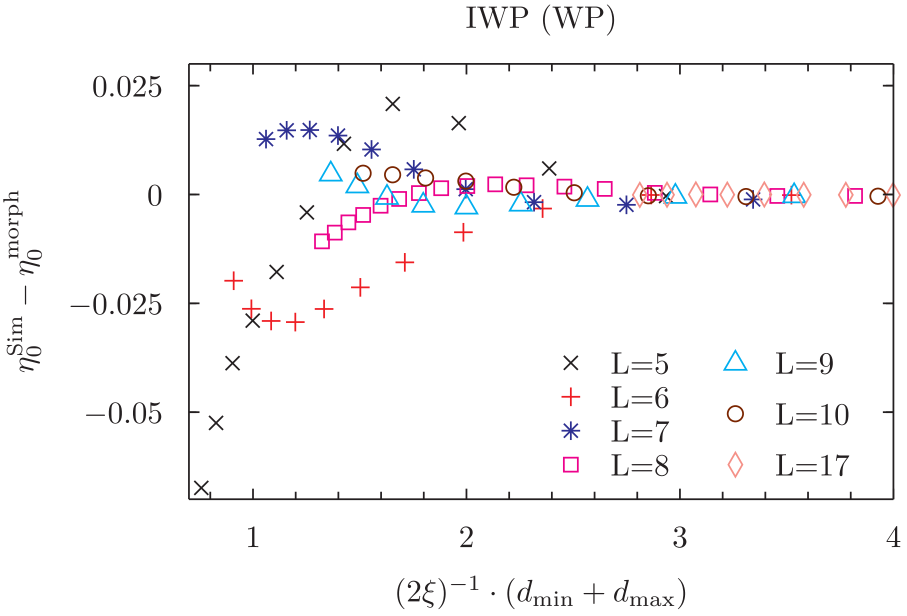

Fig. 6.3: The behavior of the IWP (WP) is similar to that of the Diamond surface. For box sizes $L \geq 7$ small deviations are observed for narrow channels.

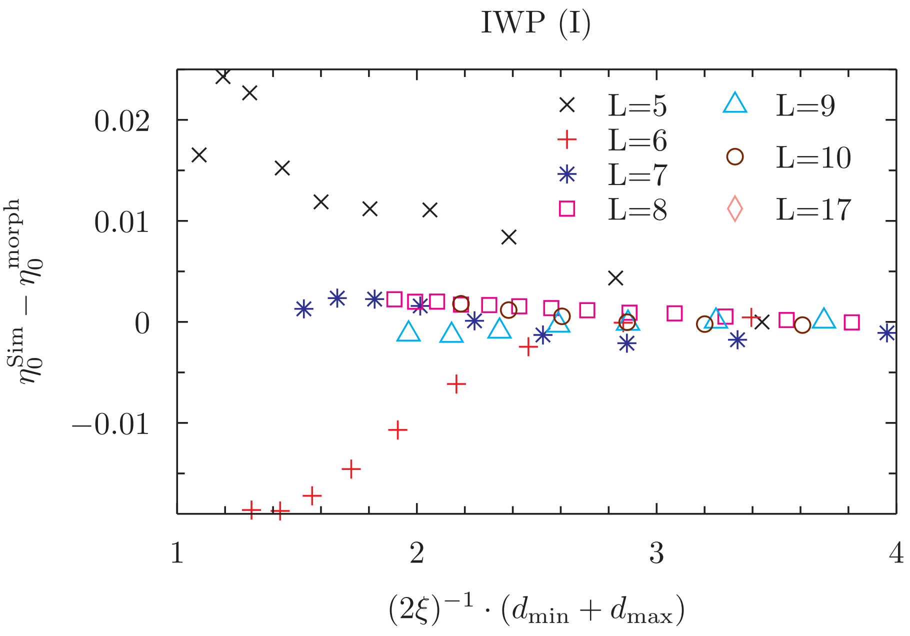

Fig. 6.4: Deviations for the IWP (I) surface. Only for $L = 5, 6$ significant deviations are observed.

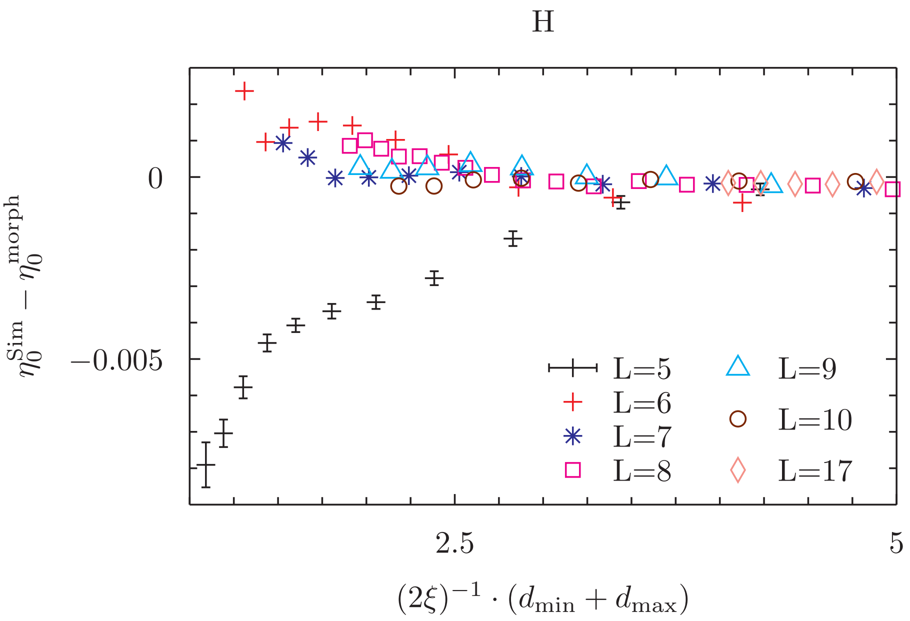

Fig. 6.5: Almost no deviations are found for the H surface, exept for $L = 5$. Obviously the morphometric formula is very accurate for this structure.

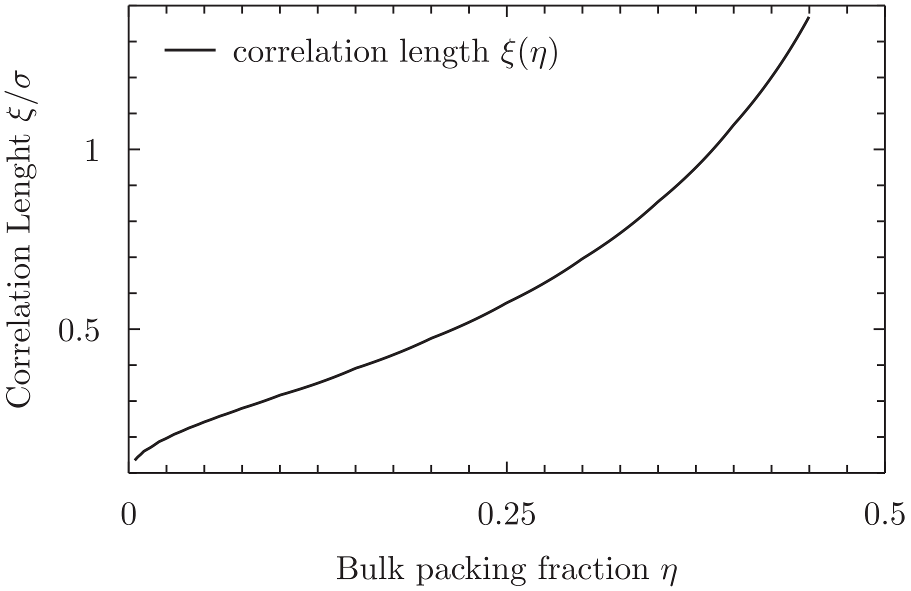

Fig. 6.6: The correlation length $\xi(\eta)$ as a function of the bulk packing fraction. The data is taken from Ref. [45], where it was obtained by means of density functional theory.

7 Development of the Monte Carlo Algorithm

In this chapter certain problems are addressed that occurred during the development of the Monte Carlo program. In particular an alternative input parameter μ^* for the chemical potential is described that led to confusion in context of the proper definition of the excess part of the chemical potential. However, it is shown in section 7.1 that a simulation with μ^* is totally equivalent to one with μ as input parameter. Further, a mistake in the Monte Carlo implementation is described, that led to an incorrect behavior of the excess chemical potential for an ideal gas simulation at low densities. It is shown, that the detailed balance condition was violated in this version of the code. Section 7.3 is dealing with the reliability of the used random number generator. In the final section, we show, that finite size effects are of minor importance in our simulation.

7.1 Simulation Results with μ^* as Input Parameter

In a previous version of the GCMC program the chemical potential μ entered the simulation in slightly different version, namely as the star chemical potential μ^*, which was originally proposed by Adams [2] for a bulk system. Although this did not seem to be important at first, it had far reaching consequences regarding the comparison between the morphometric approach and the simulation results, as we were not able to bring both in line. The question was raised how to properly define the excess part of the chemical potential. This issue is resolved in this section.

The definition of μ^* is given by

$$\beta\mu = \beta\mu^*_{\text{ex}} + \beta\mu^*_{\text{id}} = \beta\mu^* - \ln\langle N\rangle + \ln\left(\Lambda^3 \frac{\langle N\rangle}{V}\right) , \tag{7.1}$$

where

$$\beta\mu^* = \beta\mu^*_{\text{ex}} + \ln\langle N\rangle \ . \tag{7.2}$$

Therefore the star chemical potential

$$\beta\mu^* = \beta\mu - \ln\left(\frac{\Lambda^3}{V}\right) \tag{7.3}$$

is equivalent to the chemical potential $\beta\mu$ except for a constant shift of $\ln(\Lambda^3/V)$, where V denotes the system volume, i.e. the volume of the simulation box. It has to be remarked that the definition of μ^*_{ex} and μ^*_{id} is not generally equivalent to the definition of μ_{ex} and μ_{id} given in Eq. (2.28). It turns out, that this is only true for a bulk fluid.

The simulation was run for a certain value of μ^* with insertion and deletion probability according to (4.23) and (4.24) as:

$$\mathrm{acc}(N \to N+1) = \min\left(1,\ \frac{1}{N+1} \cdot \exp\left(\beta\mu^*\right)\right) \tag{7.4}$$

$$\mathrm{acc}(N \to N-1) = \min\left(1,\ N \cdot \exp\left(-\beta\mu^*\right)\right)\ . \tag{7.5}$$

The star chemical excess potential μ^*_{ex} was then calculated with the simulated average number of particles as parameter $\langle N \rangle$. Though μ^*_{ex} is totally equivalent to μ_{ex} for the bulk case, it is not in the case of a confining geometry. The reason for this problem is the proper identification of the ideal gas part of the chemical potential, or equivalently, the determination of the corresponding (bulk) density ρ_{bulk} of the particle reservoir regarding the definition given in Eq. (2.25).

For better understanding, the following notion might be useful. In a confined system at equilibrium the density distribution $\rho(\vec{r})$ is an inhomogeneous function, as illustrated in Fig. 7.1 for the case of a planar wall in 3D. The integration of $\rho(\vec{r})$ over the whole system volume V yields the average number of particles within the system

$$\langle N \rangle = \int_V \mathrm{d}\vec{r}\ \rho(\vec{r})\ . \tag{7.6}$$

This implies that the expression $\langle N \rangle / V$ exhibits the mean density over the system volume V. It is obvious that this expression cannot be identified with the bulk density of the particle reservoir. On the other hand it is exactly $\langle N \rangle$ that is sampled by the Monte Carlo algorithm. Therefore the star chemical excess potential μ^*_{ex} is not equivalent to μ_{ex} as defined in (2.28).

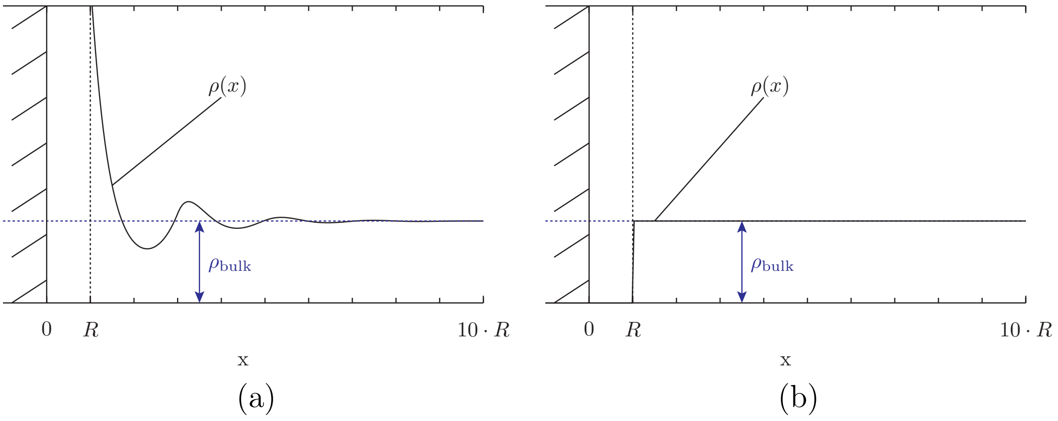

(a) (b)

Fig. 7.1: Density profiles in perpendicular direction to a 3D planar wall for a hard sphere system (a) and an ideal gas system (b). The local density is zero for a distance smaller than the sphere radius R for both cases. For values larger than R the density of the hard sphere system oscillates in a rather complex manner towards the bulk value ρ_{bulk} whereas $\rho(x) = \rho_{\mathrm{bulk}}$ for the ideal gas system. Therefore the bulk density can be reproduced for case (b) by identifying $\rho_{\mathrm{bulk}} = \langle N \rangle / V_{\mathrm{acc}}$ (see Eq. (7.6)). In contrast this not possible for case (a).

Consequently it was not possible to bring the simulation results in line with the theoretical predictions, as we tried to compare the simulation data for a given value c for μ^*_{ex} to the theoretical predictions for the same value c for the excess potential μ_{ex}. The proper way is to calculate the chemical potential μ by Eq. (7.1) and then use Eq. (2.28) to determine μ_{ex}. Therefore

$$\beta\mu_{\text{ex}} = \beta\mu^* - \ln\left(\rho_{\text{bulk}} V\right) . \tag{7.7}$$

Furthermore the notion of μ^*_{ex} as an excess (over the ideal gas) potential is not sensible as it is not converging to zero for in the ideal gas limit. This became apparent for the simulation of a confined ideal gas. In this case confined ideal gas means, that there is no sphere-sphere interaction whereas the hard repulsion of the solid is maintained. It was found, that the value of μ^*_{ex} (see Fig. 7.2) was approximately $\ln\left(V/V_{\text{acc}}\right)$ for all values of μ^*. This can be understood by the following arguments. For an ideal gas the local density is at the constant value of ρ_{bulk} within the accessible volume and zero everywhere else. This implies $\langle N\rangle/V_{\text{acc}} = \rho_{\text{bulk}}$. An illustration is given in Fig. 7.1 for the case of a planar wall in 3D. Further, using the fact that $\mu_{\text{ex}} = 0$ for an ideal gas and Eq. (7.7) one obtains exactly the observed value in the simulation. This also means, that by defining

$$\beta\mu^*_{\text{ex}} = \beta\mu^* - \ln\langle N\rangle - \ln\left(\frac{V}{V_{\text{acc}}}\right) \tag{7.8}$$

the star chemical excess potential behaves well in the ideal gas limit.

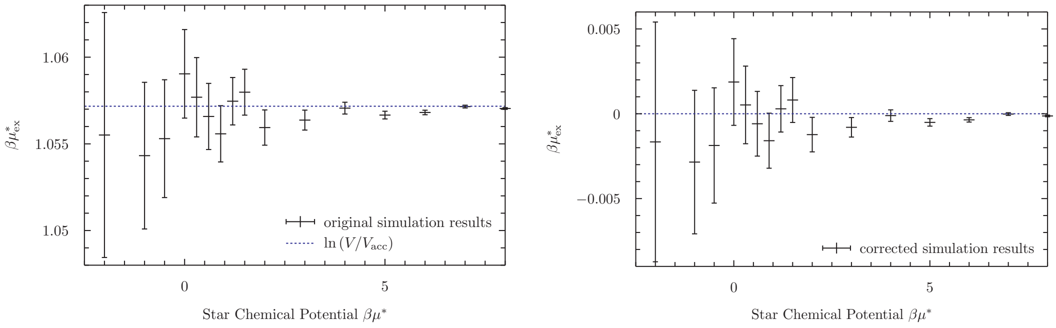

(a) (b)

Fig. 7.2: Confined ideal gas simulation results for the gyroid with simulation box size $L = 10$ (a) for the original definition of μ^*_{ex} (Eq. (7.2)) and (b) for definition (7.8). By subtracting $\ln\left(V/V_{\text{acc}}\right)$ in Eq. (7.2) the star excess chemical potential μ^*_{ex} is zero for all values of μ^* as is necessary for an ideal gas. The amount of sampled configurations is almost equal for all data points, therefore the error of μ^*_{ex} is larger for lower densities.

To conclude, a simulation with the star chemical potential μ^* as input parameter is totally equivalent to a simulation with μ. The advantage that the thermal wavelength Λ does not have to be defined for the determination of the insertion and deletion probabilities is outweighed by the fact, that the equilibrium properties do not depend on the choice of Λ anyway. Finally a simulation result for the Gyroid with μ^* as input parameter and its theoretical prediction is presented in fig. 7.3.

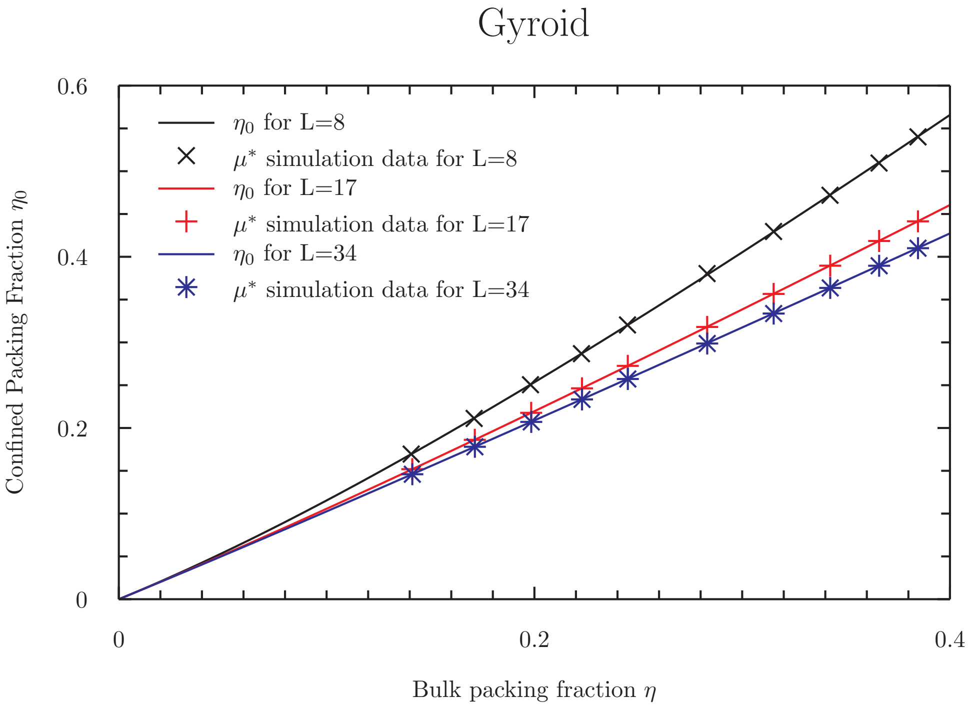

Fig. 7.3: Simulation results for the Gyroid structure with μ^* as input parameter. The results are qualitatively equivalent to the simulation results obtained with μ as input parameter (cf. Fig. 5.2). The agreement with the theoretical prediction is also apparent.

7.2 Mistake in the Monte Carlo Implementation

This section addresses a mistake in the implementation of the Monte Carlo algorithm in a former version of the program, that lead to wrong results for systems with significant probability for the zero particle state. In bulk ideal gas simulations see sec. 7.1, it was observed, that for certain values of the star chemical potential μ^* (defined in Eq. (7.1)) the star excess chemical potential μ^*_{ex} (Eq. (4.47)) was not showing the expected behavior, i.e. $\mu^*_{\text{ex}} = 0$ for all values of μ^* (see Fig. 7.4). For decreasing values of μ^* the effect got even more significant.

As $\mu^*_{\text{ex}} = \mu_{\text{ex}}$ in the case of a bulk simulation, as seen in section 7.1, the mistake was not due to the wrong identification of the excess part of the chemical potential. It turned out, that the algorithm of a single Monte Carlo move, i.e. one attempt to either move, insert or delete a particle, was not constructed the proper way. The problem was, that for a state of zero particles within the simulation box only insertion or deletion was attempted, whereas the probability for a particle displacement for a non-empty box was 1/3. This led to a violation of the detailed balance condition for the $N = 0$ case, as one can easily verify. The detailed balance condition (4.17) for a $N = 0$ state is given by

$$\text{acc}(0 \to 1) \cdot \alpha(0 \to 1) \cdot P(0) = \text{acc}(1 \to 0) \cdot \alpha(1 \to 0) \cdot P(1) \ , \tag{7.9}$$

where “0” denotes the zero particle and “1” an arbitrary one particle configuration. By using the equations

$$\frac{P(1)}{P(0)} = z \quad , \quad \alpha(0 \to 1) = \frac{1}{2} \cdot \frac{1}{V} \ , \tag{7.10}$$

(4.22), (4.25) and (4.26) the detailed balance condition reads:

$$\frac{\text{acc}(0 \to 1)}{\text{acc}(1 \to 0)} \cdot \frac{P(0)}{P(1)} \cdot \alpha(0 \to 1) = \frac{1}{2} = \frac{1}{c} \ . \tag{7.11}$$

This is obviously a contradiction as $1/c = 1/3$ (see subsection 4.3.1) for our simulation program. Therefore the essential detailed balance condition was not fulfilled, i.e. the Boltzmann distribution is not sampled the proper way. The 1/2 in Eq. (7.10) accounts for the fact that only insertion and deletion are attempted for an empty box for the incorrect algorithm. It obvious that the incorrect implementation led to a preferred insertion of particles for systems with significant probability for the $N = 0$ state and therefore caused the unexpected behavior of μ_{ex} as seen in Fig. 7.4.

It shall be remarked, that this mistake affected the simulation of hard spheres as well, but was not observed, as the μ_{ex} behavior is more complex for such a system in general. Therefore an ideal gas simulation is a suitable choice for a check-up of the implementation of the Monte Carlo algorithm.

7.3 Random Number Generator

The name “Monte Carlo” stems from the fact, that a lot of random numbers have to be generated for the simulation. In particular, it is important that the random number generator (RNG) does indeed generate random numbers q uniformly $[0, 1]$ for the check-up of the acceptance probabilities of the Monte Carlo moves. Therefore two different RNG

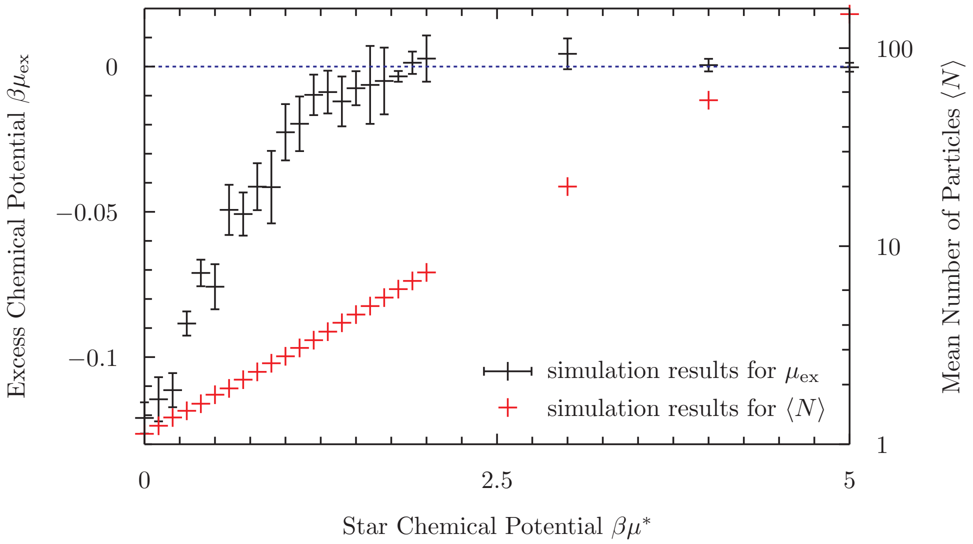

Fig. 7.4: Bulk simulation of an ideal gas in a simulation box of size 10^3. The wrong behavior of μ_{ex} for low μ^* values is due to a mistake in the Monte Carlo algorithm. For systems with significant probability for number of particles $N = 0$, the insertion of particles was preferred what led to a violation of the detailed balance condition (4.17).

were implemented in the program, namely the "minstd_rand" and the "mt19937", both originating from the boost `C++` library [4] to test the reliability of the random number generation. A good discussion on random number generators in general is found in [40].

For the actual test, several simulations were run with the same input parameters for both random number generators. It has been found out, that both RNG lead to the same results aside from statistical uncertainties. As the "minstd_rand"-RNG proved to be a little faster in context of the general simulation time, the results presented in this thesis were obtained using this RNG.

7.4 Finite Size Effects

It has been asserted that finite size effects are small by simulating in $2 \times 2 \times 2$ translational units of the Gyroid surface but with the same translational lattice vector, i.e. in systems with the same domain size or length scale but 2^3 times the volume. As consequence, it is sensible to assume that a simulation with periodic boundary conditions in a single translational unit cell is a good approximation of the thermodynamic limit. Note that in our case, the thermodynamic limit does not mean an infinite enlargement of the translational unit cell but an infinite periodic extension of the triply-periodic minimal surface in each space direction.

8 Summary and Outlook

Summary A short summary of the obtained results is given here. Based on (and due to) the work of Gerd Schröder-Turk *et al.* [13], we are able to successfully perform grand canonical Monte Carlo simulations of hard spheres in complex periodic pore domains bound by so-called triply periodic minimal surfaces. The validation of our simulation results is supported by the good agreement we find with numerical 3D DFT calculations for the same structures, carried out by Roland Roth [44].

Further, we are able to show that in a wide range of input parameters and for several TPMS our simulation results are predicted accurately by a morphometric approach (cf. Fig. 4.9), originally proposed by Klaus Mecke in Ref. [33]. Therefore it is demonstrated that the morphometric formula can be applied to an even wider class of pore domains, as before, the validity has only been tested for domains that were the complement of a convex body [28]. Nevertheless, we also find deviations (cf. Fig. 5.3) , that are explained by a violation of the additivity condition that needs to be satisfied by the grand canonical potential Ω. In particular, it is demonstrated that these deviations are related to the ratio between the average channel width (cf. Eqs. (6.1),(6.2)) and the correlation length ξ. For the studied structures, significant deviations from the morphometric formula are only found for systems with an average channel width smaller than two times the correlation length. Note, that the correlation length is depending on the bulk packing fraction η as shown in Fig. 6.6.

As a remarkable result, we are able to extract the Euler number X of our studied TPMS, using only the theoretical concept and the simulated average number of particles. However, these results are not very accurate and an improvement of the data is certainly needed for an even stronger verification of the notion that thermodynamic properties depend on the topology of the confining structure.

Finally, certain problems that occurred during the thesis project are resolved. It is shown that a simulation with the chemical star potential μ^* as input parameter is equivalent to a simulation with the chemical potential μ as input parameter. Further, it is demonstrated that a mistake in the implementation of the Monte Carlo algorithm led to a violation of the detailed balance condition (4.17) and therefore the simulation produced incorrect results.

Outlook Two ideas are presented that could be realized in future projects.

(a) **Optimization of the GCMC program:** As it has been asserted, that the program produces reliable results, it could now be optimized in speed and sampling efficiency to obtain even more accurate results in reasonable computing time. These result might be used for an improved extraction of the Euler number X.

(b) **Average channel width:** An alternative measure for the average channel width introduced in chapter 6 could lead to a more precise determination of the validity range of the morphometric formula. For example, the integral

$$\frac{\int_{\mathcal{I}} \mathrm{d}\vec{r} d_m(\vec{r})}{A[\mathcal{I}]} , \tag{8.1}$$

where $d_m(\vec{r})$ is the medial distance of $\vec{r}$ and $A[\mathcal{I}]$ the area of the interface, might be a more natural measure of the average channel width. This integral could be approximated by the sum over the medial distances of all vertices divided by the total number of vertices. For an even triangulation of the surface this could lead to a good approximation of the integral.

Appendices

A.1 Evolver File for D-CMC Surface

Changes in evolver file:

1. Vertices (2) and (4) are not fixed any more, but on constraints 1,4 and 2,3 respectively.
2. A vertex (5) at .5 -0.5 1.5 on constraints 1,3 has to be added. All vertices with the “fixed bare” property can be deleted as they are only important for better visualization.
3. Accordingly edge (3) is goes from vertex (2) to (5) and is on constraint 1.
4. An additional edge (4) from vertex (5) to (4) on constraint 3 is introduced
5. Finally the facet (1) is redefined to 2 3 -4 -5

Source code of dcell_cmc.fe file:

```
// dcell.fe

// Surface Evolver datafile for double fundamental region for D CMC



PARAMETER h_zero := 0.5 //SET h_zero
quantity sqmean energy modulus 1 method star_perp_sq_mean_curvature global
quantity mci info_only modulus 1 method mean_curvature_integral global

KEEP_ORIGINALS

symmetric_content
parameter fudge = 1/3

constraint 1 // top
formula: x + z = 2
content:
c1: fudge*(y+1)
c2: fudge*(1-x)
c3: 0

constraint 2 // right side
formula: y - x = 0

constraint 3 // left side
formula -x-y = 0

constraint 4 // front
formula: x - z = 0


view_transform_generators 6
0,1,0,0    1,0,0,0    0,0,1,0    0,0,0,1   // a: x,y swap
0,-1,0,0   -1,0,0,0   0,0,1,0    0,0,0,1   // b: x+y=0 mirror
0,0,1,0    0,1,0,0    1,0,0,0    0,0,0,1   // c: x,z swap
swap_colors 1 0 0 2 , 0 1 0 0, 0 0 1 0, 0 0 0 1 // d: x translation
swap_colors 1 0 0 0 , 0 1 0 2, 0 0 1 0, 0 0 0 1 // e: y translation
swap_colors 1 0 0 0 , 0 1 0 0, 0 0 1 2, 0 0 0 1 // f: z translation
//swap_colors 1 0 0 0,  0 -1 0 0, 0 0 -1 2, 0 0 0 1 // g: C2 rotation

vertices
2    1  0 1   constraints 1,4
```

```
3   .5 .5 .5 constraints 2,4
4   0 0 1  constraint 2,3
5  .5 -0.5 1.5 constraints 1,3



edges
2   2 3 constraint 4
3   3 4 constraint 2
4         2 5 constraint 1
5   5 4 constraint 3

facets
1   2 3 -5 -4

bodies
1  1

read

// command to show full cell in rhombic dodecahedron
showrhombic := { transform_expr "abcabc"; transforms on;
                 set edge color black;
                 set edge color clear where bare and original != 7 and
                     original != 6;
                 show_trans "R";
                                                                    }
setcolor := { set facet backcolor yellow }

raw_cells
conj_grad on
augmented_hessian on
check_increase on
area_normalization off
effective_area off
metric_conversion off
autorecalc on
gv_binary off
gravity off
set facet tension 0
sqmean.modulus:=1
unset body[1] target
```

List of Figures

2.1 A sphere can be stretched and bent (without any rupture of fusion of the surfaces) into an infinite variety of globular surfaces, all topological equivalent. Source: [23] 8

2.2 Examples for the Minkowski sum of two sets. A parallel body $\mathcal{B}_r$ (2.4) of a body $\mathcal{B}$ is obtained by Minkowski addition of a sphere (or a disk in 2D) with radius r and $\mathcal{B}$. Source: [35] 10

2.3 Sketch of the pore geometry. The white part is the accessible pore space $\mathcal{P}_{\text{acc}}$ (2.22), whereas P_{ex} is the region that the sphere centers cannot penetrate due to hard core interaction with the wall. It also required that the surface is continuous on the boundaries, as depicted here. 12

3.1 The triply-periodic Diamond, Primitive and Gyroid minimal surfaces with cubic symmetries. The Primitive structure consists of 8 (smallest) cubic unit cells. The topology of the surfaces is expressed by the skeletal graph that measures the connectedness of the surface [47]. Different colors indicate the two congruent labyrinths of the balanced surfaces. Triangulated representatives are available for the Monte Carlo simulation of confined hard spheres. Source: [47]. 16

3.2 The triply-periodic H surface. The frame outlines the tetragonal translational unit cell of the surface. One side of the surface is colored green, the other orange. The two labyrinth domains are congruent, i.e. the surface is balanced. 17

3.3 (a) The initial surface patch of the evolver input file. The confining tetrahedron outlines the corresponding asymmetric unit cell of the CMC diamond. (b) Asymmetric unit patch after the minimization of the functional $E[S]$ (Eq. (3.1)) via the surface evolver program. The faces are mirror planes in the Fd$\overline{3}$m symmetry group. (c) A cubic unit cell of the D-CMC-surface with a volume fraction of $\phi = 0.25$. The colors indicate the orientation of the geometry (orange inside the pore, green outside). 20

3.4 An illustration of the step method. The plot shows schematically the volume V as function of the mean curvature H in the vicinity of H_ϕ . As this dependency is approximated linearly close to H_ϕ, the initial curvature H_{initial} is altered by δH (cf. Eq. (3.4)) to gradually generate a CMC-Diamond structure with desired volume fraction. The gradient of the linear function is a (cf. Eq. (3.2)). Each arc represents a step as defined in the step method. After $n = 3$ steps the step size is recalculated and the algorithm is iterated. 22

3.5 The two medial surfaces in either of the two geometrically different channels of the I-WP TPMS for a conventional cubic unit cell: (Top) MS of the I side (Here, the surface itself is cut open for better visibility of the MS) (Bottom) MS of the WP.Blue spheres indicate maxima of the medial distance function $d(p)$ (3.5), whereas yellow spheres indicate minima of $d(p)$ along the line graphs. Note that these points are not identical with NP $(\mathcal{P})$ (3.8) and WP $(\mathcal{P})$ (3.7). Source: [47] 24

4.1 Determination of the relaxation time for a given set of input parameters. A test simulation is run for same input parameters and the value of a measured quantity F is recorded for every MC step. F is starting to fluctuate about some average value after approximately 1000 Monte Carlo steps. To account for statistical uncertainties, the systems is considered to be in equilibrium after $N_{\mathrm{sbm}} = 2500$ steps. In the simulation the amount of MC steps performed before the actual measurement is set to N_{sbm}. 34

4.2 Snapshot of a hard sphere liquid confined to one of the domains given by the Gyroid cubic minimal surface with lattice size $L = 17\sigma$. The cubic frame is the simulation box $\mathbb{P}$ which in turn corresponds to a translational unitcell of the surface (here the cubic unitcell $L_x = L_y = L_z = L$). 34

4.3 Look-up table for fast but exact test whether a hard sphere of radius R overlaps with the solid phase or not. A detailed description is given in this section. 36

4.4 Packing fraction η simulated for different chemical potentials μ. The solid line represents the Carnahan-Starling approximation, whereas the symbols are the result of the GCMC simulation in a cubic simulation box of edge length $L = 8$, 17 or 34. The inset shows the relative difference between simulation and theory for the three different box sizes. 41

4.5 The simulation results for the definition $\Lambda^3 = V_{\mathrm{sph}}/8$. A redefinition of the chemical potential $\mu' = \mu - \ln 8$ reproduces the same results as shown in Fig. 4.4. As expected, the thermodynamic equilibrium properties do not depend on the choice of the thermal wavelength. 41

4.6 Two Point correlation function $g(r)$ of unconfined hard sphere fluids. Symbols are the result of GCMC simulation in a cubic box of size $L = 17$. Lines represent $g(r)$ in Carnahan-Starling approximation. The inset show the relative difference between theory and simulation for the densest (black) and the least densest case (red). 42

4.7 The excess part of the chemical potential potential μ_{ex} (Eq. (2.28)) converges to zero for small packing fractions η of the reservoir for all simulation box sizes, i.e. in the ideal gas limit. Therefore the simulation reproduces the expected thermodynamical behavior. 43

4.8 Simulation result for a sphere of radius $0.3L$ placed in the center of a cubic simulation box with edge length L. The inner part of the sphere is defined as the pore space, whereas the outer part represents the substrate. The relative difference between the confined packing fraction η_0 and the reservoir packing fraction η is plotted versus η. There are deviations from the bulk case due to the confining geometry, that decrease with larger box size and smaller packing fraction of the reservoir. This behavior is typical for all solid pore interfaces examined in this work. An explanation for that behavior is given in section 4.5.1. 45

4.9 Simulation result for the Gyroid (s. Fig. **??**) for box sizes $L = 8, 17, 34$. Although the geometry of the Gyroid (Fig. 3.1) is more complex than the geometry of a single sphere, the behavior of the relative difference between the confined packing fraction and η is similar (Fig. 4.8). An explanation for the positivity of $(\eta_0 - \eta)/\eta$ is given in section 4.5.1. 47

4.10 Simulation result for all TPMS of table 4.2 for $L = 8$. The P8uc is showing the largest relative difference $(\eta_0 - \eta)/\eta$ as it has the least pore volume compared to all other TPMS with $L = 8$. As all surfaces have the same surface area the ratio of surface area A to volume V is the largest for the P8uc surface. According to the explanation given in section 4.5.1, this is reason for the large relative difference $(\eta_0 - \eta)/\eta$ of the P8uc structure compared to the other shown TPMS. 48

4.11 Comparison of simulation result and DFT data for the Gyroid. The data were obtained by 3D DFT calculations, carried out by Roland Roth, using voxelized data sets for the TPMS [44]. The agreement of both approaches is very good. Thus the simulation data can be regarded as being well established within the parameter range of η. For $L = 34$ the DFT calculation are not available. 49

5.1 The coefficients Γ_σ, Γ_κ and $\Gamma_{\bar\kappa}$ of the morphometric approach for the confined packing fraction η_0 (Eq. (5.7)) on the left hand side. On the right hand side the volume term $\rho_{\mathrm{bulk}}V$, the area term $\Gamma_\sigma A$ and the topological term $\Gamma_{\bar\kappa}X$ appearing in the morphometric approach for η_0 (Eq. (5.7)). The volume V, area A and Euler X are chosen to be equal to the geometrical values for Gyroid for a box size $L = 8$. For such a system the contribution of the topological term to the confined packing fraction η_0 is small compared to the volume and area term, as the Euler number is not scaling with the system size. Note the logarithmic scale on the y-axis. 55

5.2 The relative difference $(\eta_0 - \eta)/\eta$ as predicted by the morphometric approach Eq. (5.12) (solid line) compared both to the simulation and DFT data (symbols). The agreement of both numerical approaches to the theoretical curve is really striking. Obviously the morphometric approach is working well within this range of η and L for the Gyroid. 56

5.3 Primitive and P8uc: On the one hand theory and simulation are in very good agreement for the P surface. On the other hand there are deviations for the 8 unit cell equivalent. This can be explained by a violation of the additivity condition set on the grand canonical potential in section 5.1. As the channel system of the P8uc structure is two times narrower than that of the primitive, correlation effects play an important role here. A detailed discussion on that is given in chapter 6. 57

5.4 Simulation results for the Diamond, IWP (both orientations) and the H surface and the theoretical predictions. Beside minor deviations for $L = 8$ for bulk packing fractions $\eta \leq 0.25$ the theory is in quantitative agreement with the simulation results. 58

5.5 Spherical pores: The good quantitative agreement shows, that the morphometric approach also works for geometries with integrated mean curvature $C \neq 0$. 59

5.6 Cylindrical pores: We also observe good agreement with the theoretical predictions. 60

5.7 Adsorption plots for Primitive and P8uc. The deviation behavior is similar to the confined packing fraction (s. Fig. 5.3), as the predictions are very accurate for the primitive whereas the numerical results deviate from the theoretical curve for the P8uc for $L = 8$. The almost identical graphs for $L = 8$ and $L = 17$ are due to the fact that $(\Gamma_{\bar{\kappa}}(\eta)X[\mathcal{P}]/A[\mathcal{P}])$ is the only varying parameter which is small compared to $\Gamma_\sigma(\eta)$ (s. Eq. 5.18). 61

5.8 Plots for the other examined structures. The agreement for all of them is still really good, although all geometries except the H surface show stronger deviations with increasing bulk packing fraction for a scaling factor of 8. . . 61

5.9 The extraction of the Euler number for attempt (1). Although the quantitative agreement needs to be improved, the correct tendency is reproduced for all geometries. This is an amazing result as the contribution of the topological term to average number of particles is very small compared to the other terms appearing in the morphometric approach (cf. Fig. 5.1). Nevertheless the data is deteriorating outside the presented η-range and does not show the expected behavior. The values behind the surface names are the corresponding Euler numbers. Except for P and D, the error bars are omitted for better visibility. The uncertainties for the other surfaces are comparable in magnitude. 64

5.10 The extraction of the Euler number for attempt (2). Slight improvements compared to the first approach are observed (cf. Fig. 5.9). Especially for the Primitive surface a better agreement is visible. For better visibility, only for the P and the D surface error bars are shown. The uncertainties for all other surfaces are comparable in magnitude. The large error bars compared to attempt (1) are due to the fact, that errors in the area coefficient Γ_σ and in the determination of the bulk packing fraction are taken into account. . . 65

5.11 The result for attempt (3). The Euler number X is even better extracted compared to attempt (1) and (2). Also the η-range could be extended up to a value of 0.35. 66

5.12 This graph shows both the DFT (see Eq. 5.9) curve and the fitted data for Γ_σ and $\Gamma_{\bar{\kappa}}$. The fitted area coefficient is in good agreement with the theoretical curve whereas the topological term shows no qualitative agreement for $\eta > 0.15$. The error bars for $\Gamma_{\bar{\kappa}}$ are omitted as they are larger than the y-range of the plot. 67

6.1 The average channel width $(d_{\text{min}} - d_{\text{max}})/2$ in terms of the correlation length ξ is plotted against the difference $\eta_0^{\text{Sim}} - \eta_0^{\text{morph}}$ between the simulation results and the morphmetric prediction for η_0. For systems where the average channel width is smaller than two times the correlation length $\xi(\eta)$ (Fig. 6.6), significant deviations between theory and simulation are observed. For larger channel widths the morphmetric approach predicts the simulation results very accurately. The error bars are not shown as they are smaller than the symbol size. 70

6.2 The Diamond surface shows a similar behavior as the Gyroid for $L = 5, 6$. On the other hand for $L \geq 7$ the theoretical prediction are accurate even for systems where the average channel width is smaller than two times the correlation length. 71

6.3 The behavior of the IWP (WP) is similar to that of the Diamond surface. For box sizes $L \geq 7$ small deviations are observed for narrow channels. . . . 71

6.4 Deviations for the IWP (I) surface. Only for $L = 5, 6$ significant deviations are observed. 72

6.5 Almost no deviations are found for the H surface, exept for $L = 5$. Obviously the morphometric formula is very accurate for this structure. 72

6.6 The correlation length $\xi(\eta)$ as a function of the bulk packing fraction. The data is taken from Ref. [45], where it was obtained by means of density functional theory. 73

7.1 Density profiles in perpendicular direction to a 3D planar wall for a hard sphere system (a) and an ideal gas system (b). The local density is zero for a distance smaller than the sphere radius R for both cases. For values larger than R the density of the hard sphere system oscillates in a rather complex manner towards the bulk value ρ_{bulk} whereas $\rho(x) = \rho_{\text{bulk}}$ for the ideal gas system. Therefore the bulk density can be reproduced for case (b) by identifying $\rho_{\text{bulk}} = \langle N \rangle / V_{\text{acc}}$ (see Eq. (7.6)). In contrast this not possible for case (a). 76

7.2 Confined ideal gas simulation results for the gyroid with simulation box size $L = 10$ (a) for the original definition of μ^*_{ex} (Eq. (7.2)) and (b) for definition (7.8). By subtracting $\ln(V/V_{\text{acc}})$ in Eq. (7.2) the star excess chemical potential μ^*_{ex} is zero for all values of μ^* as is necessary for an ideal gas. The amount of sampled configurations is almost equal for all data points, therefore the error of μ^*_{ex} is larger for lower densities. 77

7.3 Simulation results for the Gyroid structure with μ^* as input parameter. The results are qualitatively equivalent to the simulation results obtained with μ as input parameter (cf. Fig. 5.2). The agreement with the theoretical prediction is also apparent. 78

7.4 Bulk simulation of an ideal gas in a simulation box of size 10^3. The wrong behavior of μ_{ex} for low μ^* values is due to a mistake in the Monte Carlo algorithm. For systems with significant probability for number of particles $N = 0$, the insertion of particles was preferred what led to a violation of the detailed balance condition (4.17). 80

List of Tables

2.1 Euler number for some simple geometries. It can be calculated by $X = 1 - g(S)$, where the genus of the surface $g(S)$ is sum of cavities and handles (see Eq. (2.1)). Note that the Euler number of a sphere is equal to 1 for the definition used in this thesis. Source: [1] 9

3.1 Evolution of D CMC structures with a given volume fraction. These surfaces are obtained by the step method. The volume of the initial asymmetric unit cell is $(1/12) \cdot d^3$ with d as edge length of the Fd$\bar{3}$m cubic unit cell. 21

4.1 Properties of the used geometries for a box size of L. Inside means that the pore space is the inner part of the sphere/cylinder, outside the opposite. . . 45

4.2 List of the studied solid pore interfaces that are introduced in section 3.1. For all geometries the box size is set up in a way that the surface area equals the surface area of the Gyroid for box size L. As this structure is well understood and a lot of simulation data are available, it is taken as a reference point. The intertwined channel systems of Gyroid, P and D are congruent as mentioned in section 3.1 whereas this is not the case for the IWP surface. Therefore results for both orientations are presented. (I) means, that the I-labyrinth is the pore domain and vice versa. P8uc denotes a primitive surface but with 8 (smallest) cubic unit cells within the simulation box (instead of one). Finally the H structure does not have a cubic but a (non-primitive) tetragonal unit cell, so edge lengths are given in each space direction. The deeper meaning of this choice becomes apparent in chapter 5. 46

Bibliography

[1] http://en.wikipedia.org.

[2] D.J. Adams. Chemical potential of hard-sphere fluids by monte carlo methods. *Mol. Phys.*, 28(5):1241–1252, 1974.

[3] M.P. Allen and D.J. Tildesley. *Computer Simulations of Liquids.* Clarendon, Oxford, 1987.

[4] Boost:. http://www.boost.org/.

[5] K. Brakke. The surface evolver. *Experimental Mathematics*, 1(2):141–165, 1992.

[6] Norman F. Carnahan and Kenneth E. Starling. Equation of state for nonattracting rigid spheres. *The Journal of Chemical Physics*, 51(2):635–636, 1969.

[7] J.C.C. Nitsche D.M. Anderson, H.T. Davis and L.E. Scriven. Periodic surfaces of prescribed mean curvature. *Advances in Chemical Physics*, 77:337–396, 1990.

[8] Manfredo P. Do Carmo. *Differential Geometry of Curves and Surfaces.* Prentice Hall, Inc. Englewood Cliffs, New Jersey, 1976.

[9] Siem E.J. and Carter W.C. The stability of several triply periodic surfaces. *Interface Science*, 10:287–296(10), December 2002.

[10] R. Evans. Fluids adsorbed in narrow pores: phase equilibria and structure. *J. Phys.: Condens. Matter*, 2:8989–9007, 1990.

[11] Surface Evolver. http://www.susqu.edu/brakke/evolver/downloads/dcell.fe.

[12] Daan Frenkel and Berend Smit. *Understanding Molecular Simulation.* Academic Press, 2004.

[13] D. Hörndlein F. Krach T. Hiester G.E. Schröder-Turk, S. Kuczera and K. Mecke. Monte carlo simulations of confined hard sphere fluids. *Physics Procedia*, 3(3):1493 – 1497, 2010. Proceedings of the 22th Workshop on Computer Simulation Studies in Condensed Matter Physics (CSP 2009).

[14] S.C. Kapfer F.M. Schaller B. Breidenbach D. Hug G.E. Schroeder-Turk, W. Mickel and K. Mecke. Minkowski tensors of anisotropic spatial structure. unpublished.

[15] Lev D. Gelb, K.E. Gubbins, R. Radhakrishnan, and M. Sliwinska-Bartkowiak. Phase separation in confined systems. *Rep. Prog. Phys.*, 62:1573–1659, 1999.

[16] Karsten Grosse-Brauckmann. Stable constant mean curvature surfaces minimize area. *Pacific J. Math.*, 175 Number 2:527–534, 1996.

[17] Karsten Grosse-Braukmann. On Gyroid interfaces. 187:418–428, 1997.

[18] H. Hadwiger. *Vorlesungen über Inhalt, Oberfläche und Isoperimetrie.* Springer, 1957.

[19] Theo Hahn, editor. *International Tables For Crystallography.* Kluwer Academic Publishers, Dordrecht, third and revised edition, 1992.

[20] Jean Pierre Hansen and Ian R. McDonald. *Theory of Simple Liquids.* Academic Press, 2nd edition, 1986.

[21] Hendrik Hansen-Goos and Roland Roth. Density functional theory for hard-sphere mixtures: the white bear version mark ii. *Journal of Physics: Condensed Matter*, 18(37):8413, 2006.

[22] Houdini. http://www.sidefx.com/.

[23] S. T. Hyde, S Andersson, K Larsson, Z Blum, T Landh, S Lidin, and B. W. Ninham. *The Language of Shape.* Elsevier Science B. V., Amsterdam, 1st edition, 1997.

[24] S.T. Hyde, M. O'Keeffe, and D.M. Proserpio. A short history of an elusive yet ubiquitous structure in chemistry, materials and mathematics. *Angewandte Chemie International Edition*, 47(42):7996–8000, 2008.

[25] V.I. Kalikmanov. *Statistical Physics of Fluids.* Springer, 2001.

[26] H. Karcher. The triply periodic minimal surfaces of A. Schoen and their constant mean curvature companions. *Man. Math.*, 64:291–357, 1989.

[27] P.-M. König. *Influence of Geometry on Thermodynamics. the Structure of Fluids, and Effective Interactions in Key-Lock Systems.* PhD thesis, Institut für Theoretische und Angewandte Physik, Universität Stuttgart, 2005.

[28] P.-M. König, R. Roth, and K.R. Mecke. Morphological thermodynamics of fluids: Shape dependence of free energies. *PRL*, 93(16):160601, 2004.

[29] Charla A. Lambert, Leonard H. Radzilowski, and Edwin L. Thomas. Triply periodic level surfaces as models for cubic tricontinuous block copolymer morphologies. *Philosophical Transactions: Mathematical, Physical and Engineering Sciences*, 354(1715):2009–2023, 1996.

[30] C. N. Likos, K. R. Mecke, and H. Wagner. Statistical morphology of random interfaces in microemulsions. *The Journal of Chemical Physics*, 102(23):9350–9361, 1995.

[31] K R Mecke. A morphological model for complex fluids. *Journal of Physics: Condensed Matter*, 8(47):9663, 1996.

[32] K. R. Mecke. Morphological thermodynamics of composite media. *Fluid Phase Equilibria*, 150-151:591 – 598, 1998.

[33] K.R. Mecke. *Integralgeometrie in der statistischen Physik.* Harri Deutsch (Frankfurt), 1994.

[34] Nicholas Metropolis, Arianna W. Rosenbluth, Marshall N. Rosenbluth, Augusta H. Teller, and Edward Teller. Equation of state calculations by fast computing machines. *J. Chem. Phys.*, 21(6):1087–1092, June 1953. This article introduces the Metropolis algorithm, which the journal *Computing in Science and Engineering* cited in the top 10 algorithms having the "greatest influence on the development and practice of science and engineering in the 20th Century.".

[35] Walter Mickel. Charakterisierung anisotroper strukturen mittels minkowski-tensoren. Diploma thesis, 2008.

[36] David Nicholson and Neville George Parsonage. *Computer simulation and the statistical mechanics of adsorption.* Academic Press, 1982.

[37] G. E. Norman and V. S. Filinov. Investigations of phase transitions by a monte-carlo method. *High Temperature*, 7:216–222, 1969.

[38] Jerome K. Percus and George J. Yevick. Analysis of classical statistical mechanics by means of collective coordinates. *Phys. Rev.*, 110(1):1–13, Apr 1958.

[39] F.P. Preparata and M.I. Shamos. *Computational Geometry.* Springer-Verlag, 1985.

[40] W.H. Press, S.A. Teukolsky, W.T. Vetterling, and B.P. Flannery. *Numerical Recipes, The Art of Scientific Computing.* Cambridge University Press, 3 edition, 2007.

[41] Robert C. Reilly. Mean curvature, the laplacian, and soap bubbles. *The American Mathematical Monthly*, 89(3):180–198, 1982.

[42] Yaakov Rosenfeld. Free-energy model for the inhomogeneous hard-sphere fluid mixture and density-functional theory of freezing. *Phys. Rev. Lett.*, 63(9):980–983, Aug 1989.

[43] R. Roth, R. Evans, A. Lang, and G. Kahl. Fundamental measure theory for hard-sphere mixtures revisited: the white bear version. *JPCM*, 2002.

[44] Roland Roth. private communication.

[45] Roland Roth. *Depletion forces in hard sphere mixtures.* PhD thesis, Bergische Universität-Gesamthochschule Wuppertal, 1999.

[46] Gerd E. Schröder, Stuart J. Ramsden, Andrew G. Christy, and Stephen T. Hyde. Medial surfaces of hyperbolic structures. 35:551–564, 2003.

[47] Gerd Elmar Schröder. *Skeletons in the Labyrinth.* PhD thesis, Australian National University, Canberra, Australia, 2005.

[48] Sklog Wiki. http://www.sklogwiki.org/SklogWiki/index.php/Grand_canonical_Monte_Carlo.

Danksagung

Hiermit möchte ich mich bei Dr. Gerd Schröder-Turk, Prof. Dr. Roland Roth und Prof. Dr. Klaus Mecke bedanken, die diese Arbeit auf angenehme Weise betreut haben und stets für Frage zur Verfügung standen und zahlreiche nützliche Hinweise geliefert haben. Zudem danke ich allen Kollegen am Lehrstuhl für Theoretische Phyik I fur̈ die nette freundschaftliche Atmosphäre und große Hilfsbereitschaft über das gesamte letzte Jahr. Ich danke dem Exzellenzcluster "Engineering of Advanced Materials" und dem Institut für Theoretische Physik I für finanzielle Unterstützung für meinen Aufenthalt für die Teilnahme an der DPG-Frühjahrstagung in Regensburg und für die Teilnahme an der EAM Winterschool in Kirchberg/Tirol, bei denen ich die Ergebnisse meiner Arbeit vorstellen konnte. Zu guter Letzt noch ein Dank an meine Eltern, die mir das Studium ermöglicht haben und mich stets unterstützt haben.

Erklärung

Hiermit erkläre ich, dass ich die vorliegende Diplomarbeit selbstständig angefertigt habe. Es wurden nur die in der Arbeit ausdrücklich genannten Quellen und Hilfsmittel benutzt. Wörtlich oder sinngemäß übernommenes Gedankengut habe ich als solches kenntlich gemacht.

Ort und Datum Unterschrift